学位論文（要約）

Determination of absolute CEP by circularly-polarized few-cycle pulses and dissociative ionization of methanol in intense UV laser fields

（円偏光数サイクルパルスによる絶対 CEP の決定と紫外域強レーザー場中におけるメタノールの解離性イオン化）

平成 28 年 12 月博士（理学）申請

東京大学大学院理学系研究科
化学専攻
深堀 信一

Abstract

Ionization and dissociation of molecules in intense laser fields are strongly influenced by the waveform of the laser field. The preparation of electronically excited states of molecular cation plays a crucial role in dissociative ionization of molecules in intense laser fields. In this thesis, on the basis of photoelectron emission of atoms and molecules in intense laser fields, (i) I proposed a characterization method of one parameter which represents the waveform of a few-cycle laser pulse, called carrier-envelope phase (CEP), and (ii) I investigated the preparation processes of the electronically excited states in dissociative ionization of methanol (CH_3OH).

The basis of ionization of atoms and molecules in intense laser fields and related recent researches are introduced as general introduction in Chapter 1. In Chapter 2, theory of tunnel ionization is summarized. In Chapter 3, the character of few-cycle pulses is introduced. CEP is varied during the propagation of the laser pulse in dispersed media, indicating CEP should be determined at laser-molecule interaction point, defined as absolute CEP. The CEP of a circularly polarized few-cycle pulse represents the direction of the laser electric fields.

In Chapter 4, the absolute CEP is determined by the angle-resolved photoelectron spectra of Ar recorded using intense circularly polarized few-cycle laser pulses. In order to examine the depletion effect of Ar atoms by the ionization and the Coulombic potential effect on the motion of the electrons after tunnel ionization, classical trajectory Monte Carlo simulations are performed. It is found that the absolute CEP can be determined from the asymmetric ejection of high energy photoelectrons without any numerical calculations when the peak laser intensity is in the range between 1×10^{14} W/cm^2 and 5×10^{14} W/cm^2.

In Chapter 6~8, I investigate dissociative ionization of CH_3OH in intense ultraviolet (UV) laser fields by photoelectron-photoion coincidence momentum imaging (PEPICO-MI). The detail of PEPICO-MI is described in Chapter 5. From the analysis of the channel-specific photoelectron angular distributions (PADs), it is revealed that CH_3OH is decomposed into $CH_3^+ + OH$ after the five-photon ionization to the second electronically excited $\tilde{B}$ state of CH_3OH^+, and after the four-photon ionization to the electronic ground $\tilde{X}$ state of CH_3OH^+ followed by further excitation into the electronically excited states by absorbing additional photons. Furthermore, the dependence of the PADs on the orientation of the C-O bond axis with respect to the laser polarization direction is examined. When the four-photon ionization to the $\tilde{X}$ state occurs, the photoelectrons are ejected along the direction parallel to the laser polarization direction irrespective to

the orientation, while when the five-photon ionization to the $\tilde{B}$ state occurs, the direction of the photoelectron emission is sensitive to the orientation. In the case of dissociation into $CH_2OH^+ + H$, the dominant pathway is switched from the four-photon ionization to the vibrationally highly excited states in the $\tilde{X}$ state to the five-photon ionization to the $\tilde{B}$ state as the laser intensity increases, in addition to the similar pathway as the CH_3^+ channel, the four-photon ionization to the $\tilde{X}$ state followed by subsequent electronic excitation.

This thesis is summarized and the future prospect is discussed in Chapter 9.

Contents

1. General introduction

1-1. Molecules in intense laser fields

When molecules are irradiated with intense laser pulses, many characteristic phenomena occur [1,2], such as molecular alignment [3], structural deformation [4-7]. Multiphoton and tunnel ionization of atoms and molecules also occur in intense laser fields, followed by dissociation of the molecules and high-order harmonic generation [8-10].

In order that atoms and molecules are ionized by light, its photon energy needs to exceed the ionization energy. However, when the laser intensity is high, in other words, when the number of photons in the unit volume is large, multiphoton ionization becomes possible. The number of absorbed photons for ionization is not necessarily two or three, but can be more than ten. Furthermore, the number of absorbed photons can exceed the minimum number needed for ionization in the phenomenon called above threshold ionization [11,12].

At the same time, the laser electric field becomes comparable to the Coulombic field between the electrons and the nuclei, leading to tunnel ionization or over-the-barrier ionization. When double or multiple ionization occurs, the multiply-charged molecular ion is decomposed due to Coulomb repulsion, that is, the phenomenon called Coulomb explosion occurs [13-15]. The probability of multiple ionization is enhanced in intense laser fields, by re-collision of ejected photoelectrons to the ion core, that is, nonsequential double ionization [16], or the elongation of the internuclear distances of molecules, that is, enhanced ionization [17].

As above, ionization is a key process to understand the molecular dynamics in intense laser fields.

1-2. Ionization processes of intense laser fields

1-2-1. Above threshold ionization

1-2-1-1. Above threshold ionization in nanosecond laser fields

Above threshold ionization (ATI) is ionization process in which the number of absorbed photons is more than the minimum number needed to exceed the ionization energy I_p [11,12,18,19]. The first observation of ATI is in 1979 [11]. Figure 1-1 shows schematic pictures of the photoelectron spectra of Xe by the 1064 nm (1.17 eV) nanosecond laser pulses. In Fig. 1-1(a), the spectrum exhibits a strong peak at photoelectron energy E_{elec} = 0.70 eV, which is assigned to eleven-photon ionization.

Eleven photons are necessary to exceed the ionization energy of Xe, I_p = 12.12 eV. In addition to this peak, the other peaks can also be identified, suggesting that more than eleven photons are absorbed.

In one-photon ionization, the photoelectron energy is given by

$$E_{elec} = \hbar\omega - I_p, \quad (1\text{-}1)$$

where ω is the frequency of the light. The energy diagram is shown in Fig. 1-2(a). Similarly, in multiphoton ionization (MPI) or ATI by nanosecond laser pulses, the photoelectron energy can be expressed as

$$E_{elec} = (n + s)\hbar\omega - I_p, \quad (1\text{-}2)$$

where n is the minimum number of photons needed to exceed I_p and s (s = 0, 1, 2, ⋯) is the number of additional photons. In Fig. 1-1, n is eleven and the peaks corresponding to up to s = 3 are identified.

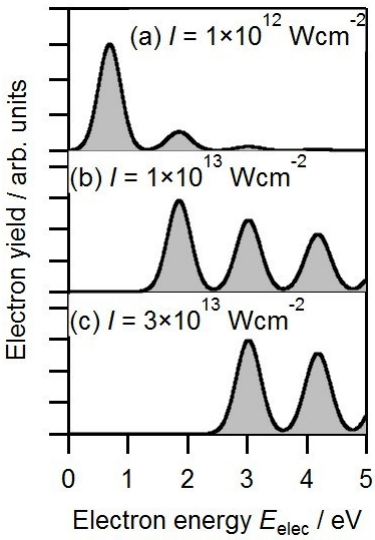

Fig.1-1 Schematic pictures of ATI photoelectron spectra of Xe by 1064 nm nanosecond laser pulse. The laser intensity is (a) 1×10^{12} W/cm^2, (b) 1×10^{13} W/cm^2 and (c) 3×10^{13} W/cm^2. Only $^2P_{3/2}$ of Xe^+ is considered. Relative intensities among the peaks are not estimated quantitatively.

As shown in Figs. 1-1(b) and 1-1(c), when the laser intensity I becomes larger, the photoelectron energies at which the peaks are observed in the spectra are not varied. However, the peak at E_{elec} = 0.7 eV disappears in Figs. 1-1(b) and 1-1(c), suggesting channel closing [19] of eleven-photon ionization. In an intense laser field, a photoelectron needs the quiver energy called ponderomotive energy

$$U_p = \frac{e^2 E_0^{\,2}}{4m_e\omega^2} = \frac{e^2}{8\pi^2 m_e \varepsilon_0 c_0^{\,3}}\lambda^2 I, \quad (1\text{-}3)$$

in addition to the ionization energy, where E_0 is maximum amplitude, λ is the wavelength of a linearly polarized pulse. For example, the ponderomotive energy is calculated as U_p = 6 eV at λ = 800 nm and $I = 1\times10^{14}$ W/cm^2.The ponderomotive energy also acts as a gradient force ($-\nabla U_p$) in the focal area of the laser pulse [20,21]. Because a laser pulse remains until the photoelectron escapes from the focal area, the photoelectron acquires the kinetic energy which corresponds to U_p [22]. Therefore, although I_p+U_p is needed to ionize, the final kinetic energy becomes Eq. (1-2). However, when $I > 6.6\times10^{12}$ W/cm^2, $11\hbar\omega$ becomes smaller than I_p+U_p, leading to channel closing of eleven-photon ionization.

When the laser intensity is high, the relative intensities among the ATI peaks become comparable to each other. This is contradicting to the expectation from perturbation theory, suggesting that ATI is a non-perturbative phenomenon.

1-2-1-2. Above threshold ionization in femtosecond laser fields

On the other hand, when the duration of a laser pulse is not long enough so that the

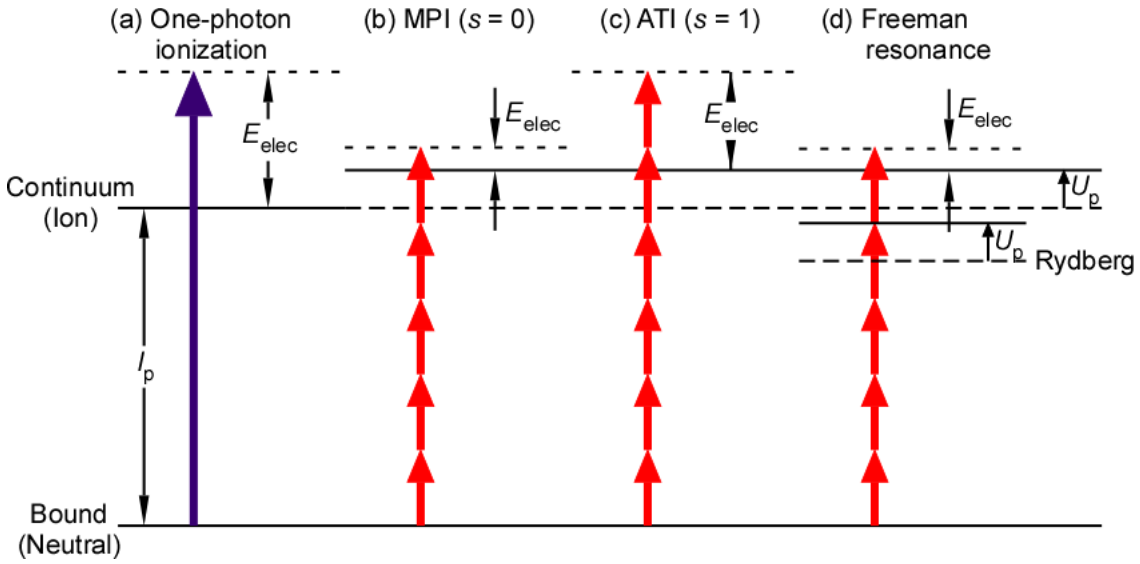

Fig.1-2 Schematic energy diagram of ionization processes. (a) One-photon ionization. (b) Multiphoton ionization. (c) Above-threshold ionization with $s = 1$. (d) Freeman resonance.

laser pulse passes through the focal area before the photoelectron escapes, the photoelectron cannot gain the potential energy U_p. In that case, the photoelectron energy can be derived as

$$E_{elec} = (n + s)\hbar\omega - I_p - U_p. \quad (1\text{-}4)$$

The schematic energy diagram is shown in Figs. 1-2(b) and 1-2(c) for MPI ($s = 0$) and ATI ($s = 1$), respectively. The energy of a continuum state increases by U_p, which can be regarded as AC-Stark shift. Therefore, the photoelectron energy is shifted as I increases [23]. Figure 1-3 shows schematic pictures of the photoelectron spectra of Xe by the 800 nm (1.55 eV) femtosecond laser pulses. The peaks are shifted to low E_{elec} and are broadened, as I increases. Furthermore, comparing to the narrow peaks in the case of the nanosecond laser pulse, the peaks are broad. Because the ponderomotive energy is proportional to the laser intensity at the moment of ionization, the energy shift depends on the time when ionization occurs and the position in the focal area, which broaden peaks in a photoelectron spectrum.

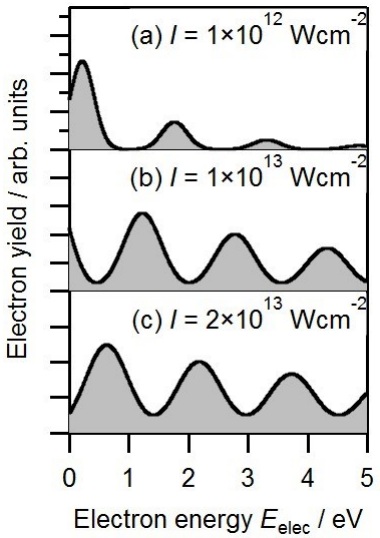

Fig.1-3 Schematic pictures of ATI photoelectron spectra of Xe by 800 nm femtosecond laser pulse. The laser intensity is (a) 1×10^{12} W/cm^2, (b) 1×10^{13} W/cm^2 and (c) 2×10^{13} W/cm^2. Only $^2P_{3/2}$ of Xe^+ is considered. Relative intensities among the peaks are not estimated quantitatively.

Rydberg states are also AC-Stark shifted in the laser field. Figure 1-4 shows the schematic picture of the photoelectron spectrum of twelve-photon ionization of Ar by 800 nm femtosecond laser pulses [24]. The

photoelectron energy of non-resonant twelve-photon ionization is shown as the vertical arrow on the dotted line. However, the actual photoelectron spectrum exhibits the split peak structure, which can be interpreted as the multiphoton resonance to the Rydberg states followed by one-photon ionization. The schematic energy diagram is shown in Fig. 1-2(d). Because the amount of the AC-Stark shift of the Rydberg state is almost the same as that of the continuum state, the energy difference between the two states is not changed from that without the AC-Stark shift, resulting that the photoelectron energy becomes independent on the laser intensity. This split structure is called Freeman resonance [23]. Because the Freeman resonance can be regarded as one-photon ionization of a Rydberg orbital, the photoelectron angular distribution contains the information about the angular momentum of the Rydberg orbital, on the basis of the selection rule of one-photon ionization [24,25].

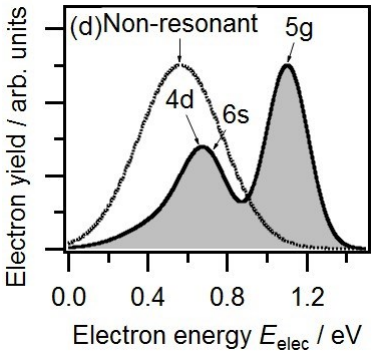

Fig.1-4 Schematic pictures of photoelectron spectrum of Freeman resonance of Ar by 800 nm femtosecond laser pulse. The laser intensity is 3.8×10^{13} W/cm^2. Dotted line is non-resonent spectrum. The resonant Rydberg states (4d, 6s, and 5g) are chosen according to [R. Wiehle, *et al.*, *Phys. Rev. A* **67**, 063405 (2003).]. Relative intensities among the peaks are not estimated quantitatively.

Furthermore, Freeman resonance of molecules has also been investigated [26]. Because the potential energy surface of a Rydberg state is almost the same as that of the ionic state into which the Rydberg state converges, the vibrational state in the ionic state becomes the same as that in the Rydberg state. Therefore, the photoelectron energy is independent on the vibrational state in the Rydberg state, and the photoelectron spectrum of Freeman resonance exhibits sharp peaks, even if for molecules.

1-2-2. KFR theory and ADK theory

The theoretical treatment of ionization in an intense laser field named strong-field approximation (SFA) is developed by Keldysh [27], Faisal [28] and Reiss [29]. This theory is also called KFR theory, named after the name of the three persons. In this theory, the transition amplitude between the initial state and the final state called Volkov state [30] is derived, in contrast to the ordinal calculation of one-photon ionization, in which the final state is the Coulomb wave function. Volkov state is the exact solution of Schrodinger equation of an electron in a laser field. It should be noted that the Coulombic potential of ionized cation is not taken into account in the final state because a strong laser field is assumed to be used.

In Keldysh's paper [27], the derived ionization probability showed that the ionization mechanism can be classified into two by Keldysh parameter

$$\gamma = \frac{\omega}{\omega_t} = \sqrt{\frac{I_p}{2U_p}}, \qquad (1\text{-}5)$$

where ω_t is tunnel ionization frequency

$$\omega_t = \frac{e|\mathbf{E}|}{\sqrt{2m_e I_p}}. \qquad (1\text{-}6)$$

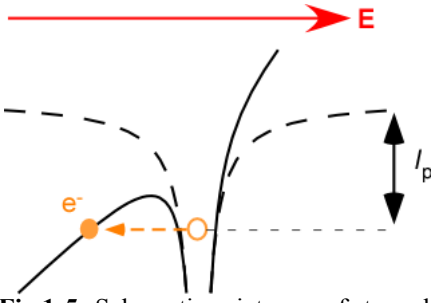

Fig.1-5 Schematic pictures of tunnel ionization.

This frequency is a reciprocal number of the time when the electron gains the kinetic energy corresponding to the ionization energy by a constant electric field **E**. When $\gamma << 1$ ($\omega_t >> \omega$), tunnel ionization (TI) dominates over MPI because the direction of the laser electric field is kept during the enough time in which TI occurs. Fig. 1-5 shows the schematic picture of TI process. The Coulombic potential of the core is modified following the laser electric field adiabatically because the oscillation of the laser field is slow enough. As a result, the electron can tunnel though the barrier. In contrast, when $\gamma >> 1$ ($\omega_t << \omega$), MPI dominates over TI.

In the case of TI, the electric field can be regarded as a constant vector. In Ammosov-Delone-Krainov (ADK) theory [31], tunnel ionization rate of a hydrogen-like atom is derived as

$$W = \frac{I_p}{\hbar} \frac{2^{2n^*}}{n^* \Gamma(n^* + l^* + 1)\Gamma(n^* - l^*)} \frac{2l+1}{2^{|m|}(|m|)!} \frac{(l+|m|)!}{(l-|m|)!} \left(\frac{2\sqrt{8m_e I_p^3}}{\hbar e|\mathbf{E}|} \right)^{2n^* - |m| - 1} \exp\left(-\frac{2\sqrt{8m_e I_p^3}}{3\hbar e|\mathbf{E}|} \right). \qquad (1\text{-}7)$$

For the application to molecules, molecular orbital (MO) ADK theory [32,33], in which a MO is decomposed into a linear combination of wavefunctions of a hydrogen-like atom as a one-center wavefunction $\Psi(r, \theta, \varphi) = \sum_{lm} C_{lm} F_l(r) Y_{lm}(\theta, \varphi)$ is known. The ionization rate can be given by

$$W = \sum_{m'} \frac{I_p}{\hbar} \frac{B(m')^2}{2^{|m'|}(|m'|)!} \left(\frac{2\sqrt{8m_e I_p^3}}{\hbar e|\mathbf{E}|} \right)^{2n^* - |m'| - 1} \exp\left(-\frac{2\sqrt{8m_e I_p^3}}{3\hbar e|\mathbf{E}|} \right), \qquad (1\text{-}8)$$

where

$$B(m') = \sum_{l,m'} (-1)^{\frac{m'+|m'|}{2}} \sqrt{\frac{2l+1}{2} \frac{(l+|m'|)!}{(l-|m'|)!}} C_{lm} D^l_{m'm}(\mathbf{\Omega}) \qquad (1\text{-}9)$$

and $D^l_{m'm}$ is Wigner's rotational matrix element. The angle **Ω** represents the Euler angle between the quantization axis of the wavefunctions of a hydrogen-like atom and the laser polarization axis.

1-2-3. Simple man's model and re-collision process

After tunnel ionization, which can be described by a quantum picture, a photoelectron

can be regarded as a classical particle. In simple man's model [10,34], the motion of a photoelectron after the tunneling can be derived by solving Newton's equation of motion in a laser electric field as

$$\frac{\mathrm{d}\mathbf{p}_{\mathrm{elec}}(t)}{\mathrm{d}t} = -e\mathbf{E}(t), \tag{1-10}$$

where $\mathbf{p}_{\mathrm{elec}}(t)$ is a momentum of a photoelectron as a function of time t. When the tunneling occurs at $t = t_0$, the final momentum $\mathbf{p}_{\mathrm{elec}}$ can be derived as

$$\mathbf{p}_{\mathrm{elec}} = \mathbf{p}_{\mathrm{elec}}(t \to \infty) = -e\mathbf{A}(t_0), \tag{1-11}$$

where $\mathbf{A}(t)$ is the laser vector potential

$$\mathbf{A}(t) = -\int_{-\infty}^{t} \mathbf{E}(t)\mathrm{d}t\,. \tag{1-12}$$

Therefore, the final kinetic energy can be obtained as

$$E_{\mathrm{elec}} = \frac{e^2|\mathbf{A}(t_0)|^2}{2m_{\mathrm{e}}}\,. \tag{1-13}$$

The photoelectrons are ejected towards antiparallel to $\mathbf{E}(t_0)$ by the tunnel ionization as shown in Fig. 1-6(a). However, when a linearly polarized pulse is used, some of the ejected electrons can go back to the ion core, because the laser electric field is oscillating as shown in Fig. 1-6(b). This return of a photoelectron induces many phenomena in intense laser fields. When the photoelectron elastically scattered backward by the ion core (rescattering) as shown in Fig. 1-6(c), the electron can gain more energy than that without rescattering. According to the Newton's equation of motion of a photoelectron in a linearly polarized field, the maximum kinetic energy becomes $10U_{\mathrm{p}}$ when the electron is back-scattered [34]. Contrary, the maximum value of the kinetic energy of photoelectrons without rescattering, Eq. (1-13), is $2U_{\mathrm{p}}$. Therefore, the photoelectron spectrum exhibits two cutoff, which is photoelectron energy at which the electron yield suddenly decreases. The first cutoff is at $2U_{\mathrm{p}}$, which is ascribed to the electrons without rescattering, and the second is at $10U_{\mathrm{p}}$, which is ascribed to the electrons with rescattering. Between the two

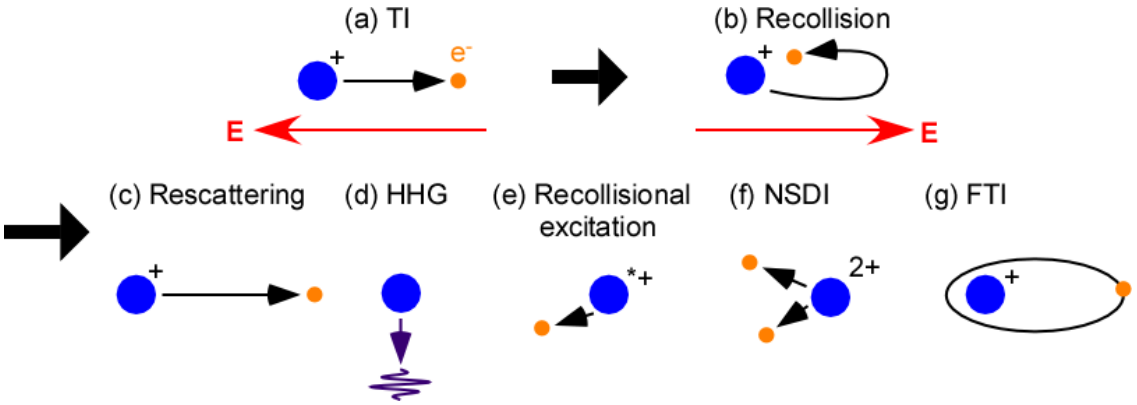

Fig.1-6 Schematic pictures of re-collision processes. (a) Tunnel ionization. (b) Re-collision (c) Rescatterting. (d) High-order harmonic generation. (e) Re-collisional excitation. (f) Nonsequential double ionization. (g) Frustrated tunnel ionization.

cutoffs, the energy range called plateau [35], where the electron yield is not varied in logarithmic scale, is formed.

When the returning photoelectron and the ion are recombined [10], the energy corresponding to the sum of the ionization energy and the energy of the returning electron is emitted as light as shown in Fig. 1-6(d). Because the spectrum of this light exhibits peaks at the odd harmonics of the fundamental laser pulses, this emission is called high-order harmonic generation (HHG) [8,9]. According to simple mans' model, the maximum photon energy, i.e., cutoff energy, of high-order harmonics becomes I_p+3.17U_p in a linearly polarized field, suggesting that the emission of vacuum ultraviolet or even soft-X ray is possible by the laser intensity of 10^{14} W/cm^2 with near-infrared laser pulses.

Re-collision of the returning photoelectron also excites, indicating inelastic scattering shown in Fig. 1-6(e), or further ionizes the ion core as shown in Fig. 1-6(f). The latter is called nonsequential double ionization (NSDI) [16]. It is known that the yield of double ionization is larger than that when only sequential double ionization is considered. When the laser intensity is large, sequential double ionization pathway becomes dominant. On the other hand, some returning electrons can be captured by the ion core as a Rydberg electron as shown in Fig. 1-6(g). This phenomenon is called frustrated tunnel ionization (FTI) [36] and Rydberg states are populated after the laser pulse passed.

Actually, probability of re-collision process is very small due to spread of electron wavepacket. In a classical picture, the electron cannot go back to the ion core because of the initial momentum at the moment of the tunneling, which is neglected in simple man's model. However, the re-collision probability is higher than that expected, suggesting that the attractive Coulombic force between the electron and the ion core plays an important role. This phenomenon is called Coulomb focusing [37-39].

Re-collision phenomena occur only with linearly polarized pulse, and not with circularly polarized pulse [35]. Recently, it is realized that orthogonally polarized two-color pulses [40-45] or counter-rotated circularly polarized two-color pulses [46,47] are able to induce re-collision.

1-3. Control of molecular dynamics by intense laser pulses

1-3-1. Control by parameters of laser pulse

The ionization of atoms and molecules and the subsequent processes such as dissociation in an intense laser field are dependent on the parameters of the laser electric pulse, such as the laser intensity, the wavelength and the pulse duration Δt [48-50]. The dispersion of the laser pulse can also be used for the control of the molecular dynamics [51-59]. Furthermore, the enhancement of a specific chemical bond breaking has been achieved by the closed-loop optimal control [60,61].

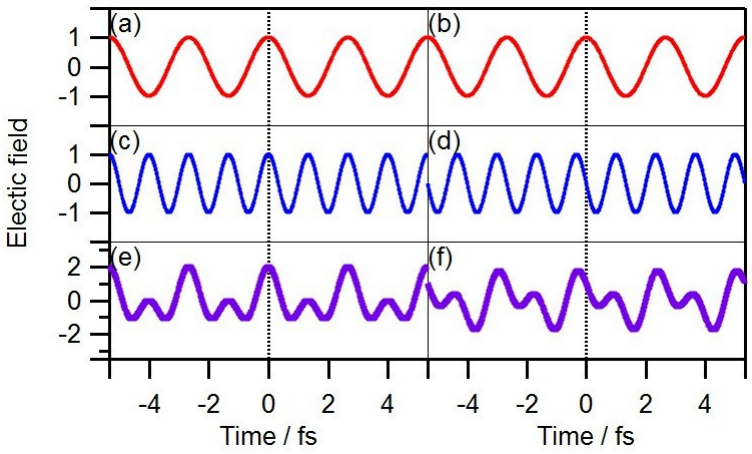

Fig.1-7 (a) 800 nm laser electric field. (b) The same as (a). (c) 400 nm laser electric field at $\phi_{\omega\text{-}2\omega} = 0°$. (d) 400 nm laser electric field at $\phi_{\omega\text{-}2\omega} = 90°$. (e) The sum of (a) and (c). (f) The sum of (b) and (d).

1-3-2. Two-color pulses

When a fundamental linearly polarized laser field and its frequency doubled laser field, whose polarization direction is set to be parallel to that of the fundamental field, are combined, the two-color laser field can be expressed as

$$\mathbf{E}_{\omega-2\omega}(t) = E_0\hat{\mathbf{x}}\left[\cos\omega t + \cos(2\omega t + \phi_{\omega-2\omega})\right], \tag{1-14}$$

where $\phi_{\omega\text{-}2\omega}$ is the relative phase between the two fields. Figures 1-7(a) and 1-7(b) show the fundamental laser field, Figs. 1-7(c) and 1-7(d) show the second harmonic laser field and Figs. 1-7(e) and 1-7(f) show the two-color laser field. The two color laser field at $\phi_{\omega\text{-}2\omega} = 0°$, in which Figs. 1-7(a) and 1-7(c) are combined as shown in Fig. 1-7(e), exhibits an asymmetric electric field. On the other hand, the two-color laser field at $\phi_{\omega\text{-}2\omega} = 90°$, in which Figs. 1-7(b) and 1-7(d) are combined as shown in Fig. 1-7(f), exhibits a symmetric electric field. In this manner, the waveform of the two-color laser field can be controlled by the relative phase $\phi_{\omega\text{-}2\omega}$. This control of the waveform has been applied to control strong field phenomena [62-67]. Similarly, the waveform controls by the relative polarization, e.g., the orthogonally polarized field [40-44] and co-rotated and counter-rotated circularly polarized field [46], have also been used to control strong field phenomena. In addition, not only two-color but also three-color or four-color laser field is used to synthesize the laser field and to control strong field phenomena [68].

1-3-3. Carrier-envelope phase of a few-cycle pulse

The asymmetric laser field can also be generated by one laser pulse whose pulse duration is extremely short. The electric field of the linearly polarized laser pulse whose envelope function is assumed to be Gaussian function is given by

$$\mathbf{E}(t) = E_0 \exp\left[-2(\ln 2)\left(\frac{t}{\Delta t}\right)^2\right]\hat{\mathbf{x}}\cos(\omega t + \phi_{\text{abs}}). \tag{1-15}$$

The relative phase ϕ_{abs} of the carrier wave with respect to the center of the envelope function is called carrier-envelope phase (CEP) [69-71]. Figures 1-8(a) and 1-8(b) show the electric field of the laser pulses at ϕ_{abs} = 0 and 90°, respectively, when their pulse durations are Δt = 30 fs (full width at half maximum, FWHM) and their wavelengths are λ = 800 nm. In Fig. 1-8(c), the magnification view of Fig. 1-8(a) in the range of t = -10 ~ +10 fs is shown, and in Fig. 1-8(d), the magnification view of Fig. 1-8(b) is shown. In general, CEP does not change the overall structure of the electric field waveform, because the variation of the envelope function indicated by the dashed line in Fig. 1-8 is much slower than the oscillation of carrier wave.

Recent advances [72] in the ultrashort laser pulse technologies enabled us to generate a laser pulse which has only a few cycles of the oscillation of the carrier wave within its pulse duration. In the case of this few-cycle pulse, the waveform of the laser electric field is strongly modified by CEP. Figures 1-8(e) and 1-8(f) show the electric field of the laser pulse at ϕ_{abs} = 0 and 90°, respectively, when their pulse durations are Δt = 4 fs and their wavelengths are λ = 800 nm. The laser electric fields show that the waveform is "cosine-like" shape at ϕ_{abs} = 0° and "sine-like" shape at ϕ_{abs} = 90°. Therefore, the CEP dependence of the ionization and the dissociation in intense few-cycle laser fields becomes the attractive research subjects in recent years [69-71,73-85]. For example, the directional D^+ ejection from C_2D_2 with respect to the laser polarization direction has been controlled by the CEP as shown in Fig. 1-9 [84].

The CEP of each laser pulse is quasi-random shot-by-shot. One of the methods to investigate the CEP dependence is stabilization of the CEP of each laser shot by frequency

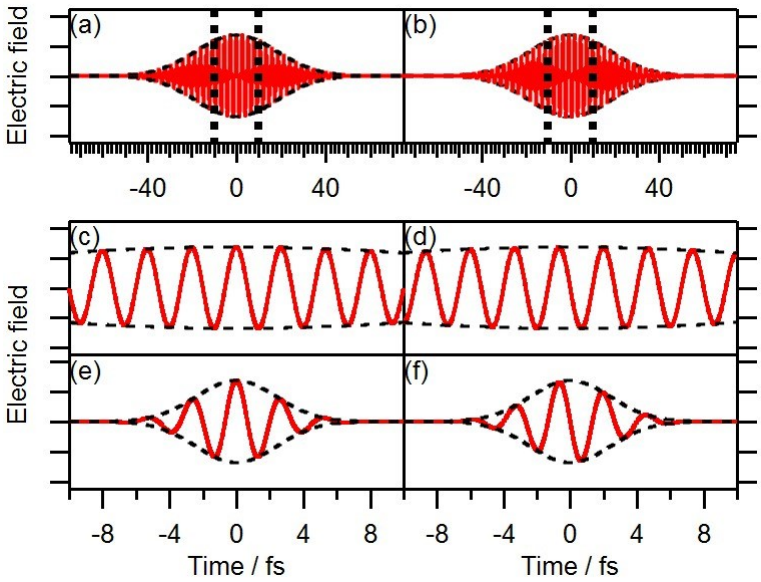

Fig.1-8 (a) 800 nm laser pulse whose pulse duration is 30 fs at ϕ_{abs}= 0°. (b) 800 nm laser pulse whose pulse duration is 30 fs at ϕ_{abs}= 90°. (c) Magnification view of (a). (d) Magnification view of (b). a) 800 nm laser pulse whose pulse duration is 4 fs at ϕ_{abs}= 0°. (b) 800 nm laser pulse whose pulse duration is 4 fs at ϕ_{abs}= 90°.

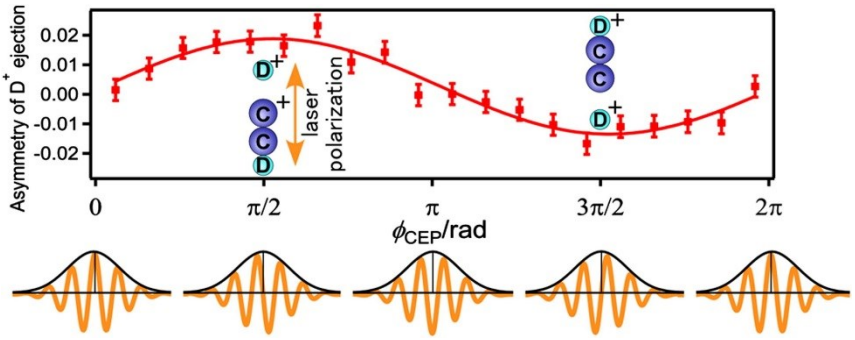

Fig.1-9 Asymmetric D^+ emission from C_2D_2 by few-cycle pulses. [S. Miura, *et al.*, *Chem. Phys. Lett.* 595–596, **61** (2014). Graphical abstract.]

comb technique, that is, f-2f interferometer and the feedback of its result to the laser system in order to lock the CEP [70,86,87]. Another method is CEP-tagging, in which the CEP of each laser shot at an apparatus called a phasemeter is recorded on the basis of CEP dependence of rescattered photoelectron in an intense linearly polarized laser field [73,88]. However, it is difficult to determine the absolute CEP at the laser-molecule interaction point. CEP is varied by the propagation of the laser pulse through dispersed media.

1-4. Coulombic potential effect

As the first approximation, the Coulombic field of an atomic or molecular ion generated by strong field ionization has been neglected, compared with the intense laser field. In the theory of SFA described in Sec. 1-2-2, the final state of photoelectrons is assumed to be Volkov state. In the theory of simple man's model described in Sec. 1-2-3, the Newton's equation of motion of a photoelectron only in the laser field is solved. These theories have succeeded in the explanation of many strong field phenomena. However, it is known that the Coulombic potential of the ion core cannot be neglected in some cases, such as Coulomb focusing [37-39] described in Sec. 1-2-3.

One example is Coulomb asymmetry [89], in which four-fold symmetry of a photoelectron angular distribution in elliptically polarized laser field is broken. When the Coulombic field of ion core is not taken into account, the photoelectron angular distributions are symmetric with respect to the major and the minor axes of the laser field. However, the experimental photoelectron angular distributions exhibit a peak at the angle which is deviated from the minor axis.

Recently, low energy photoelectrons unexpected on the basis of SFA and the simple man's model are observed in ionization of atoms by intense mid-infrared laser pulses [90,91]. In this low energy structure (LES), Coulombic potential is considered to play an important role [92,93].

1-5. Effect of molecular alignment

Because of the non-perturbative nature of strong field phenomena, they are strongly dependent on the alignment of molecular axes with respect to the laser polarization direction. For example, the tunnel ionization probability is sensitive to the alignment, indicated by MO-ADK theory.

In order to investigate the alignment effect, two methods are known; (i) molecular alignment by the relatively weak pump pulse [3], and (ii) measurement of the fragment recoil assuming axial recoil approximation [94]. In the case of (i), molecules are forced by the torque induced by the laser electric field, leading to molecular alignment. Alignment of molecular axis has been realized not only within the laser pulse whose duration is longer than the rotational period, but also in field-free condition through the revival of a rotational wavepacket prepared by femtosecond laser pulses. In the case of (ii), the direction of the molecular axis can be derived as the emitting direction of photo ions, assuming the dissociation process is faster than the molecular rotation. These techniques have been applied to investigate alignment-dependent tunnel ionization probability [95,96], photoelectron angular distributions in the molecular-frame [97-99], and polarization-dependence of dissociation dynamics [100].

1-6. Ionization to electronically excited states in intense laser fields

According to ADK theory, the ionization probability of strong field ionization is exponentially decreases as the ionization energy increases. This tendency suggests that ionization to electronic ground state, that is, ionization from highest occupied molecular orbital (HOMO) is dominant in intense laser fields. Therefore, by using HHG, imaging methods of HOMO have been proposed [101-105]. However, recently, role of ionization to electronically excited states, that is, ionization from lower-lying orbitals becomes an attractive research subject.

HHG from lower-lying orbitals is expected to produce high energy photons because of cutoff law, suggesting that it can be identified by the enhancement of high energy photons. Consequently, because the alignment dependence and internuclear-distance dependence of tunnel ionization probability are different among the MOs, HHG from lower-lying orbitals has been identified in HHG from aligned molecules [106,107] and vibrational-motion-excited molecules [108]. The electronically excited states of cations prepared by pump laser pulses have also been identified by the probe pulses [109,110]. Tunnel ionization to electronically excited states have also been identified by laser induced fluorescence (LIF) [111-113].

When electronically excited states of molecular ions are prepared, dissociation may

occur. Dissociative ionization of molecules in intense laser fields indicates that electronically excited states are prepared. Recently, dissociative ionization of molecules has been investigated by photoelectron-photoion coincidence (PEPICO) measurements [98,99,114-118]. Through the investigation of dissociative ionization of ethanol by using PEPICO momentum imaging (MI) [114,115,118], the two pathways to prepare electronically excited states of ethanol cation were revealed; (i) MPI to the electronically excited states, and (ii) MPI to the electronic ground state and subsequent one-photon or multiphoton electronic excitation to the electronically excited states. Subsequent electronic excitation of cations during the laser pulse plays an important role in many recent studies (e.g., [119]).

1-7. This thesis

1-7-1. Determination of absolute CEP by circularly-polarized few-cycle pulses

In the thesis study, I experimentally demonstrated that absolute CEP at the laser-molecule interaction point can be determined by using circularly polarized few-cycle laser pulses. CEP dependence of angle-resolved energy spectra of the photoelectron generated by tunnel ionization of Ar is investigated by CEP-tagging method. On the basis of ADK theory and simple man's model, absolute CEP can be determined without numerical calculation. The effect of depletion of neutral Ar atoms during the laser pulse and that of Coulombic potential, similar to Coulomb asymmetry, are also examined.

1-7-2. Dissociative ionization of methanol in intense UV laser fields

Furthermore, I investigated dissociative ionization of methanol in intense UV laser fields by PEPICO-MI. The electronic states of methanol cation at the moment of the photoelectron emission are identified by channel-specific photoelectron angular distribution. Assuming the axial recoil approximation, orientation-resolved photoelectron angular distribution is also examined.

1-7-3. Structure of this thesis

In Chapter 2, I describe theory of tunnel ionization and simple man's model. In Chapter 3, the character and generation of femtosecond and few-cycle pulses are briefly summarized. Particularly, the propagation of a few-cycle laser pulse in dispersive media, leading to the variation of its CEP and pulse duration, is described.

In Chapter 4, I demonstrate absolute CEP can be determined by angle-resolved photoelectron spectra in circularly polarized few-cycle laser fields.

In Chapter 5, the experimental setup and the data analysis of PEPICO-MI performed in the following chapters are described. In Chapter 6, the ionization and subsequent excitation pathways to electronically excited states of a methanol cation are revealed by

channel-specific photoelectron angular distributions in laboratory-frame and molecular-frame. In Chapter 7, the orientation dependence of photoelectron angular distribution is investigated. In Chapter 8, the laser intensity dependence of the ionization and the excitation pathways is clarified by channel-specific photoelectron angular distribution.

In Chapter 9, I summarized this thesis. Throughout this thesis, the SI units system is used unless stated otherwise.

2. Theory of tunnel ionization and simple man's model

2-1. ADK theory

2-1-1. Tunnel ionization rate

Ammosov, Delone and Krainov [31] derived the tunnel ionization rate W of hydrogen-like atoms by a constant DC electric field **E**. In this section, the derivation [31,120] of the ADK ionization rate is summarized.

The coordinate system is defined so that z axis is parallel to the electric field and the electron is ejected towards +z direction, i.e., $\mathbf{E}\cdot\hat{\mathbf{z}} = -|\mathbf{E}|$. The tunnel ionization rate W can be calculated as

$$W = \int_S \mathbf{j}\cdot d\mathbf{S} = \int_S j_z dS_z, \tag{2-1}$$

where **j** is a current density of a wavefunction ψ of the electron

$$\mathbf{j} = \frac{i\hbar}{2m_e}\left(\Psi\nabla\Psi^* - \Psi^*\nabla\Psi\right),\ j_z = \frac{i\hbar}{2m_e}\left(\Psi\frac{\partial\Psi^*}{\partial z} - \Psi^*\frac{\partial\Psi}{\partial z}\right) \tag{2-2}$$

and S is a plane perpendicular to the electric field.

Schrodinger equation of an electron whose energy is -I_p in the Coulombic field of the nuclei and the laser field as

$$\left[-\frac{\hbar^2}{2m_e}\nabla^2 - \frac{1}{4\pi\varepsilon_0}\frac{Ze^2}{r} - e|\mathbf{E}|z\right]\Psi = -I_p\Psi$$

is reduced to

$$\nabla^2\Psi + \left[-\frac{\kappa^2}{\hbar^2} + \frac{2Zm_e e^2}{4\pi\varepsilon_0\hbar^2}\frac{1}{r} + \frac{2m_e e|\mathbf{E}|}{\hbar^2}z\right]\Psi = 0, \tag{2-3}$$

where $\kappa = \sqrt{2m_e I_p}$ and Z is a charge of an atom after ionization, that is, Z = 1 when neutral atom is ionized. When the electron is close enough to the ion core to neglect the term including $|\mathbf{E}|z$, the asymptotic solution can be given by

$$\Psi = R_{n^*l^*}(r)Y_{lm}(\theta,\phi). \tag{2-4}$$

An effective principal quantum number is

$$n^* = \sqrt{\frac{Z^2 m_e e^4}{2(4\pi\varepsilon_0)^2\hbar^2 I_p}} = \frac{Zm_e e^2}{4\pi\varepsilon_0\hbar\kappa}, \tag{2-5}$$

and an effective angular momentum quantum number is

$$l^* = \begin{cases} 0, & l << n \\ n_0^* - 1, & \text{otherwise} \end{cases}, \tag{2-6}$$

where n_0^* is the effective principal quantum number for the ground state, that is, n_0^* is identical to n^* unless ionization from excited state is considered. The normalized radial wavefunction can be expressed by Laguerre polynomials as

$$R_{n^*l^*}(r)=\sqrt{\frac{\Gamma(n^*-l^*)}{2n^*\left[\Gamma(n^*+l^*+1)\right]^3}}\left(\frac{2\kappa}{\hbar}\right)^{\frac{3}{2}}\left(\frac{2\kappa}{\hbar}r\right)^{l^*}\mathrm{e}^{-\frac{\kappa}{\hbar}r}L_{n^*+l^*}^{2l^*+1}\left(\frac{2\kappa}{\hbar}r\right).$$

When the electron is far from the ion core so that the Coulombic force is small, the radial wavefunction is approximated as

$$\begin{aligned}R_{n^*l^*}(r)&\approx\sqrt{\frac{\Gamma(n^*-l^*)}{2n^*\left[\Gamma(n^*+l^*+1)\right]^3}}\left(\frac{2\kappa}{\hbar}\right)^{\frac{3}{2}}\frac{\Gamma(n^*+l^*+1)}{\Gamma(n^*-l^*)}\left(\frac{2\kappa}{\hbar}r\right)^{n^*-1}\mathrm{e}^{-\frac{\kappa}{\hbar}r}\\&=\frac{2^{n^*}}{\sqrt{n^*\Gamma(n^*+l^*+1)\Gamma(n^*-l^*)}}\left(\frac{\kappa}{\hbar}\right)^{\frac{3}{2}}\left(\frac{\kappa}{\hbar}r\right)^{n^*-1}\mathrm{e}^{-\frac{\kappa}{\hbar}r},\end{aligned}$$

by taking only the highest order term of Laguerre polynomials. By defining

$$C_{n^*l^*}=\frac{2^{n^*}}{\sqrt{n^*\Gamma(n^*+l^*+1)\Gamma(n^*-l^*)}}, \tag{2-7}$$

the asymptotic wavefunction (Eq. (2-4)) is rewritten as

$$\Psi\approx C_{n^*l^*}\left(\frac{\kappa}{\hbar}\right)^{\frac{3}{2}}\left(\frac{\kappa}{\hbar}r\right)^{n^*-1}\mathrm{e}^{-\frac{\kappa}{\hbar}r}\sqrt{\frac{2l+1}{2}\frac{(l-|m|)!}{(l+|m|)!}}P_l^{|m|}(\cos\theta)\frac{(-)^{\frac{m+|m|}{2}}}{\sqrt{2\pi}}\mathrm{e}^{im\phi}. \tag{2-8}$$

The spatial coordinates of the wavefunction is transformed from polar or Cartesian coordinates to parabolic coordinates (ξ, η, ϕ) as

$$\begin{aligned}&\xi=r(1+\cos\theta)=\sqrt{x^2+y^2+z^2}+z\\&\eta=r(1-\cos\theta)=\sqrt{x^2+y^2+z^2}-z\\&r=\frac{\xi+\eta}{2},z=\frac{\xi-\eta}{2},\cos\theta=\frac{\xi-\eta}{\xi+\eta},\sin\theta=\frac{2\sqrt{\xi\eta}}{\xi+\eta}\end{aligned}. \tag{2-9}$$

In this coordinate system, the Laplacian is expressed as

$$\nabla^2=\frac{4}{\xi+\eta}\left[\frac{\partial}{\partial\xi}\left(\xi\frac{\partial}{\partial\xi}\right)+\frac{\partial}{\partial\eta}\left(\eta\frac{\partial}{\partial\eta}\right)\right]+\frac{1}{\xi\eta}\frac{\partial^2}{\partial\phi^2}. \tag{2-10}$$

Therefore, Eq. (2-3) is rewritten as

$$\frac{4}{\xi+\eta}\left[\frac{\partial}{\partial\xi}\left(\xi\frac{\partial\Psi}{\partial\xi}\right)+\frac{\partial}{\partial\eta}\left(\eta\frac{\partial\Psi}{\partial\eta}\right)\right]+\frac{1}{\xi\eta}\frac{\partial^2\Psi}{\partial\phi^2}+\left[-\frac{\kappa^2}{\hbar^2}+\frac{4Zm_\mathrm{e}e^2}{4\pi\varepsilon_0\hbar^2}\frac{1}{\xi+\eta}-\frac{m_\mathrm{e}e|\mathbf{E}|}{\hbar^2}(\xi-\eta)\right]\Psi=0. \tag{2-11}$$

By separation of variable of the wavefunction

$$\Psi=C_{n^*l^*}\left(\frac{\kappa}{\hbar}\right)^{\frac{3}{2}}\varphi(\xi)\chi(\eta)\frac{1}{\sqrt{2\pi\xi\eta}}\mathrm{e}^{im\phi}, \tag{2-12}$$

Eq. (2-11) can be transformed as

$$\frac{1}{\varphi}\left(\xi\varphi''+\frac{\varphi}{4\xi}\right)+\frac{1}{\chi}\left(\eta\chi''+\frac{\chi}{4\eta}\right)-\frac{m^2}{4}\left(\frac{1}{\xi}+\frac{1}{\eta}\right)+\left[-\frac{\kappa^2}{4\hbar^2}(\xi+\eta)+\frac{n^*\kappa}{\hbar}-\frac{m_e e|\mathbf{E}|}{4\hbar^2}\left(\xi^2-\eta^2\right)\right]=0$$

$$\frac{\xi\varphi''}{\varphi}+\left(-\frac{\kappa^2}{4\hbar^2}\xi+\frac{1-m^2}{4\xi}-\frac{m_e eE}{4\hbar^2}\xi^2\right)+\frac{\eta\chi''}{\chi}+\left(-\frac{\kappa^2}{4\hbar^2}\eta+\frac{1-m^2}{4\eta}+\frac{m_e e|\mathbf{E}|}{4\hbar^2}\eta^2\right)+\frac{n*\kappa}{\hbar}=0\,.$$

By introducing β_1 and β_2 which satisfy $\beta_1+\beta_2=\frac{n^*\kappa}{\hbar}$, the equations

$$\varphi''+\left(-\frac{\kappa^2}{4\hbar^2}+\frac{\beta_1}{\xi}+\frac{1-m^2}{4\xi^2}-\frac{m_e e|\mathbf{E}|}{4\hbar^2}\xi\right)\varphi=0 \tag{2-13}$$

$$\chi''+\left(-\frac{\kappa^2}{4\hbar^2}+\frac{\beta_2}{\eta}+\frac{1-m^2}{4\eta^2}+\frac{m_e e|\mathbf{E}|}{4\hbar^2}\eta\right)\chi=0 \tag{2-14}$$

are derived. In parabolic coordinates, Eq. (2-8) becomes

$$\Psi=C_{n^*l^*}\left(\frac{\kappa}{\hbar}\right)^{\frac{3}{2}}\left(\frac{\kappa}{\hbar}\frac{\xi+\eta}{2}\right)^{n^*-1}\mathrm{e}^{-\frac{\kappa}{2\hbar}(\xi+\eta)}\sqrt{\frac{2l+1}{2}\frac{(l-|m|)!}{(l+|m|)!}}P_l^{|m|}\left(\frac{\xi-\eta}{\xi+\eta}\right)\frac{(-)^{\frac{m+|m|}{2}}}{\sqrt{2\pi}}\mathrm{e}^{im\phi}\,. \tag{2-15}$$

When the electron is close to z axis, the approximation

$$P_l^{|m|}(\cos\theta)\approx\frac{1}{2^{|m|}(|m|)!}\frac{(l+|m|)!}{(l-|m|)!}\theta^{|m|}$$

is held due to $\theta\approx\sin\theta$. Therefore, the asymptotic wavefunction becomes

$$\Psi=C_{n^*l^*}\left(\frac{\kappa}{\hbar}\right)^{\frac{3}{2}}\left(\frac{\kappa}{\hbar}\frac{\xi+\eta}{2}\right)^{n^*-1}\mathrm{e}^{-\frac{\kappa}{2\hbar}(\xi+\eta)}\sqrt{\frac{2l+1}{2}\frac{(l+|m|)!}{(l-|m|)!}}\frac{1}{2^{|m|}(|m|)!}\left(\frac{2\sqrt{\xi\eta}}{\xi+\eta}\right)^{|m|}\frac{(-)^{\frac{m+|m|}{2}}}{\sqrt{2\pi}}\mathrm{e}^{im\phi}\,.$$

Because the electron is assumed to be ejected towards $+z$ direction, and to be close to z axis, ξ and η satisfy the relation $\xi>>\eta$. The asymptotic wavefunction becomes

$$\begin{aligned}\Psi&=C_{n^*l^*}\left(\frac{\kappa}{\hbar}\right)^{\frac{3}{2}}\left(\frac{\kappa}{\hbar}\frac{\xi}{2}\right)^{n^*-1}\mathrm{e}^{-\frac{\kappa}{2\hbar}(\xi+\eta)}\sqrt{\frac{2l+1}{2}\frac{(l+|m|)!}{(l-|m|)!}}\frac{1}{(|m|)!}\left(\frac{\eta}{\xi}\right)^{\frac{|m|}{2}}\frac{(-)^{\frac{m+|m|}{2}}}{\sqrt{2\pi}}\mathrm{e}^{im\phi}\\&=C_{n^*l^*}\left(\frac{\kappa}{\hbar}\right)^{\frac{3}{2}}\left(\frac{\kappa}{\hbar}\right)^{n^*-1}\left(\frac{\xi}{2}\right)^{n^*-1-\frac{|m|}{2}}\mathrm{e}^{-\frac{\kappa}{2\hbar}\xi}\sqrt{\frac{2l+1}{2}\frac{(l+|m|)!}{(l-|m|)!}}\frac{1}{2^{\frac{|m|}{2}}(|m|)!}\eta^{\frac{|m|}{2}}\mathrm{e}^{-\frac{\kappa}{2\hbar}\eta}\frac{(-)^{\frac{m+|m|}{2}}}{\sqrt{2\pi}}\mathrm{e}^{im\phi}\end{aligned}\,. \tag{2-16}$$

By comparing Eqs. (2-12) and (2-16),

$$\varphi(\xi)=\sqrt{2}\left(\frac{\kappa}{\hbar}\right)^{n^*-1}\left(\frac{\xi}{2}\right)^{n^*-\frac{|m|+1}{2}}\mathrm{e}^{-\frac{\kappa}{2\hbar}\xi}\sqrt{\frac{2l+1}{2}\frac{(l+|m|)!}{(l-|m|)!}}\frac{1}{2^{\frac{|m|}{2}}(|m|)!} \tag{2-17}$$

$$\chi(\eta)=\eta^{\frac{|m|+1}{2}}\mathrm{e}^{-\frac{\kappa}{2\hbar}\eta} \tag{2-18}$$

are obtained. Using Eqs. (2-13) and (2-14), β_1 and β_2 are derived as

$$\begin{cases} \beta_1 = \dfrac{n^*\kappa}{\hbar} - \dfrac{\kappa}{2\hbar}\left(|m|+1\right) = \dfrac{\kappa}{2\hbar}\left(2n^* - |m| - 1\right) \\ \beta_2 = \dfrac{\kappa}{2\hbar}\left(|m|+1\right) \end{cases}. \tag{2-19}$$

On the one hand, using $\rho = \sqrt{x^2 + y^2}$, η is approximated as

$$\eta = \sqrt{\rho^2 + z^2} - z \approx \frac{\rho^2}{2z} \approx \frac{\rho^2}{\xi}. \tag{2-20}$$

Assuming ξ takes a constant value when the electron is on the plane S and is close to z axis, the small area dS in Eq. (2-2) can be expressed as

$$\mathrm{d}S = \rho \mathrm{d}\rho \mathrm{d}\phi = \frac{1}{2}\xi \mathrm{d}\eta \mathrm{d}\phi. \tag{2-21}$$

Substituting Eq. (2-21) into Eq. (2-2), the current density is rewritten as

$$j_z = \frac{\mathrm{i}\hbar}{m_\mathrm{e}}\left(\Psi\frac{\partial\Psi^*}{\partial\xi} - \Psi^*\frac{\partial\Psi}{\partial\xi}\right) = \frac{\mathrm{i}\hbar}{m_\mathrm{e}}\frac{1}{2\pi}\frac{\chi^2}{\eta}\left[\frac{\varphi}{\sqrt{\xi}}\frac{\mathrm{d}}{\mathrm{d}\xi}\left(\frac{\varphi^*}{\sqrt{\xi}}\right) - \frac{\varphi^*}{\sqrt{\xi}}\frac{\mathrm{d}}{\mathrm{d}\xi}\left(\frac{\varphi}{\sqrt{\xi}}\right)\right].$$
$$= \frac{\mathrm{i}\hbar}{2\pi m_\mathrm{e}}\frac{\chi^2}{\xi\eta}\left(\varphi\frac{\mathrm{d}\varphi^*}{\mathrm{d}\xi} - \varphi^*\frac{\mathrm{d}\varphi}{\mathrm{d}\xi}\right)$$

When the electron is close to z axis, $\eta \approx 0$. Therefore, $\chi(\eta)$ is the same as in the asymptotic range (Eq. (2-18)), resulting in

$$W = \int_0^\infty\int_0^{2\pi} j_z \frac{1}{2}\xi \mathrm{d}\eta \mathrm{d}\phi = \frac{\mathrm{i}\hbar}{4\pi m_\mathrm{e}} C_{n^*l^*}^2 \left(\frac{\kappa}{\hbar}\right)^3 \left(\varphi\frac{\mathrm{d}\varphi^*}{\mathrm{d}\xi} - \varphi^*\frac{\mathrm{d}\varphi}{\mathrm{d}\xi}\right)\int_0^\infty \frac{\chi^2}{\eta}\mathrm{d}\eta \int_0^{2\pi}\mathrm{d}\phi$$
$$= \frac{\mathrm{i}\hbar}{2m_\mathrm{e}} C_{n^*l^*}^2 \left(\frac{\kappa}{\hbar}\right)^3 \left(\varphi\frac{\mathrm{d}\varphi^*}{\mathrm{d}\xi} - \varphi^*\frac{\mathrm{d}\varphi}{\mathrm{d}\xi}\right)\int_0^\infty \eta^{|m|}\mathrm{e}^{-\frac{\kappa}{\hbar}\eta}\mathrm{d}\eta$$
$$W = \frac{\mathrm{i}\hbar C_{n^*l^*}^2}{2m_\mathrm{e}}\left(\varphi\frac{\mathrm{d}\varphi^*}{\mathrm{d}\xi} - \varphi^*\frac{\mathrm{d}\varphi}{\mathrm{d}\xi}\right)\frac{(|m|)!}{\left(\frac{\kappa}{\hbar}\right)^{|m|-2}}. \tag{2-22}$$

Using WKB approximation with a quasi-momentum

$$p = \sqrt{\left|\frac{\kappa^2}{4\hbar^2} - \frac{\beta_1}{\xi} - \frac{1-m^2}{4\xi^2} - \frac{m_\mathrm{e}e|\mathbf{E}|}{4\hbar^2}\xi\right|}, \tag{2-23}$$

the wavefunction can be expressed as

$$\varphi(\xi) = \begin{cases} \mathrm{i}\dfrac{C}{\sqrt{p}}\exp\left(\mathrm{i}\displaystyle\int_{\xi_0}^{\xi} p\mathrm{d}\xi - \mathrm{i}\frac{\pi}{4}\right) & (\xi > \xi_0) \\ \dfrac{C}{\sqrt{p}}\exp\left(-\displaystyle\int_{\xi_0}^{\xi} p\mathrm{d}\xi\right) & (\xi < \xi_0) \end{cases} \tag{2-24}$$

in the ξ range around turning point ξ_0, i.e., $p = 0$. In the range of $\xi > \xi_0$,

$$\frac{\mathrm{d}\varphi}{\mathrm{d}\xi} = \left(-\frac{1}{2p}\frac{\mathrm{d}p}{\mathrm{d}\xi} + \mathrm{i}p\right)\varphi.$$

Substituting this into Eq. (2-22), the ionization rate becomes

$$W=\frac{\mathrm{i}\hbar C_{n^*l^*}^2}{2m_\mathrm{e}}\left[\left(-\frac{1}{2p}\frac{\mathrm{d}p}{\mathrm{d}\xi}-\mathrm{i}p\right)-\left(-\frac{1}{2p}\frac{\mathrm{d}p}{\mathrm{d}\xi}+\mathrm{i}p\right)\right]|\varphi|^2\frac{(|m|)!}{\left(\frac{\kappa}{\hbar}\right)^{|m|-2}}=\frac{\hbar C_{n^*l^*}^2}{m_\mathrm{e}}\frac{|C|^2(|m|)!}{\left(\frac{\kappa}{\hbar}\right)^{|m|-2}}. \tag{2-25}$$

In the range of $\xi<\xi_0$ and $\frac{z}{\kappa^2}\ll\xi\ll\frac{\kappa^2}{e|\mathbf{E}|}$, where $\frac{z}{\xi}\ll\kappa^2$ and $e|\mathbf{E}|\xi\ll\kappa^2$ are satisfied, the quasi-momentum Eq. (2-23) is approximated as

$$p=\frac{\kappa}{2\hbar}\sqrt{\left|1-\frac{m_\mathrm{e}e|\mathbf{E}|}{\kappa^2}\xi-\frac{4\hbar^2\beta_1}{\kappa^2\xi}-\frac{\hbar^2\left(1-m^2\right)}{\kappa^2\xi^2}\right|}\approx\frac{\kappa}{2\hbar}\left[\sqrt{1-\frac{m_\mathrm{e}e|\mathbf{E}|}{\kappa^2}\xi}\left(1-\frac{1}{2}\frac{1}{1-\frac{m_\mathrm{e}e|\mathbf{E}|}{\kappa^2}\xi}\frac{4\hbar^2\beta_1}{\kappa^2\xi}\right)\right].$$

$$=\frac{\kappa}{2\hbar}\sqrt{1-\frac{m_\mathrm{e}e|\mathbf{E}|}{\kappa^2}\xi}-\frac{\hbar\beta_1}{\kappa\xi\sqrt{1-\frac{m_\mathrm{e}e|\mathbf{E}|}{\kappa^2}\xi}}$$

Thus, Eq. (2-24) becomes

$$\varphi(\xi)=\frac{C}{\sqrt{\frac{\kappa}{2\hbar}\sqrt{1-\frac{m_\mathrm{e}e|\mathbf{E}|}{\kappa^2}\xi}}}\exp\left[-\int_{\xi_0}^{\xi}\left(\frac{\kappa}{2\hbar}\sqrt{1-\frac{m_\mathrm{e}e|\mathbf{E}|}{\kappa^2}\xi}-\frac{\hbar\beta_1}{\kappa\xi\sqrt{1-\frac{m_\mathrm{e}e|\mathbf{E}|}{\kappa^2}\xi}}\right)\mathrm{d}\xi\right].$$

By defining $t=\sqrt{1-\frac{m_\mathrm{e}e|\mathbf{E}|}{\kappa^2}\xi}\approx1-\frac{m_\mathrm{e}e|\mathbf{E}|}{2\kappa^2}\xi$, that is, $\xi=\frac{1-t^2}{m_\mathrm{e}e|\mathbf{E}|/\kappa^2}$,

$$\int_{\xi_0}^{\xi}\frac{1}{\xi\sqrt{1-\frac{m_\mathrm{e}e|\mathbf{E}|}{\kappa^2}\xi}}\mathrm{d}\xi=\int_0^t\frac{2\mathrm{d}t}{t^2-1}=\left[\ln\left|\frac{t-1}{t+1}\right|\right]_0^t\approx\ln\frac{\frac{m_\mathrm{e}e|\mathbf{E}|}{2\kappa^2}\xi}{2-\frac{m_\mathrm{e}e|\mathbf{E}|}{2\kappa^2}\xi},$$

is obtained, resulting that

$$\varphi(\xi)=\frac{C}{\sqrt{\frac{\kappa}{2\hbar}\sqrt{1-\frac{m_\mathrm{e}e|\mathbf{E}|}{\kappa^2}\xi}}}\exp\left\{-\left[-\frac{\kappa}{2\hbar}\frac{\kappa^2}{m_\mathrm{e}e|\mathbf{E}|}\frac{2}{3}\left(1-\frac{m_\mathrm{e}e|\mathbf{E}|}{\kappa^2}\xi\right)^{\frac{3}{2}}\right]_{\xi_0}^{\xi}+\frac{\hbar\beta_1}{\kappa}\ln\frac{\frac{m_\mathrm{e}e|\mathbf{E}|}{2\kappa^2}\xi}{2-\frac{m_\mathrm{e}e|\mathbf{E}|}{\kappa^2}\xi}\right\}$$

$$=\frac{C}{\sqrt{\frac{\kappa}{2\hbar}\sqrt{1-\frac{m_\mathrm{e}e|\mathbf{E}|}{\kappa^2}\xi}}}\left(\frac{\frac{m_\mathrm{e}e|\mathbf{E}|}{2\kappa^2}\xi}{2-\frac{m_\mathrm{e}e|\mathbf{E}|}{\kappa^2}\xi}\right)^{\frac{\hbar\beta_1}{\kappa}}\exp\left[\frac{\kappa^3}{3\hbar m_\mathrm{e}e|\mathbf{E}|}\left(1-\frac{m_\mathrm{e}e|\mathbf{E}|}{\kappa^2}\xi\right)^{\frac{3}{2}}\right]$$

$$\varphi(\xi)\approx C\sqrt{\frac{2\hbar}{\kappa}}\left(\frac{m_\mathrm{e}e|\mathbf{E}|}{4\kappa^2}\xi\right)^{n^*-\frac{|m|+1}{2}}\exp\left(\frac{\kappa^3}{3\hbar m_\mathrm{e}e|\mathbf{E}|}-\frac{\kappa}{2\hbar}\xi\right) \tag{2-26}$$

is derived.

By comparing the solution (Eq. (2-26)) obtained by WKB approximation and the

asymptotic solution (Eq. (2-17)), C is obtained as

$$C=\left(\frac{\kappa}{\hbar}\right)^{n^*-\frac{1}{2}}\left(\frac{2\kappa^2}{m_e e|\mathbf{E}|}\right)^{n^*-\frac{|m|+1}{2}}\exp\left(-\frac{\kappa^3}{3\hbar m_e e|\mathbf{E}|}\right)\sqrt{\frac{2l+1}{2}\frac{(l+|m|)!}{(l-|m|)!}}\frac{1}{2^{\frac{|m|}{2}}(|m|)!}.$$

Consequently, from Eq. (2-25), the ionization rate W is derived as

$$W=\frac{\hbar C_{n^*l^*}^2}{m_e}\frac{(|m|)!}{\left(\frac{\kappa}{\hbar}\right)^{|m|-2}}\left(\frac{\kappa}{\hbar}\right)^{2n^*-1}\left(\frac{2\kappa^2}{m_e e|\mathbf{E}|}\right)^{2n^*-|m|-1}\exp\left(-\frac{2\kappa^3}{3\hbar m_e e|\mathbf{E}|}\right)\frac{2l+1}{2}\frac{(l+|m|)!}{(l-|m|)!}\frac{1}{2^{|m|}((|m|)!)^2}$$

$$=\frac{1}{\hbar}\frac{\kappa^2}{2m_e}C_{n^*l^*}^2\frac{2l+1}{2^{|m|}(|m|)!}\frac{(l+|m|)!}{(l-|m|)!}\left(\frac{2\kappa^3}{\hbar m_e e|\mathbf{E}|}\right)^{2n^*-|m|-1}\exp\left(-\frac{2\kappa^3}{3\hbar m_e e|\mathbf{E}|}\right)$$

$$W=\frac{I_p}{\hbar}\frac{2^{2n^*}}{n^*\Gamma(n^*+l^*+1)\Gamma(n^*-l^*)}\frac{2l+1}{2^{|m|}(|m|)!}\frac{(l+|m|)!}{(l-|m|)!}\left(\frac{2\sqrt{8m_e I_p^{\,3}}}{\hbar e|\mathbf{E}|}\right)^{2n^*-|m|-1}\exp\left(-\frac{2\sqrt{8m_e I_p^{\,3}}}{3\hbar e|\mathbf{E}|}\right). \tag{2-27}$$

2-1-2. Initial transverse momentum distribution for circularly polarized pulses

Delone and Krainov [121] also derived the initial momentum distribution of the electron at the moment of the tunneling within the adiabatic theory.

When the tunneling occurs at $t = 0$, the transition amplitude from an initial state i to a final state f can be expressed as

$$A_{if}=\exp\left\{\frac{\mathrm{i}}{\hbar}\int_0^{t_0}\left[\varepsilon_f(t)-\varepsilon_i(t)\right]\mathrm{d}t\right\} \tag{2-28}$$

by Landau-Dykhne adiabatic approximation [122], where ε_f and ε_i are the energies of states i and f, respectively, and t_0 is turning point at which the relation

$$\varepsilon_f(t_0)=\varepsilon_i(t_0) \tag{2-29}$$

is satisfied. The transition probability is derived as

$$w_{if}=\exp\left(-\frac{2}{\hbar}\mathrm{Im}S\right), \tag{2-30}$$

where S is an action

$$S=\int_0^{t_0}\left[\varepsilon_f(t)-\varepsilon_i(t)\right]\mathrm{d}t. \tag{2-31}$$

The energy of the initial state i is set to be

$$\varepsilon_i(t_0)=-I_p. \tag{2-32}$$

When the Coulombic potential of the ionic core, which is already taken into account in Sec. 2-1-1, is neglected, the energy of the final state f is

$$\varepsilon_f(t)=\frac{1}{2m_e}\left[\mathbf{p}+e\mathbf{A}(t)\right]^2, \tag{2-33}$$

where $\mathbf{p}=m_e\dot{\mathbf{x}}(t)-e\mathbf{A}(t)$ is generalized momentum, $\mathbf{x}(t)$ position and $\mathbf{A}(t)$ vector potential

of the laser field. The generalized momentum is considered to be conserved during the tunneling.

Tunnel ionization in the circularly polarized DC laser field

$$\begin{cases} \mathbf{E}(t) = |\mathbf{E}|\left[\hat{\mathbf{x}}\cos(\omega t+\phi)+\hat{\mathbf{y}}\sin(\omega t+\phi)\right] \\ \mathbf{A}(t) = -\dfrac{|\mathbf{E}|}{\omega}\left[\hat{\mathbf{x}}\sin(\omega t+\phi)-\hat{\mathbf{y}}\cos(\omega t+\phi)\right] \end{cases} \tag{2-34}$$

is considered. Assuming long wavelength (i.e. $\omega \sim 0$), Eq. (2-33) becomes

$$\begin{aligned} \varepsilon_f(t) &= \frac{1}{2m_\mathrm{e}}\left\{\left[p_\mathrm{x}-\frac{e|\mathbf{E}|}{\omega}\sin(\omega t+\phi)\right]^2+\left[p_\mathrm{y}+\frac{e|\mathbf{E}|}{\omega}\cos(\omega t+\phi)\right]^2+{p_\mathrm{z}}^2\right\} \\ &\approx \frac{1}{2m_\mathrm{e}}\left\{\left[p_\mathrm{x}-\frac{e|\mathbf{E}|\sin\phi}{\omega}-e|\mathbf{E}|(\cos\phi)t\right]^2+\left[p_\mathrm{y}+\frac{e|\mathbf{E}|\cos\phi}{\omega}-e|\mathbf{E}|(\sin\phi)t\right]^2+{p_\mathrm{z}}^2\right\} \\ \varepsilon_f(t) &\approx \frac{1}{2m_\mathrm{e}}\left[e^2|\mathbf{E}|^2t^2-2e|\mathbf{E}|\left(p_\mathrm{x}\cos\phi+p_\mathrm{y}\sin\phi\right)t+{p_\mathrm{x}}^2+{p_\mathrm{y}}^2+{p_\mathrm{z}}^2\right. \\ &\quad \left.-\frac{2e|\mathbf{E}|}{\omega}\left(p_\mathrm{x}\sin\phi-p_\mathrm{y}\cos\phi\right)+\frac{e^2|\mathbf{E}|^2}{\omega^2}\right] \end{aligned} \tag{2-35}$$

Solving Eq. (2-29), the turning point t_0 is derived as

$$t_0 = \frac{p_\mathrm{x}\cos\phi+p_\mathrm{y}\sin\phi+\mathrm{i}\sqrt{2m_\mathrm{e}I_\mathrm{p}+\left(p_\mathrm{x}\sin\phi-p_\mathrm{y}\cos\phi-\dfrac{e|\mathbf{E}|}{\omega}\right)^2+{p_\mathrm{z}}^2}}{e|\mathbf{E}|}. \tag{2-36}$$

Substituting Eqs. (2-32) and (2-35) into Eq. (2-31), the action is obtained as

$$\begin{aligned} S &= \int_0^{t_0}\left(\frac{1}{2m_\mathrm{e}}\left[e^2|\mathbf{E}|^2t^2-2e|\mathbf{E}|\left(p_\mathrm{x}\cos\phi+p_\mathrm{y}\sin\phi\right)t+{p_\mathrm{x}}^2+{p_\mathrm{y}}^2+{p_\mathrm{z}}^2-\frac{2e|\mathbf{E}|}{\omega}\left(p_\mathrm{x}\sin\phi-p_\mathrm{y}\cos\phi\right)\right.\right. \\ &\quad \left.\left.+\frac{e^2|\mathbf{E}|^2}{\omega^2}\right]+I_p\right)\mathrm{d}t \\ &= \frac{1}{2m_\mathrm{e}}\left[\frac{e^2|\mathbf{E}|^2}{3}t^3-e|\mathbf{E}|\left(p_\mathrm{x}\cos\phi+p_\mathrm{y}\sin\phi\right)t^2+\left[{p_\mathrm{x}}^2+{p_\mathrm{y}}^2+{p_\mathrm{z}}^2-\frac{2e|\mathbf{E}|}{\omega}\left(p_\mathrm{x}\sin\phi-p_\mathrm{y}\cos\phi\right)\right.\right. \\ &\quad \left.\left.+\frac{e^2|\mathbf{E}|^2}{\omega^2}+2m_\mathrm{e}I_\mathrm{p}\right]t\right]_0^{t_0} \end{aligned}$$

$$\begin{aligned} \mathrm{Im}S &= \frac{1}{2m_\mathrm{e}}\left\{\frac{e^2|\mathbf{E}|^2}{3}\left[3(\mathrm{Re}\,t_0)^2-(\mathrm{Im}t_0)^3\right]-e|\mathbf{E}|\left(p_\mathrm{x}\cos\phi+p_\mathrm{y}\sin\phi\right)2\,\mathrm{Re}\,t_0\,\mathrm{Im}t_0\right. \\ &\quad \left.+\left[{p_\mathrm{x}}^2+{p_\mathrm{y}}^2+{p_\mathrm{z}}^2-\frac{2e|\mathbf{E}|}{\omega}\left(p_\mathrm{x}\sin\phi-p_\mathrm{y}\cos\phi\right)+\frac{e^2|\mathbf{E}|^2}{\omega^2}+2m_\mathrm{e}I_\mathrm{p}\right]\mathrm{Im}t_0\right\} \end{aligned}$$

$$\mathrm{Im}\,S = \frac{1}{3m_\mathrm{e}e|\mathbf{E}|}\left[2m_\mathrm{e}I_\mathrm{p} + \left(p_\mathrm{x}\sin\phi - p_\mathrm{y}\cos\phi - \frac{e|\mathbf{E}|}{\omega}\right)^2 + {p_\mathrm{z}}^2\right]^{\frac{3}{2}}. \tag{2-37}$$

When the classical momentum $m_\mathrm{e}\dot{\mathbf{x}}$ is separated into the components parallel ($p_{/\!/}$) and perpendicular ($p_\perp$) to $\mathbf{E}(0)$,

$$\begin{aligned}\mathrm{Im}\,S &= \frac{1}{3m_\mathrm{e}e|\mathbf{E}|}\left\{2m_\mathrm{e}I_\mathrm{p} + \left[\mathbf{p}\cdot(\hat{\mathbf{x}}\sin\phi - \hat{\mathbf{y}}\cos\phi) - \frac{e|\mathbf{E}|}{\omega}\right]^2 + {p_\mathrm{z}}^2\right\}^{\frac{3}{2}} \\ &= \frac{1}{3m_\mathrm{e}e|\mathbf{E}|}\left(2m_\mathrm{e}I_\mathrm{p} + \left\{[m_\mathrm{e}\dot{\mathbf{x}}(0) - e\mathbf{A}(0)]\cdot(\hat{\mathbf{x}}\sin\phi - \hat{\mathbf{y}}\cos\phi) - \frac{e|\mathbf{E}|}{\omega}\right\}^2 + {p_\mathrm{z}}^2\right)^{\frac{3}{2}} \\ &= \frac{1}{3m_\mathrm{e}e|\mathbf{E}|}\left\{2m_\mathrm{e}I_\mathrm{p} + [m_\mathrm{e}\dot{\mathbf{x}}(0)\cdot(\hat{\mathbf{x}}\sin\phi - \hat{\mathbf{y}}\cos\phi)]^2 + {p_\mathrm{z}}^2\right\}^{\frac{3}{2}}\end{aligned}$$

$$\mathrm{Im}\,S = \frac{1}{3m_\mathrm{e}e|\mathbf{E}|}\left(2m_\mathrm{e}I_\mathrm{p} + {p_\perp}^2\right)^{\frac{3}{2}} \tag{2-38}$$

is obtained. From Eq. (2-30),

$$w(p_\perp) = \exp\left(-\frac{2}{3}\frac{\left(2m_\mathrm{e}I_\mathrm{p} + {p_\perp}^2\right)^{\frac{3}{2}}}{\hbar m_\mathrm{e}e|\mathbf{E}|}\right) \approx \exp\left(-\frac{2\sqrt{8m_\mathrm{e}{I_\mathrm{p}}^3}}{3\hbar e|\mathbf{E}|}\right)\exp\left(-\frac{1}{\hbar e|\mathbf{E}|}\sqrt{\frac{2I_\mathrm{p}}{m_\mathrm{e}}}{p_\perp}^2\right) \tag{2-39}$$

is derived. The first factor is the same with the exponential factor of Eq.(2-27) and the second factor is the initial transverse momentum distribution.

2-2. Simple man's model

2-2-1. Arbitral laser fields

In simple man's model [10,34], the motion of a photoelectron after the tunneling can be obtained by solving Newton's equation of motion in a laser electric field as

$$\frac{\mathrm{d}\mathbf{p}_\mathrm{elec}(t)}{\mathrm{d}t} = -e\mathbf{E}(t), \tag{2-40}$$

where $\mathbf{p}_\mathrm{elec}(t)$ is a momentum of a photoelectron

$$\mathbf{p}_\mathrm{elec}(t) = m_\mathrm{e}\frac{\mathrm{d}\mathbf{r}(t)}{\mathrm{d}t}. \tag{2-41}$$

In this model, the initial condition at the moment of the tunneling $t = t_0$ is set to be

$$\mathbf{r}(t_0) = 0, \tag{2-42}$$

$$\mathbf{p}_\mathrm{elec}(t_0) = 0. \tag{2-43}$$

Solving Eq. (2-40) under Eq. (2-43), the momentum is obtained as

$$\mathbf{p}_\mathrm{elec}(t) = e(\mathbf{A}(t) - \mathbf{A}(t_0)), \tag{2-44}$$

where $\mathbf{A}(t)$ is the laser vector potential

$$\mathbf{A}(t) = -\int_{-\infty}^{t} \mathbf{E}(t)\mathrm{d}t \,. \tag{2-45}$$

The time-average kinetic energy is derived as

$$\langle E_{\mathrm{elec}}(t)\rangle = \frac{1}{T}\int_0^T \frac{|\mathbf{p}_{\mathrm{elec}}(t)|^2}{2m_{\mathrm{e}}}\,\mathrm{d}t = \frac{e^2}{2m_{\mathrm{e}}}\left\{\frac{1}{T}\int_0^T |\mathbf{A}(t)|^2\,\mathrm{d}t + |\mathbf{A}(t_0)|^2\right\}. \tag{2-46}$$

The first term of Eq. (2-46) corresponds to the ponderomotive energy

$$U_{\mathrm{p}} = \frac{e^2}{2m_{\mathrm{e}}}\frac{1}{T}\int_0^T |\mathbf{A}(t)|^2\,\mathrm{d}t \,. \tag{2-47}$$

After the laser pulse disappears, the final momentum of Eq. (2-44) becomes

$$\mathbf{p}_{\mathrm{elec}} = \mathbf{p}_{\mathrm{elec}}(t \to \infty) = -e\mathbf{A}(t_0), \tag{2-48}$$

which is the second term of Eq. (2-44) called a drift momentum. The final kinetic energy becomes

$$E_{\mathrm{elec}} = \frac{e^2|\mathbf{A}(t_0)|^2}{2m_{\mathrm{e}}} \,. \tag{2-49}$$

Solving Eq.(2-41) under Eq. (2-42),

$$\mathbf{r}(t) = \frac{1}{m_{\mathrm{e}}}\int_{t_0}^{t} e(\mathbf{A}(t) - \mathbf{A}(t_0))\mathrm{d}t = \frac{e}{m_{\mathrm{e}}}\left[\int_{t_0}^{t} \mathbf{A}(t)\mathrm{d}t - (t - t_0)\mathbf{A}(t_0)\right]. \tag{2-50}$$

The time of recollision t_{n} at which $\mathbf{r}(t_n) = 0$ ($n = 1, 2, 3, \cdots$) is satisfied can be obtained by solving the equation

$$\int_{t_0}^{t_n} \mathbf{A}(t)\mathrm{d}t = (t_n - t_0)\mathbf{A}(t_0). \tag{2-51}$$

The returning time t_n represents the n-th time at which the photoelectron goes back to ion core. The kinetic energy of the retuning photoelectron at $t = t_n$ is obtained as

$$E_{\mathrm{elec}}(t_n) = \frac{e^2|\mathbf{A}(t_n) - \mathbf{A}(t_0)|^2}{2m_{\mathrm{e}}} \,. \tag{2-52}$$

2-2-2. Linearly polarized continuous laser field

When the linearly polarized laser electric field is written as

$$\mathbf{E}(t) = E_0\hat{\mathbf{x}}\cos(\omega t + \phi), \tag{2-53}$$

the intensity of the laser field is given by

$$I = \varepsilon_0 c_0 \left\langle |\mathbf{E}(t)|^2 \right\rangle = \varepsilon_0 c_0 \frac{1}{T}\int_0^T |E_0\hat{\mathbf{x}}\cos(\omega t + \phi)|^2\,\mathrm{d}t = \frac{1}{2}\varepsilon_0 c_0 {E_0}^2 \,, \tag{2-54}$$

the vector potential

$$\mathbf{A}(t) = -\frac{E_0}{\omega}\hat{\mathbf{x}}\sin(\omega t + \phi), \tag{2-55}$$

the momentum

$$\mathbf{p}_{\mathrm{elec}}(t) = -\frac{eE_0}{\omega}\hat{\mathbf{x}}[\sin(\omega t + \phi) - \sin(\omega t_0 + \phi)], \tag{2-56}$$

the ponderomotive energy

$$U_{\mathrm{p}} = \frac{e^2}{2m_{\mathrm{e}}} \frac{1}{T} \int_0^T \left| \frac{E_0}{\omega} \hat{\mathbf{x}} \sin(\omega t + \phi) \right|^2 \mathrm{d}t = \frac{e^2 {E_0}^2}{4m_{\mathrm{e}}\omega^2} = \frac{e^2}{8\pi^2 m_{\mathrm{e}} \varepsilon_0 {c_0}^3} \lambda^2 I \,, \tag{2-57}$$

and the final momentum

$$\mathbf{p}_{\mathrm{elec}} = \frac{eE_0}{\omega} \hat{\mathbf{x}} \sin(\omega t + \phi). \tag{2-58}$$

The final kinetic energy becomes

$$E_{\mathrm{elec}} = 2U_{\mathrm{p}} \sin^2(\omega t_0 + \phi), \tag{2-59}$$

suggesting that the maximum kinetic energy is $2U_{\mathrm{p}}$, when $\omega t_0 + \phi = \pm\pi/2$. Equation (2-50) becomes

$$\mathbf{r}(t) = \frac{eE_0}{m_{\mathrm{e}}\omega^2} \hat{\mathbf{x}} [\cos(\omega t + \phi) - \cos(\omega t_0 + \phi)] + \frac{eE_0}{m_{\mathrm{e}}\omega} (t - t_0) \hat{\mathbf{x}} \sin(\omega t_0 + \phi). \tag{2-60}$$

Here, the first term represents the oscillation with the amplitude called quiver radius

$$\alpha_0 = \frac{eE_0}{m_{\mathrm{e}}\omega^2}, \tag{2-61}$$

and the second term represents the translational motion by the drift momentum. Because of the oscillatory motion of the electron, recollision is possible in the specific range of t_0. The time of recollision t_{n} can be obtained by solving

$$[\cos(\omega t_n + \phi) - \cos(\omega t_0 + \phi)] + \omega(t_{\mathrm{n}} - t_0)\sin(\omega t_0 + \phi) = 0. \tag{2-62}$$

Therefore, the energy of the returning electron can be obtained as

$$E_{\mathrm{elec}}(t_n) = 2U_{\mathrm{p}}[\sin(\omega t_n + \phi) - \sin(\omega t_0 + \phi)]^2. \tag{2-63}$$

The maximum energy of Eq. (2-63) becomes $3.17U_{\mathrm{p}}$, by solving Eq. (2-50) numerically.

2-2-3. Elliptically polarized continuous laser field

When the elliptically polarized electric laser field with ellipticity ε ($-1 \le \varepsilon \le 1$) is written as

$$\mathbf{E}(t) = E_0 [\hat{\mathbf{x}} \cos(\omega t + \phi) + \hat{\mathbf{y}} \varepsilon \sin(\omega t + \phi)], \tag{2-64}$$

the intensity of the laser field can be derived as

$$I = \varepsilon_0 c_0 \left\langle |\mathbf{E}(t)|^2 \right\rangle = \frac{1 + \varepsilon^2}{2} \varepsilon_0 c_0 {E_0}^2, \tag{2-65}$$

and the vector potential becomes

$$\mathbf{A}(t) = -\frac{E_0}{\omega} [\hat{\mathbf{x}} \sin(\omega t + \phi) - \hat{\mathbf{y}} \varepsilon \cos(\omega t + \phi)]. \tag{2-66}$$

Because the inner product of two vectors $\mathbf{E}(t) \cdot \mathbf{A}(t)$ is proportional to $1-\varepsilon^2$, when the linearly polarized laser field is used, i.e., $\varepsilon = 0$, the two vectors are parallel to each other, while when the circularly polarized laser field is used, i.e., $\varepsilon = \pm 1$, the two vectors are perpendicular. The momentum is obtained as

$$\mathbf{p}_{\mathrm{elec}}(t) = -\frac{eE_0}{\omega} \{\hat{\mathbf{x}} [\sin(\omega t + \phi) - \sin(\omega t_0 + \phi)] - \hat{\mathbf{y}} \varepsilon [\cos(\omega t + \phi) - \cos(\omega t_0 + \phi)]\}, \tag{2-67}$$

and the ponderomotive energy becomes

$$U_{\mathrm{p}} = \frac{e^2 {E_0}^2}{4 m_{\mathrm{e}} \omega^2} \left(1+\varepsilon^2\right) = \frac{e^2}{8\pi^2 m_{\mathrm{e}} \varepsilon_0 {c_0}^3} \lambda^2 I \,. \tag{2-68}$$

Therefore, the relation between the ponderomotive energy U_{p} and the laser intensity I is independent on the ellipticity. The final momentum becomes

$$\mathbf{p}_{\mathrm{elec}} = \frac{eE_0}{\omega}\left[\hat{\mathbf{x}}\sin(\omega t_0+\phi) - \hat{\mathbf{y}}\varepsilon\cos(\omega t_0+\phi)\right], \tag{2-69}$$

and the final kinetic energy becomes

$$E_{\mathrm{elec}} = \frac{2}{1+\varepsilon^2} U_{\mathrm{p}} \left[\sin^2(\omega t_0+\phi) + \varepsilon^2 \cos^2(\omega t_0+\phi)\right]. \tag{2-70}$$

Therefore, when the circularly polarized laser field is used, the kinetic energy always becomes U_{p}. On the other hand, the position of the electron becomes

$$\begin{aligned}\mathbf{r}(t) = {} & \frac{eE_0}{m_{\mathrm{e}}\omega^2}\left\{\hat{\mathbf{x}}\left[\cos(\omega t+\phi)-\cos(\omega t_0+\phi)\right] + \hat{\mathbf{y}}\varepsilon\left[\sin(\omega t+\phi)-\sin(\omega t_0+\phi)\right]\right\} \\ & + \frac{eE_0}{m_{\mathrm{e}}\omega}(t-t_0)\left[\hat{\mathbf{x}}\sin(\omega t_0+\phi) - \hat{\mathbf{y}}\varepsilon\cos(\omega t_0+\phi)\right]\end{aligned}, \tag{2-71}$$

resulting that the probability of the recollision decreases as the ellipticity increases.

2-3. Tunnel-exit

The tunnel-exit r_0 is the distance between an electron and an ion core just after the tunneling, and can be derived as the turning point of an electron whose energy is $-I_{\mathrm{p}}$ in the Coulombic potential modified by the laser field. Adopting field-direction model, in which the electron is ejected along z axis, the equation is given by

$$-e|\mathbf{E}|r_0 - \frac{1}{4\pi\varepsilon_0}\frac{Ze^2}{r_0} = -I_{\mathrm{p}} \,. \tag{2-72}$$

Solving Eq. (2-72), the tunnel-exit can be obtained as

$$r_0 = \frac{I_{\mathrm{p}} + \sqrt{{I_{\mathrm{p}}}^2 - \dfrac{Ze^3}{\pi\varepsilon_0}|\mathbf{E}|}}{2e|\mathbf{E}|}, \tag{2-73}$$

under the condition

$$|\mathbf{E}| \le \frac{{I_{\mathrm{p}}}^2}{Ze^3/(\pi\varepsilon_0)}, \tag{2-74}$$

that is, the ionization process can be regarded as not over-the-barrier ionization but tunnel ionization.

However, in this field-direction model, the motion of an electron is restricted to one-dimensional coordinates. As shown in Sec. 2-1-1, the Schrödinger equation of an electron in the laser field and Coulombic field of an ion core is separable in the parabolic coordinates (Eq. (2-9)) [123,124]. From Eq. (2-13), the equation for the turning point is expressed as

$$-\frac{\hbar^2\beta_1}{2m_e\xi_0}+\frac{e|\mathbf{E}|}{8}\xi_0=-\frac{I_p}{4}. \tag{2-75}$$

In Eq. (2-75), the term including ξ^{-2} is neglected, because the electron is far enough from the origin. Solving Eq. (2-75), the outer turning point is obtained as

$$\xi_0=\frac{I_p+\sqrt{{I_p}^2-\frac{4\hbar^2e\beta_1}{m_e}|\mathbf{E}|}}{e|\mathbf{E}|}. \tag{2-76}$$

From Eq. (2-19), the tunnel-exit is derived as

$$\begin{aligned} r_0=\frac{\xi_0}{2}&=\frac{I_p+\sqrt{{I_p}^2-\frac{4\hbar^2e}{m_e}\left[\frac{n^*\kappa}{\hbar}-\frac{\kappa}{2\hbar}\left(|m|+1\right)\right]|\mathbf{E}|}}{2e|\mathbf{E}|}\\ &=\frac{I_p+\sqrt{{I_p}^2-\frac{4\hbar^2e}{m_e}\left[\frac{Zm_ee^2}{4\pi\varepsilon_0\hbar^2}-\frac{\sqrt{2m_eI_p}}{2\hbar}\left(|m|+1\right)\right]|\mathbf{E}|}}{2e|\mathbf{E}|}\\ r_0&=\frac{I_p+\sqrt{{I_p}^2-\left[\frac{Ze^3}{\pi\varepsilon_0}-2\hbar e\sqrt{\frac{2I_p}{m_e}}\left(|m|+1\right)\right]|\mathbf{E}|}}{2e|\mathbf{E}|}. \end{aligned} \tag{2-77}$$

Compared with the tunnel-exit derived by the field direction model (Eq. (2-77)), the tunnel-exit in the parabolic coordinate system becomes long.

3. Femtosecond and few-cycle laser pulses

3-1. Introduction

Development in intense ultrashort laser technologies [125] has played an important role in investigation of molecules in intense laser fields. Chirped-pulse amplification (CPA) [126] and Ti:Sapphire mode-locked laser [127] offer us to use intense femtosecond pulses whose peak intensity at the focal point can be above 10^{14} W/cm^2. Through the pulse compression by a rare-gas filled hollow-core fiber [72], femtosecond laser pulses with a few optical cycles within their pulse duration can be generated. Few-cycle pulses thus obtained have been applied to probe the ultrafast phenomena such as nuclear wavepacket motion of molecules by pump and probe experiments [128,129], and to investigate CEP dependent phenomena.

In both generation and application of femtosecond and few-cycle laser pulses, understanding of their characteristics owing to their broad bandwidth and high laser intensity is necessary. Particularly, the effect of group velocity dispersion is crucial in few-cycle laser pulses. In this short chapter, the effect of propagation of laser pulses in dispersive and nonlinear media, and generation method of femtosecond and few-cycle laser pulses are briefly summarized. Furthermore, the CEP effect in a circularly polarized few-cycle laser pulse is also described.

3-2. Propagation of femtosecond laser pulse

3-2-1. Spectral phase

The complex amplitude of the Gaussian laser pulse can be written as

$$\tilde{E}(\omega)=E_0\exp\left[-2(\ln 2)\left(\frac{\omega-\omega_0}{\Delta\omega}\right)^2+\mathrm{i}\phi(\omega)\right], \tag{3-1}$$

where ω_0 is a central frequency, $\Delta\omega$ is a spectral bandwidth (FWHM), and $\phi(\omega)$ is a spectral phase. When the spectral phase is expanded into Taylor series of ω as

$$\phi(\omega)=\sum_n\frac{1}{n!}\phi_n(\omega-\omega_0)^n=\phi_0+\phi_1(\omega-\omega_0)+\frac{1}{2}\phi_2(\omega-\omega_0)^2+\frac{1}{6}\phi_3(\omega-\omega_0)^3+\cdots, \tag{3-2}$$

the inverse Fourier transformation of Eq. (3-1) is given by

$$E(t)=\frac{1}{\sqrt{2\pi}}\int_{-\infty}^{\infty}E_0\exp\left[-2(\ln 2)\left(\frac{\omega-\omega_0}{\Delta\omega}\right)^2+\mathrm{i}\sum_n\frac{1}{n!}\phi_n(\omega-\omega_0)^n-\mathrm{i}\omega t\right]\mathrm{d}\omega$$

$$=\frac{1}{\sqrt{2\pi}}\exp(-\mathrm{i}\omega_0 t)\int_{-\infty}^{\infty}E_0\exp\left[-2(\ln 2)\left(\frac{\omega-\omega_0}{\Delta\omega}\right)^2+\mathrm{i}\sum_n\frac{1}{n!}\phi_n(\omega-\omega_0)^n-\mathrm{i}(\omega-\omega_0)t\right]\mathrm{d}\omega$$

By rewriting ω-ω_0 as ω, the electric field becomes

$$E(t)=\frac{E_0}{\sqrt{2\pi}}\exp(-\mathrm{i}\omega_0 t+\mathrm{i}\phi_0)\int_{-\infty}^{\infty}\exp\left[\left(-\frac{2\ln 2}{\Delta\omega^2}+\frac{1}{2}\mathrm{i}\phi_2\right)\omega^2-\mathrm{i}\omega(t-\phi_1)+\mathrm{i}\sum_{n=3}\frac{1}{n!}\phi_n\omega^n\right]\mathrm{d}\omega\,. \tag{3-3}$$

Assuming $\phi_n = 0$ ($n > 2$),

$$E(t)=\frac{E_0}{\sqrt{2\pi}}\exp(-\mathrm{i}\omega_0 t+\mathrm{i}\phi_0)\int_{-\infty}^{\infty}\exp\left[\left(-\frac{2\ln 2}{\Delta\omega^2}+\frac{\mathrm{i}\phi_2}{2}\right)\left(\omega^2-\frac{\mathrm{i}(t-\phi_1)\omega}{-\frac{2\ln 2}{\Delta\omega^2}+\frac{\mathrm{i}\phi_2}{2}}\right)\right]\mathrm{d}\omega$$

$$E(t)=\frac{E_0}{\left[\left(\frac{4\ln 2}{\Delta\omega^2}\right)^2+{\phi_2}^2\right]^{\frac{1}{4}}}\exp\left\{-2(\ln 2)\frac{(t-\phi_1)^2}{\Delta\omega^2\left[\left(\frac{4\ln 2}{\Delta\omega^2}\right)^2+{\phi_2}^2\right]}\right. \tag{3-4}$$

$$\left.-\mathrm{i}\left(\omega_0+\frac{1}{2}\phi_2\frac{t-\phi_1}{\left(\frac{4\ln 2}{\Delta\omega^2}\right)^2+{\phi_2}^2}\right)(t-\phi_1)+\mathrm{i}\left[\phi_0-\omega_0\phi_1+\arctan\left(\frac{\phi_2\Delta\omega^2}{8\ln 2}\right)\right]\right\}$$

Therefore, the zeroth-order term ϕ_0 represents the CEP

$$\phi_0-\omega_0\phi_1+\arg\left(\frac{\phi_2\Delta\omega^2}{8\ln 2}\right). \tag{3-5}$$

The first-order term ϕ_1 represents a time delay of the laser pulse called group delay. The second-order term ϕ_2 represents the linear chirp of instantaneous frequency

$$\omega(t)=-\left(\omega_0+\frac{1}{2}\phi_2\frac{t+\phi_1}{\left(\frac{4\ln 2}{\Delta\omega^2}\right)^2+{\phi_2}^2}\right), \tag{3-6}$$

and, the pulse duration is elongated as

$$\Delta t=\Delta\omega\sqrt{\left(\frac{4\ln 2}{\Delta\omega^2}\right)^2+{\phi_2}^2}\,, \tag{3-7}$$

comparing with that at $\phi_2 = 0$. In general, the product of Δt and $\Delta\omega$ is more than a certain value which is obtained for the Fourier-transform limited pulse i.e., when $\phi_n = 0$ ($n > 1$). For example, the relation of $\Delta t\Delta\omega \geq 4\ln 2$ is satisfied for a Gaussian laser pulse.

3-2-2. Propagation of laser pulse

When the complex amplitude of a Fourier-transform limited Gaussian laser pulse at $z = 0$ in vacuum can be written as

$$E(0,t) = E_0 \exp\left[-2(\ln 2)\left(\frac{t}{\Delta t}\right)^2 - \mathrm{i}\omega_0 t + \mathrm{i}\phi_{\mathrm{abs}} \right], \tag{3-8}$$

its Fourier transform is derived as

$$\tilde{E}(0,\omega) = E_0 \exp\left[-\frac{\Delta t^2}{8\ln 2}(\omega - \omega_0)^2 + \mathrm{i}\phi_{\mathrm{abs}} \right]. \tag{3-9}$$

After the laser pulse is propagated through a dispersed medium (length: L) whose refractive index exhibits the wavelength dependence $n_0(\lambda)$, the electric field becomes

$$\tilde{E}(L,\omega) = E_0 \exp\left\{ -\frac{\Delta t^2}{8\ln 2}(\omega - \omega_0)^2 + \mathrm{i}[k(\omega)L + \phi_{\mathrm{abs}}] \right\}, \tag{3-10}$$

where $k(\omega)$ is the wavenumber as

$$k(\omega) = k_0(\omega) = \frac{2\pi n_0(\lambda)}{\lambda}. \tag{3-11}$$

Therefore, the group delay per unit length is given by

$$k_1(\omega) = \frac{\mathrm{d}k}{\mathrm{d}\omega} = \frac{\mathrm{d}}{\mathrm{d}\omega}\frac{2\pi n_0(\lambda)}{\lambda} = \frac{1}{c_0}\left(n_0(\lambda) - \lambda\frac{\mathrm{d}n_0(\lambda)}{d\lambda} \right), \tag{3-12}$$

Here, k_1^{-1} is called group velocity. The second-order term k_2 is called group velocity dispersion (GVD) and is expressed as

$$k_2(\omega) = \frac{\mathrm{d}^2 k}{\mathrm{d}\omega^2} = \frac{\mathrm{d}}{\mathrm{d}\omega}\frac{1}{c_0}\left[n_0(\lambda) - \lambda\frac{\mathrm{d}n_0(\lambda)}{d\lambda} \right] = \frac{\lambda^3}{2\pi {c_0}^2}\frac{\mathrm{d}^2 n_0(\lambda)}{\mathrm{d}\lambda^2}. \tag{3-13}$$

Therefore, when the laser pulse propagates through the dispersed media, the complex amplitude becomes

$$E(L,t) = \frac{E_0}{\left[\left(\frac{\Delta t^2}{4\ln 2} \right)^2 + (k_2 L)^2 \right]^{\frac{1}{4}}} \exp\left\{ -2\ln 2 \frac{(t - k_1 L)^2}{\left[\Delta t^2 + \left(\frac{4\ln 2 k_2 L}{\Delta t} \right)^2 \right]} \right.$$
$$\left. - \mathrm{i}\left(\omega_0 + \frac{1}{2}k_2 L \frac{t - k_1 L}{\left(\frac{\Delta t^2}{4\ln 2} \right)^2 + (k_2 L)^2} \right)(t - k_1 L) + \mathrm{i}\left[\phi_{\mathrm{abs}} + (k_0 - \omega_0 k_1)L + \arctan\left(\frac{2\ln 2}{\Delta t^2} k_2 L \right) \right] \right\}$$
. (3-14)

Figure 3-1(a) shows the wavelength dependence of the refractive index of fused silica and air. The Sellmeier formulae are

$${n_0}^2 = 1 + \frac{0.6961663(\lambda/\mu\mathrm{m})^2}{(\lambda/\mu\mathrm{m})^2 - 0.0684043^2} + \frac{0.4079426(\lambda/\mu\mathrm{m})^2}{(\lambda/\mu\mathrm{m})^2 - 0.1162414^2} + \frac{0.8974794(\lambda/\mu\mathrm{m})^2}{(\lambda/\mu\mathrm{m})^2 - 9.896161^2} \tag{3-15}$$
$$(0.23\,\mu\mathrm{m} < \lambda < 3.5\,\mu\mathrm{m})$$

for fused silica, and

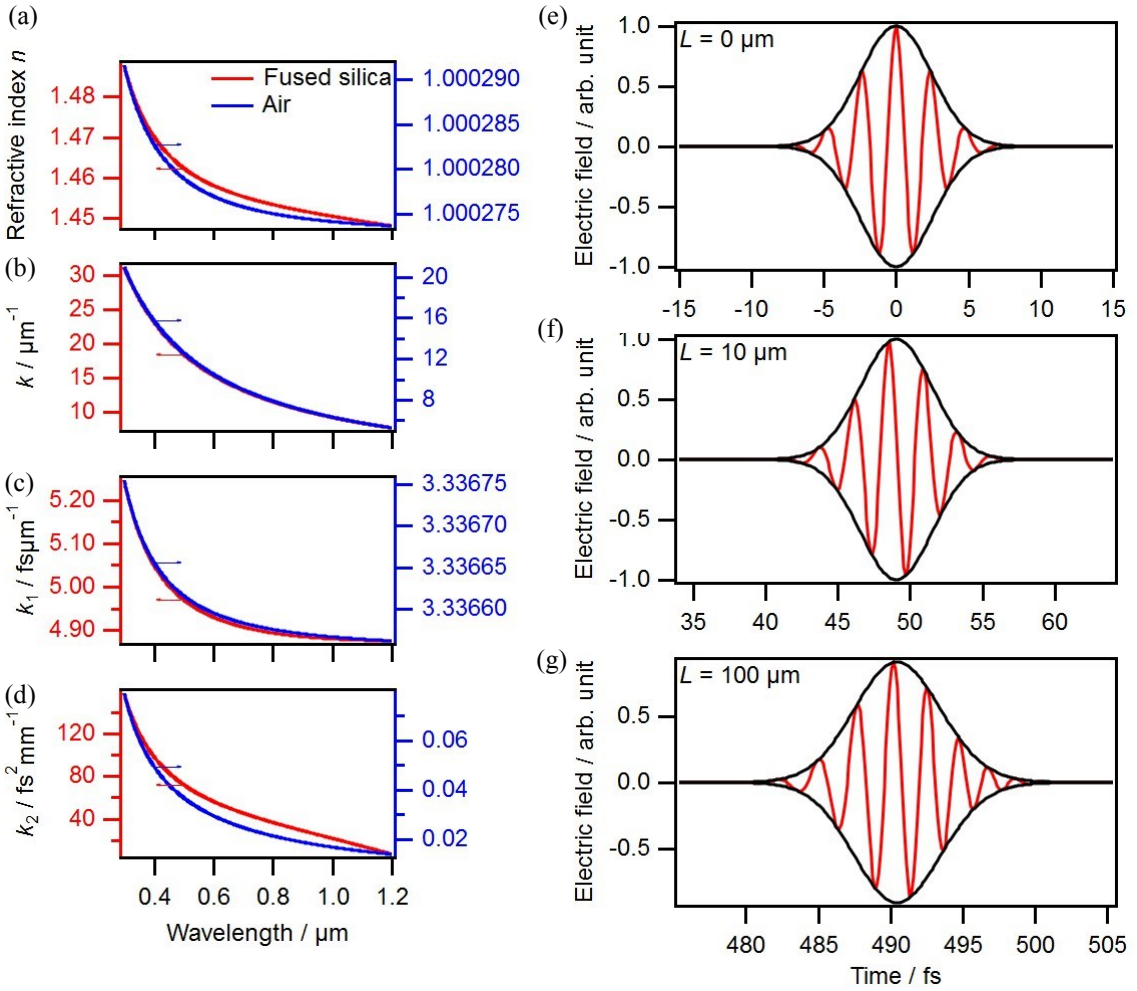

Fig.3-1 (a) Refractive index of fused silica (red line, left axis) and air (blue line, right axis). (b) Wavenumber obtained from (a). (c) The first derivative of (b). (d) The second derivative of (b). (e), (f) and (g) The waveform of the few-cycle laser pulse (722 nm, 4.1 fs), after the propagation in fused silica of L = 0, 10, and 100 μm, respectively.

$$n_0=1+\left(\frac{5791817}{238.0185-\left(\frac{1}{\lambda/\mu\mathrm{m}}\right)^2}+\frac{167909}{57.362-\left(\frac{1}{\lambda/\mu\mathrm{m}}\right)^2}\right)\times10^{-8},\ (0.23\,\mu\mathrm{m}<\lambda<1.7\,\mu\mathrm{m}) \quad (3\text{-}16)$$

for air [130].

The calculated wavenumbers k, their derivatives k_1 and k_2 are shown in Figs. 3-1(b), 3-1(c) and 3-1(d), respectively. In the case of fused silica, the propagation of a few-cycle laser pulse (722 nm, 4.1 fs, Fig. 3-1(e)) is simulated by Fourier transformation of Eq. (3-10). After the propagation of L = 10 μm, the CEP is changed by $(k_0-\omega_0 k_1)L$ = -1.34 rad, which corresponds to the difference of the phase velocity and the group velocity, as shown in Fig. 3-1(f). In the case of air, the CEP is shifted by $-\pi/2$ by the propagation about 30 mm. Furthermore, after the propagation of L = 100 μm in fused silica, the pulse duration

is elongated to 5.0 fs as shown in Fig. 3-1(g). As above, the CEP and the pulse duration can be controlled by changing the length of the dispersed media.

3-2-3. Self-phase modulation

Spectral phase modulation (SPM) is the third-order nonlinear process. The refractive index depends on the laser intensity as

$$n = n_0 + n_2 I, \tag{3-17}$$

where n_2 is a nonlinear refractive index. When only the second-term is taken into account, after propagation of L, the electric field Eq. (3-8) becomes

$$E(L,t) = E_0 \exp\left[-2(\ln 2)\left(\frac{t}{\Delta t}\right)^2 - \mathrm{i}\omega_0 t + \mathrm{i}n_2 I(0,t)k_0 L + \mathrm{i}\phi_{\mathrm{abs}}\right]. \tag{3-18}$$

where $n_0 = 1$. Because the laser intensity is expressed as

$$I(0,t) = \frac{1}{2}\varepsilon_0 c_0 {E_0}^2 \exp\left[-4(\ln 2)\left(\frac{t}{\Delta t}\right)^2\right], \tag{3-19}$$

the instantaneous frequency can be derived as

$$\omega(z,t) = \omega_0\left\{1 + 4(\ln 2)n_2\varepsilon_0 {E_0}^2 L\frac{t}{{\Delta t}^2}\exp\left[-4(\ln 2)\left(\frac{t}{\Delta t}\right)^2\right]\right\}. \tag{3-20}$$

Therefore, the laser pulse becomes up-chirped. However the pulse duration is not changed as indicated by Eq. (3-18). Because the laser pulse Eq. (3-18) is not the Fourier-transform limited pulse, the spectral bandwidth is considered to be broadened. Actually, the SPM and the dispersion effect described in Sec. 3-2-2 occur simultaneously. The simulation of the propagation of an intense femtosecond laser pulse including SPM needs to be performed step-by-step, because the SPM changes the spectrum according to the temporal profile of the laser intensity, which is modified by the GVD [131].

3-3. Generation of femtosecond and few-cycle laser pulse

3-3-1. Ti: Sapphire chirped pulse amplification laser system

Ti:Sapphire is a crystal in which a few percent of Al^{3+} in Al_2O_3 are replaced by Ti^{3+}. Because the ion diameter of Ti^{3+} is 26% larger than that of Al^{3+}, the crystal structure is distorted. Therefore, the degenerated electronic states are split and the broad emission spectrum ($^2T_g \rightarrow {}^2E_g$) is obtained when the 400 ~ 600 nm light is absorbed. This broad

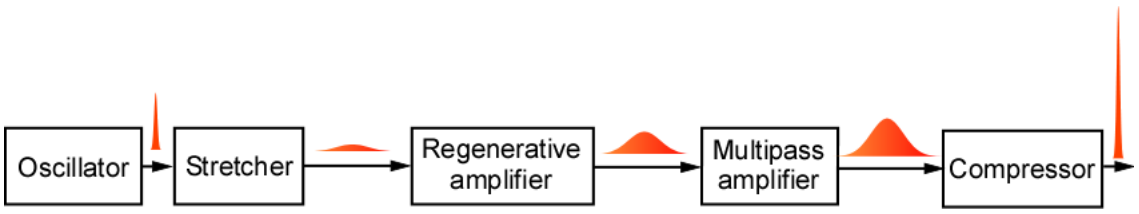

Fig.3-2 Flow chart of CPA system.

emission spectrum enabled us to generate a femtosecond laser pulse [132]. In an oscillator, a Ti:Sapphire crystal is irradiated with the pump laser in an optical cavity, resulting that continues-wave (CW) near-infrared laser is generated. By introducing the modulation of the cavity length, femtosecond laser pulses are generated via Kerr lens mode-locking [127].

When a femtosecond laser pulse is amplified, its peak power can easily exceed the damage threshold of the crystal. In order to obtain high pulse energy, chirped pulse amplification (CPA) technique is widely used [126]. Fig. 3-2 shows the flow chart of the CPA system. A femtosecond laser pulse generated by an oscillator is introduced into a stretcher, in which the laser pulse is chirped by a pair of gratings and its pulse duration is elongated to picosecond order. Because the peak power decreases, the pulse energy of the chirped picosecond laser pulse can be amplified. The chirped laser pulse is amplified by a regenerative amplifier, which is pumped by an intense green nanosecond laser pulse such as second harmonics of Nd:YAG laser. The timing of the injection of the seed pulse from the stretcher to the cavity and that of the extraction of the amplified pulse from the cavity are controlled by a Pockels cell, which can change the polarization of the injected laser pulse by applying a high voltage through electro-optic effect. After the Ti:Sapphire crystal is irradiated with the green pump pulse, the seed pulse is injected and passes the crystal many times. Just before the population inversion in the crystal disappears, the amplified pulse is extracted. In order to obtain more high pulse energy, multipass amplifiers are used, in addition to the regenerative amplifier. After the amplification, the chirped laser pulse is introduced into a compressor, in which the dispersion is compensated by a pair of gratings. Thus, the intense femtosecond laser pulse can be obtained by the CPA system.

3-3-2. Generation of few-cycle pulses

In order to obtain the few-cycle pulse, (i) a broad spectral bandwidth, and (ii) spectral phase compensation is necessary. Figure 3-3 illustrates a flow chart of generating few-cycle laser pulse. The broadening of the laser spectrum is achieved by focusing the femtosecond laser pulse generated by the CPA, into a hollow-core fiber filled with rare gases [72,133]. In the hollow-core fiber, SPM is induced, resulting in broadening of the laser spectrum.

Because of the SPM, the second-order dispersion of the laser pulse increases. In order

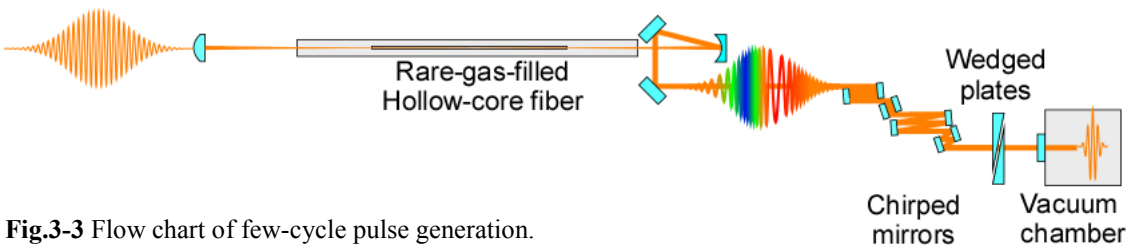

Fig.3-3 Flow chart of few-cycle pulse generation.

to compensate the positive dispersion, the laser pulses are reflected by the chirped mirrors. In Fig. 3-3, the configuration of double-angle multilayer chirped mirrors [134] is shown. The number of the chirped mirrors is set so that the second-order dispersion of the laser pulse becomes negative enough to compensate not only the dispersion induced by SPM in the hollow-core fiber, but also the dispersion gained through the propagation of the laser pulse in air and transmitted optics such as an entrance window of a vacuum chamber. A pair of glass wedged-plates are used to compensate the dispersion precisely by adjusting the optical pass length through the glass, and a few-cycle pulse can be obtained.

3-4. Circularly polarized few-cycle pulses

When the electric field of a right-handed circularly polarized laser pulse is written as

$$\mathbf{E}(t) = E_0 \exp\left[-2(\ln 2)\left(\frac{t}{\Delta t}\right)^2\right]\left[\hat{\mathbf{x}}\cos(\omega t + \phi_{\text{abs}}) - \hat{\mathbf{y}}\sin(\omega t + \phi_{\text{abs}})\right], \tag{3-21}$$

the CEP represents the direction of the laser electric field at the moment of $t = 0$. Figures 3-4(a) and 3-4(b) show the laser electric fields in stereographic drawing at $\phi_{\text{abs}} = 0$ and 90°, respectively. The black lines are the projections on t-E_x, t-E_y and E_x-E_y planes. The projections on E_x-E_y plane, i.e., the polarization plane, are also shown in Figs. 3-4(c) and 3-4(d) at $\phi_{\text{abs}} = 0$ and 90°, respectively. The direction of the electric field at $t = 0$ points to 0° at $\phi_{\text{abs}} = 0$° and to -90° at $\phi_{\text{abs}} = 90$°.

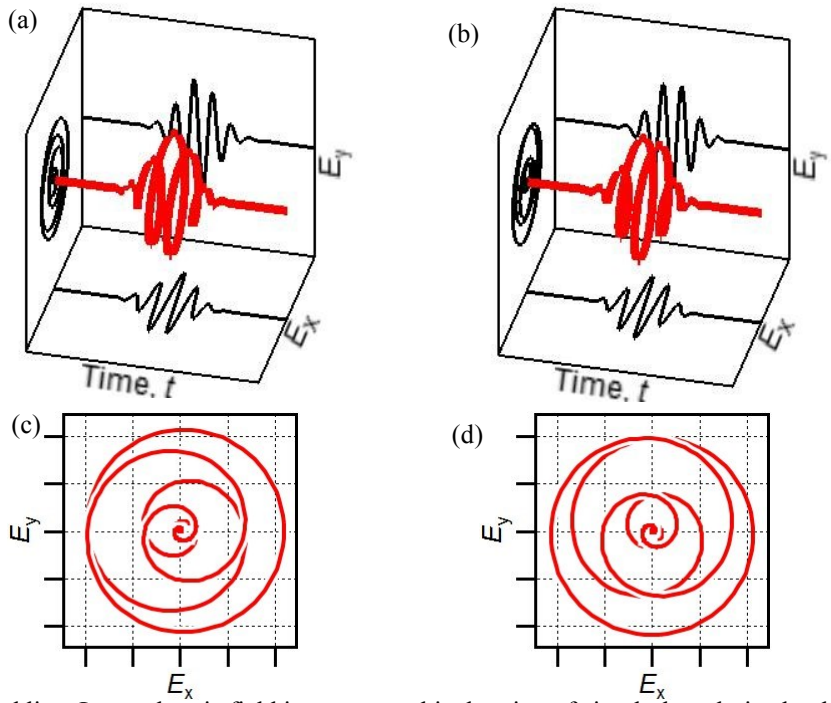

Fig.3-4 (a) Red line: Laser electric field in stereographic drawing of circularly polarized pulse whose pulse duration is 4.1 fs at $\phi_{\text{abs}} = 0$°. Black lines: Projection of laser electric field on E_x-E_y, t-E_x and t-E_y planes. (b) The same as (a) but at $\phi_{\text{abs}} = 90$°. (c) Projection of (a) on E_x-E_y plane. (d) Projection of (b) on E_x-E_y plane.

4. Determination of absolute CEP by circularly-polarized few-cycle pulses

本章については、5 年以内に雑誌等で刊行予定のため、非公開。

5. Photoelectron-photoion coincidence momentum imaging for dissociative ionization of methanol in intense UV laser fields

5-1. Introduction

In order to understand dissociative ionization of molecules in intense laser fields, photoelectron-photoion coincidence momentum imaging (PEPICO-MI) is a powerful tool as shown in following chapters. Several setups are known to record the momentum vectors of a photoelectron and a photoion in coincidence [163-167]. For example, in cold-target recoil ion momentum spectrometer (COLTRIMS) [164], a cold supersonic molecular beam is used as a sample and static electric and magnetic fields are used to detect photoelectrons and photoions ejected in 4π solid angle.

In the study of dissociative ionization of methanol described in the following chapters, three-dimensional (3D) momentum focusing condition by a static electric field is used for both photoelectrons and photoions [163]. The momentum component along the time-of-flight (TOF) axis is mapped to the TOF, irrespective to the distribution of ionization points along the TOF axis by Wiley-McLaren condition [168]. The momentum components perpendicular to the TOF axis are mapped to the position on the detector, irrespective to the distribution of ionization points, by velocity map imaging (VMI) condition [169]. The 3D momentum vectors of a photoelectron and a photoion are thus obtained. It should be noted that the 3D momentum distribution can be reconstructed by Abel inversion [170] from a two-dimensional (2D) momentum image projected on the detector, assuming cylindrical symmetry. However, the vector correlation between a photoelectron and a photoion cannot be revealed by Abel inversion. Consequently, the 3D momentum focusing is useful to investigate angular correlation in dissociative ionization of molecules.

In this chapter, the PEPICO-MI experimental setup and the analysis procedure, which are used in following chapters, are described.

5-2. Experimental setup

Near-infrared (NIR) femtosecond laser pulses are generated by a Ti:Sapphire CPA laser system. Ultraviolet (UV) pulses were generated through second-harmonic generation (SHG) of the NIR pulses by using β-barium borate crystal (BBO, 0.2 mm thick, type I). The UV pulse and the NIR pulse were separated by multi-layered mirrors which

reflect only 400 nm laser pulses. The waveform of the UV pulse was measured by self-diffraction frequency-resolved optical gating (SD-FROG) [171,172]. After attenuation of the pulse energy by adjusting the orifice diameter of an iris, the UV pulses were focused by an off-axis parabolic Al mirror (f = 200 mm, Janos Technology, LLC.) on an effusive molecular beam of methanol vapor in an ultra-high vacuum chamber whose base pressure is $\sim 1\times10^{-8}$ Pa shown in Fig. 5-1. The methanol sample was kept in a SUS tube (3/8 inchϕ). In order to decrease its impurity, the methanol sample was frozen by liquid nitrogen and contained impurities were evacuated by a scroll pump, several times. Pure methanol vapor was introduced into the vacuum chamber through a variable leak valve and a micro-syringe. The effusive molecular beam of methanol from the syringe was skimmed by a skimmer and was crossed with the laser pulses. The laser intensity at the focal point was estimated from the ponderomotive shift of the peaks in the photoelectron spectra of Kr and/or Xe recorded in the separate experiments under the same laser conditions.

The detail of the PEPICO-MI apparatus was previously reported [118,165]. A photoelectron and a photoion which were ejected from the crossing point of the laser beam and the molecular beam were extracted to the opposite directions and were focused on respective position sensitive detectors (PSDs) by the electrostatic lenses which fulfill 3D momentum focusing condition [163,165]. The 3D momentum vector of the photoelectrons $\boldsymbol{p}_{\mathrm{elec}}$ and that of photoions $\boldsymbol{p}_{\mathrm{ion}}$ were calculated from their arrival times at the respective PSDs and their positions on the PSDs. The PSDs were micro-channel plates (MCPs) and delay-line anodes called Hexanodes (HEX80 [173], RoentDek Handels GmbH). Timing signals from the MCPs and the delay-line anodes were amplified and discriminated by constant-fraction discriminators (CFDs) (ATR-19, RoentDek Handels GmbH). The signals were recorded as digital data by two time-to-digital converters (TDCs) (TDC8HP, RoentDek Handels GmbH). The start signal of the TDCs was another signal from a photodiode located just downstream of an exit window of the vacuum chamber. The arrival times of

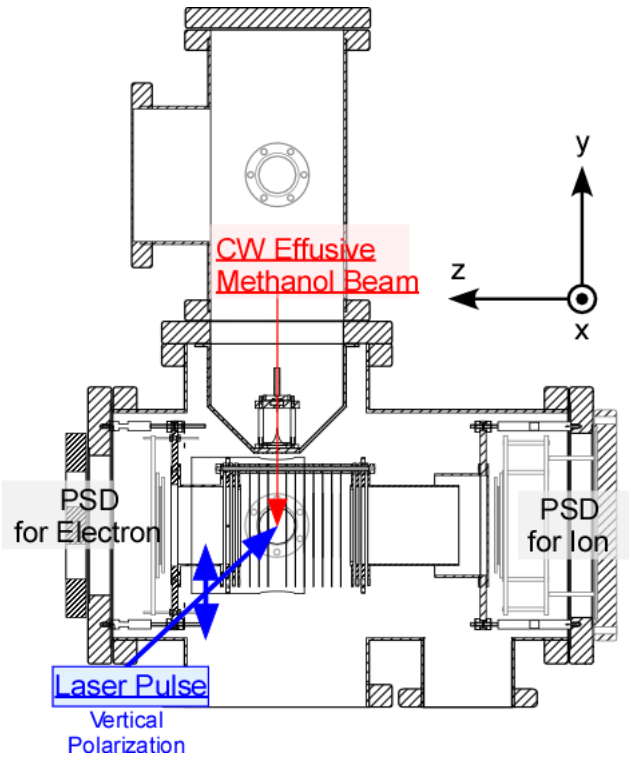

Fig.5-1 Schematic picture of the PEPICO vacuum chamber.

the signals were saved as the digital data whose binize is 25 ps in the list mode file by the software named CoboldPC 2002 (RoentDek Handels GmbH). Empty events, in which none of the signals from the two MCPs and the two HEX80s are detected, are not stored in the file. The arrival times of the photoelectron and the photoion at the detectors were obtained from the timing signals from the respective MCPs, and their positions on the detectors were converted from the signals from the respective delay-line anodes.

To ensure that the photoelectron and the photoion detected simultaneously were from an identical methanol molecule, the detection rate of the signals was kept around 0.3 events per laser pulse by controlling the amount of the methanol sample by the variable leak valve. The number of the signal from residual gas was reduced by a cryogenic effect, that is, the vacuum chamber was cooled by using liquid nitrogen. In the data analysis, only the events in which a single pair of a photoelectron and a photoion were detected were used.

5-3. Data analysis

5-3-1. Principle of delay-line anode

Using the delay-line anode type position-sensitive detector [174], the position where a photoelectron or a photoion is detected on the MCP is obtained from the difference of arrival times between two signals, one signal from one end of the delay-line and the other signal from the other end. However, the signal is propagated close to speed of light in the Cu delay-line. Therefore, it is necessary that the length of the delay-line is long enough to distinguish the difference of the arrival times.

Figure 5-2 shows a schematic picture of the detector [174], in which two layers of delay-lines are used. In the inner layer, a delay-line is wound onto the ceramic with a pitch such as 1 mm. The time in which the signal is propagated though one loop, that is, the signal is propagated for 1 mm perpendicular to the delay-line, is called the single pitch propagation time. In order that the difference of the arrival times between the two ends depends on the detected position perpendicular to the delay-line and is distinguishable, the single pitch propagation time is set to be a finite value.

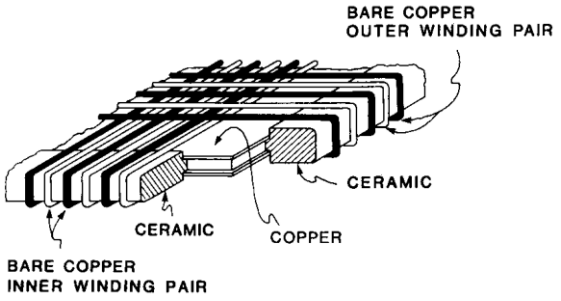

Fig.5-2 Schematic picture of delay-line anode type position-sensitive detector. [S. E. Sobottka, *et al.*, *IEEE Trans. Nucl. Sci.* **35**, 348 (1988). Fig. 1]

A pairwise delay-line is also wound onto the same ceramic with the same pitch. One delay-line is named as a signal delay-line and the other is named as a reference delay-line. The voltage of the signal delay-line is higher than that of the reference delay-line e.g.,, 36

V higher set by a battery box (BA3, RoentDek Handels GmbH). Therefore the electrons from a MCP are collected by the signal delay-line. The signals from the delay-lines are introduced into a differential amplifier and the signal from one layer is obtained as the difference signal between as a signal and reference delay-lines, ensuring that the signal originates from the MCP, because the noises which exhibits signals in both signal and reference delay-lines are suppressed by the differential amplifier.

In a similar manner, the outer layer of the delay-lines is wound perpendicular to the inner layer. The 2D position can be obtained by the signals from the two layers.

5-3-2. Principle of Hexanode

The Hexanode has the third layer, which is redundant to obtain the 2D position, and the three layers are crossed by 120°. In this thesis, the three axes, *u*, *v* and *w*, are defined as shown in Fig. 5-3. Therefore, there are three equations to obtain the position (*x*, *y*) and the multi-hit signals can be recorded without a dead time, in principle.

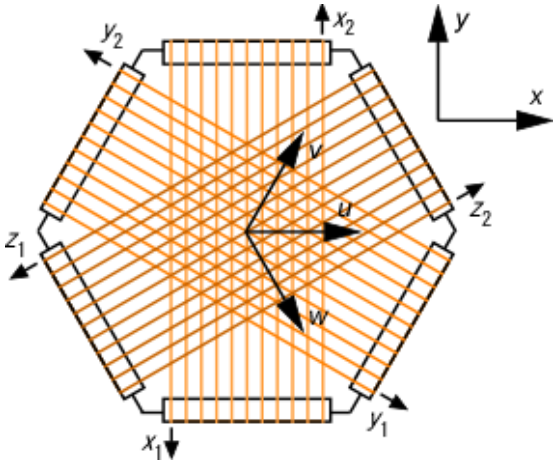

Fig.5-3 Schematic picture of Hexanode

The data recorded by TDC are six timing signals (x_1, x_2, y_1, y_2, z_1 and z_2) from the two ends of the three delay-lines. The positions (*u*, *v* and *w*) in the unit of the binsize of the TDC can be obtained as

$$\begin{cases} u = x_1 - x_2 \\ v = y_1 - y_2 \\ w = z_1 - z_2 + o_0 \end{cases}, \tag{5-1}$$

from the arrival time differences, where o_0 is a constant determined below. The 2D positions (*x*, *y*) are obtained from two of three positions (*u*, *v*, *w*) as

$$x_{\mathrm{uv}} = d_{\mathrm{u}} u, y_{\mathrm{uv}} = \frac{1}{\sqrt{3}}\left(-d_{\mathrm{u}} u + 2 d_{\mathrm{V}} v\right) \tag{5-2}$$

from (*u* ,*v*),

$$x_{\mathrm{vw}} = d_{\mathrm{v}} v + d_{\mathrm{w}} w, y_{\mathrm{vw}} = \frac{1}{\sqrt{3}}\left(d_{\mathrm{v}} v - d_{\mathrm{w}} w\right), \tag{5-3}$$

from (*v* ,*w*), and

$$x_{\mathrm{wu}} = d_{\mathrm{u}} u, y_{\mathrm{wu}} = \frac{1}{\sqrt{3}}\left(-2 d_{\mathrm{w}} w + d_{\mathrm{u}} u\right), \tag{5-4}$$

from (*w* ,*u*), where d_{i} (*i* = u, v and w) are the lengths per the unit time Δt, in the *u*, *v*, and *w* axes, respectively. The unit time in the case of TDC8HP is Δt = 25 ps. By using the perpendicular propagation speeds v_i of the signals, d_i are obtained as

$$d_i = \frac{1}{2} v_i \Delta t \,. \tag{5-5}$$

The perpendicular propagation speed is a reciprocal number of the single pitch propagation time. By taking averages of these three patterns (Eqs. (5-2), (5-3) and (5-4)), the 2D positions

$$x = d_u u + \frac{1}{3}\left(d_v v + d_w w - d_u u\right) = d_u\left(u + \frac{1}{3} o\right) \tag{5-6}$$

$$y = \frac{1}{\sqrt{3}}\left(d_v v - d_w w\right), \tag{5-7}$$

where

$$o = \frac{d_v}{d_u} v + \frac{d_w}{d_u} w - u \,, \tag{5-8}$$

are obtained. In order that Eqs. (5-2), (5-3) and (5-4) become the same, o_0 in Eq. (5-1) is adjusted so that o becomes 0.

It is noteworthy that after deriving x and y, the coordinate system is rotated about the z axis so that the new y axis becomes parallel to the laser polarization axis and the molecular axis beam (see Fig. 5-1).

5-3-3. Three-dimensional momentum vectors

At first, a photoelectron and a photoion ejected in 4π solid angle from the focal point are extracted to opposite direction by a constant electric field, similar to Wiley-McLaren type TOF mass spectrometer [168]. Then, they are focused by respective electrostatic

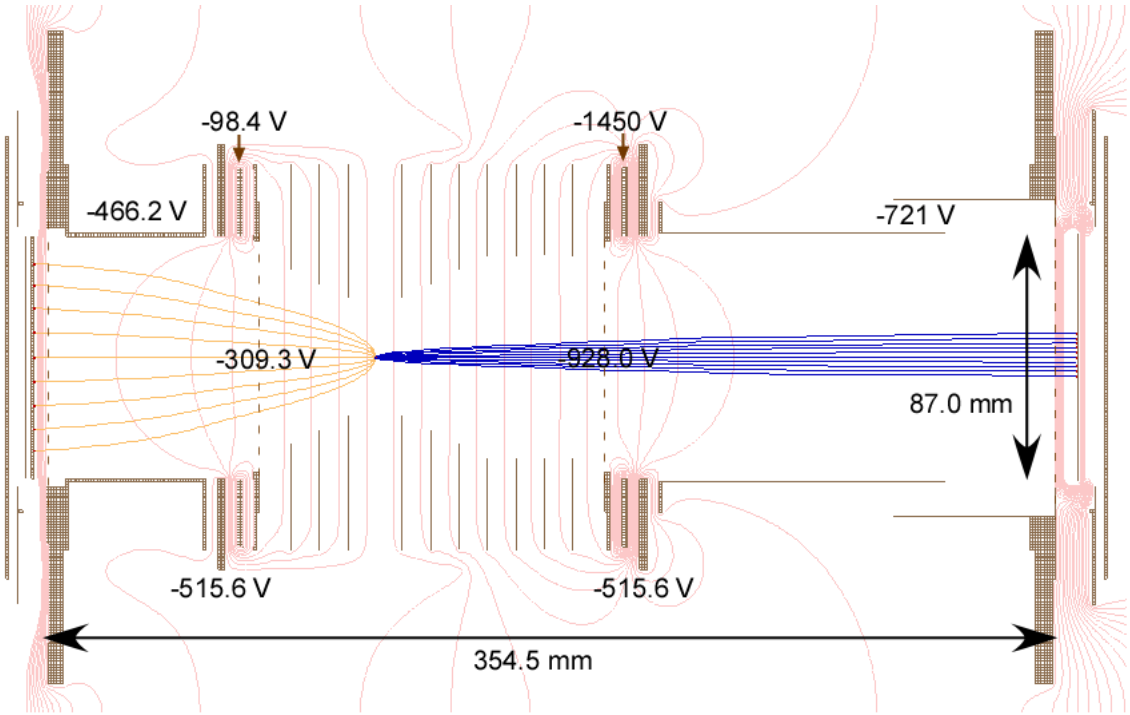

Fig.5-4 Brawn area or lines: Electrostatic lenses. Pink contour plots: Isopotential curve. Yellow and blue lines: Trajectories of electrons and ions, respectively, simulated by SIMION 8.0.

lenses on the respective PSDs, similarly to VMI [169]. Therefore, the 3D momentum vectors of both photoelectron and photoion and the mass to charge of the photoion are obtained from their flight times and positions on the PSDs, even if the ionization point is slightly deviated from the center point [163,165]. Particularly, the z components of the momentum vectors $p_{\mathrm{elec,z}}$, $p_{\mathrm{ion,z}}$ are derived from their flight times. The x components $p_{\mathrm{elec,x}}$, $p_{\mathrm{ion,x}}$ are derived from their positions x, and the y components $p_{\mathrm{elec,y}}$, $p_{\mathrm{ion,y}}$ are derived from their positions y.

When the kinetic energy is zero, the photoelectron or the photoion is detected at the time $t = t_0$ and the center position of the PSD $(x, y) = (x_0, y_0)$. The 3D momentum vector can be obtained as a function of the deviations as

$$\begin{cases} p_{\mathrm{elec,x}} = f_{\mathrm{elec,xy}}\left(x_{\mathrm{elec}} - x_{\mathrm{elec},0}\right) \\ p_{\mathrm{elec,y}} = f_{\mathrm{elec,xy}}\left(y_{\mathrm{elec}} - y_{\mathrm{elec},0}\right) \\ p_{\mathrm{elec,z}} = f_{\mathrm{elec,z}}\left(t_{\mathrm{elec}} - t_{\mathrm{elec},0}\right) \end{cases} \tag{5-9}$$

for a photoelectron and

$$\begin{cases} p_{\mathrm{ion,x}} = f_{\mathrm{ion,xy}}\left(x_{\mathrm{ion}} - x_{\mathrm{ion},0}\right)\sqrt{m_{\mathrm{ion}}} \\ p_{\mathrm{ion,y}} = f_{\mathrm{ion,xy}}\left[y_{\mathrm{ion}} - y_{\mathrm{ion},0}\left(m_{\mathrm{ion}}\right)\right]\sqrt{m_{\mathrm{ion}}} \\ p_{\mathrm{ion,z}} = f_{\mathrm{ion,z}}\left(\dfrac{t_{\mathrm{ion}} - t_{\mathrm{ion},0}\left(m_{\mathrm{ion}}\right)}{t_{\mathrm{ion},0}\left(m_{\mathrm{ion}}\right)}\right)\sqrt{m_{\mathrm{ion}}} \end{cases} \tag{5-10}$$

for a photoion.

In practice, the momentum vector is derived as

$$\begin{cases} p_{\mathrm{elec,x}} = a_{\mathrm{elec,xy}}\left(x_{\mathrm{elec}} - x_{\mathrm{elec},0}\right) \\ p_{\mathrm{elec,y}} = a_{\mathrm{elec,xy}}\left(y_{\mathrm{elec}} - y_{\mathrm{elec},0}\right) \\ p_{\mathrm{elec,z}} = a_{\mathrm{elec,z,1}}\left(t_{\mathrm{elec}} - t_{\mathrm{elec},0}\right) + a_{\mathrm{elec,z,2}}\left(t_{\mathrm{elec}} - t_{\mathrm{elec},0}\right)^2 \\ \qquad + a_{\mathrm{elec,z,3}}\left(t_{\mathrm{elec}} - t_{\mathrm{elec},0}\right)^3 + a_{\mathrm{elec,z,4}}\left(t_{\mathrm{elec}} - t_{\mathrm{elec},0}\right)^4 \end{cases} \tag{5-11}$$

for a photoelectron and

$$\begin{cases} p_{\mathrm{ion,x}} = a_{\mathrm{ion,xy}}\left(x_{\mathrm{ion}} - x_{\mathrm{ion},0}\right)\sqrt{m_{\mathrm{ion}}} \\ p_{\mathrm{ion,y}} = a_{\mathrm{ion,xy}}\left[y_{\mathrm{ion}} - y_{\mathrm{ion},0}\left(m_{\mathrm{ion}}\right)\right]\sqrt{m_{\mathrm{ion}}} \\ p_{\mathrm{ion,z}} = a_{\mathrm{ion,z}}\left(\dfrac{t_{\mathrm{ion}} - t_{\mathrm{ion},0}\left(m_{\mathrm{ion}}\right)}{t_{\mathrm{ion},0}\left(m_{\mathrm{ion}}\right)}\right)\sqrt{m_{\mathrm{ion}}} \end{cases} \tag{5-12}$$

for a photoion, where m_{ion} is its mass. The coefficients $a_{\mathrm{i,j}}$ (i = elec, ion, j = xy, z) are determined based on the simulation and their fits to the models Eqs. (5-11) and (5-12). In Chapters 6 and 8, following values are used as $a_{\mathrm{elec,xy}} = 0.027377$ au/mm, $a_{\mathrm{elec,z,1}} = -0.40013$ au/ns, $a_{\mathrm{elec,z,2}} = -0.096863$ au/ns^2, $a_{\mathrm{elec,z,3}} = -0.04859$ au/ns^3, $a_{\mathrm{elec,z,4}} = -0.0090339$ au/ns^4 for photoelectrons, and $a_{\mathrm{ion,xy}} = 0.0066609$ eV$^{1/2}$/mm, $a_{\mathrm{ion,z}} = 2089.4$

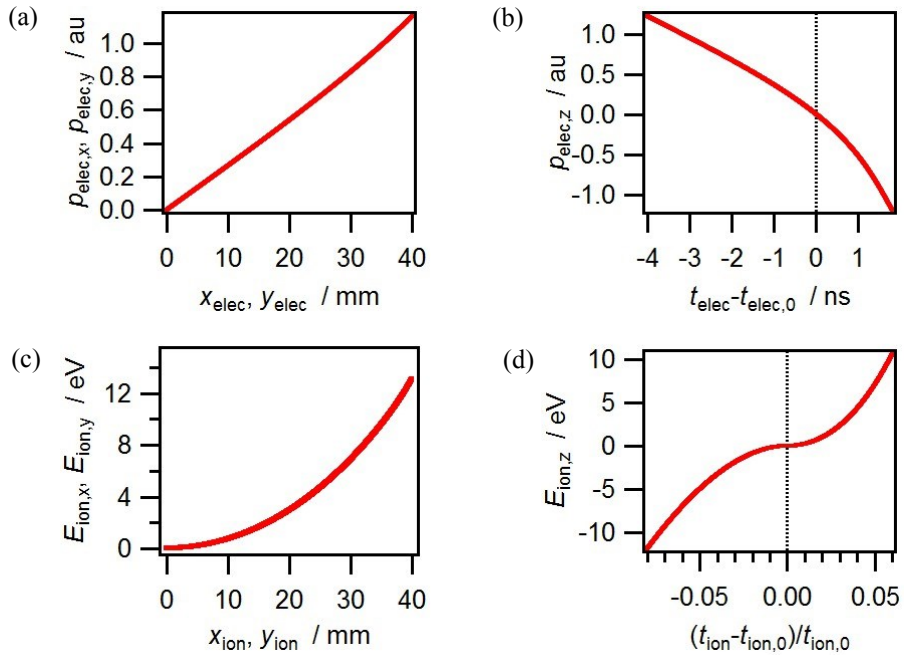

Fig.5-5 (a) Electron momentum as a function of the detected position. (b) Electron momentum as a function of the flight time. (c) Ion translational energy as a function of the detected position. (d) Ion translational energy as fuction of the relative flight time. The sign of energy is defined as the same as the corresponding momentum.

$eV^{1/2}$ when $t_{ion} > t_{ion,0}(m_{ion})$ and $a_{ion,z} = 2365.4$ $eV^{1/2}$ when $t_{ion} < t_{ion,0}(m_{ion})$ for photoions.

On the one hand, in Chapter 7, where the improved apparatus (see Appendix) is used, the simulated results by the software named SIMION 8.0 (Scientific Instrument Services, Inc.) are directly utilized. Figure 5-4 illustrates the configuration of the electrostatic lenses and the simulated trajectories of the photoelectrons and the photoions. Figures 5-5(a) and 5-5(b) show the functions for photoelectrons Eq. (5-9) obtained by the simulation. The obtained functions for photoions Eq. (5-10) are shown in Figs. 5-5(c) and 5-5(d) as energy scale

$$\begin{cases} E_{ion,x} = \dfrac{p_{ion,x}^{\,2}}{2m_{ion}} = \dfrac{1}{2}\left[f_{ion,xy}\left(x_{ion} - x_{ion,0}\right)\right]^2 \\ E_{ion,y} = \dfrac{p_{ion,y}^{\,2}}{2m_{ion}} = \dfrac{1}{2}\left\{f_{ion,xy}\left[y_{ion} - y_{ion,0}(m_{ion})\right]\right\}^2 \\ E_{ion,z} = \dfrac{p_{ion,z}^{\,2}}{2m_{ion}} = \dfrac{1}{2}\left[f_{ion,z}\left(\dfrac{t_{ion} - t_{ion,0}(m_{ion})}{t_{ion,0}(m_{ion})}\right)\right]^2 \end{cases}, \quad (5\text{-}13)$$

because the energy as a function of the arrival time or the position is not dependent on its mass. The momentum vectors are derived from the recorded time and position by the linear interpolation of these functions.

5-3-4. Initial momentum of parent methanol molecules in an effusive beam

In the case of the *y* component of the momentum vector of a photoion, the origin $p_{ion,y}$

= 0 should be defined as the most probable momentum of the methanol sample in the effusive beam in the laboratory-fixed coordinates.

It is assumed that the momentum distribution of molecules in the laboratory-fixed coordinates at the exit of the nozzle can be expressed as Maxwell-Boltzmann distribution with translational temperature parallel (T_y) and perpendicular (T_{rxz}) as

$$f(\mathbf{p})\mathrm{d}p_x\mathrm{d}p_y\mathrm{d}p_z = \frac{1}{(2\pi mk_B)^{\frac{3}{2}}T_y^{\frac{1}{2}}T_{rxz}}\exp\left(-\frac{(p_y-p_{y0})^2}{2mk_BT_y}-\frac{{p_x}^2+{p_z}^2}{2mk_BT_{rxz}}\right)\mathrm{d}p_x\mathrm{d}p_y\mathrm{d}p_z . \quad (5\text{-}14)$$

where m is mass of the molecule and p_{y0} is the mean value of y component of the momentum. Because the distribution is symmetric about x and z, by using

$$p_{rxz} = \sqrt{{p_x}^2+{p_z}^2}, \mathrm{d}p_x\mathrm{d}p_z = 2\pi p_{rxz}\mathrm{d}p_{rxz}, \quad (5\text{-}15)$$

the distribution becomes

$$f(p_y,p_{rxz})\mathrm{d}p_y(2\pi p_{rxz}\mathrm{d}p_{rxz}) = \frac{1}{(2\pi mk_B)^{\frac{3}{2}}T_y^{\frac{1}{2}}T_{rxz}} \times\exp\left(-\frac{(p_y-p_{y0})^2}{2mk_BT_y}-\frac{{p_{rxz}}^2}{2mk_BT_{rxz}}\right)\mathrm{d}p_y(2\pi p_{rxz}\mathrm{d}p_{rxz}) . \quad (5\text{-}16)$$

This molecular beam is skimmed by a skimmer. Assuming the nozzle is a point, only the molecules whose momentum vectors satisfy

$$p_y<0, \frac{p_{rxz}}{|p_y|}<\tan\theta, \quad (5\text{-}17)$$

reach the crossing point with the laser beam, where $\tan\theta$ is defined as the ratio of the distance between the nozzle and the skimmer to the radius of the skimmer orifice. By integrating Eq. (5-16) in the range of Eq. (5-17),

$$\begin{aligned} f(p_y)\mathrm{d}p_y &= \left[\iint f(p_y,p_{rxz})(2\pi p_{rxz}\mathrm{d}p_{rxz})\right]\mathrm{d}p_y \\ &= \frac{2\pi}{(2\pi mk_B)^{\frac{3}{2}}T_y^{\frac{1}{2}}T_{rxz}}\left[\int_0^{-p_y\tan\theta}\exp\left(-\frac{{p_{rxz}}^2}{2mk_BT_{rxz}}\right)p_{rxz}\mathrm{d}p_{rxz}\right]\exp\left[-\frac{(p_y-p_{y0})^2}{2\pi mk_BT_y}\right]\mathrm{d}p_y \\ &= \frac{2\pi}{(2\pi mk_B)^{\frac{3}{2}}T_y^{\frac{1}{2}}T_{rxz}}\left[-mk_BT_{rxz}\exp\left(-\frac{{p_{rxz}}^2}{2mk_BT_{rxz}}\right)\right]_0^{-p_y\tan\theta}\exp\left[-\frac{(p_y-p_{y0})^2}{2mk_BT_y}\right]\mathrm{d}p_y \end{aligned}$$

$$f(p_y)\mathrm{d}p_y = \frac{1}{\sqrt{2\pi mk_BT_y}}\left[1-\exp\left(-\frac{{p_y}^2\tan^2\theta}{2mk_BT_{rxz}}\right)\right]\exp\left[-\frac{(p_y-p_{y0})^2}{2mk_BT_y}\right]\mathrm{d}p_y . \quad (5\text{-}18)$$

Here, assuming $\theta \ll 1$, Eq. (5-18) becomes

$$f(p_y)\mathrm{d}p_y \approx \frac{\theta^2}{\sqrt{\pi}(2mk_B)^{\frac{3}{2}}T_y^{\frac{1}{2}}T_{rxz}}{p_y}^2\exp\left(-\frac{(p_y-p_{y0})^2}{2mk_BT_y}\right)\mathrm{d}p_y , \quad (5\text{-}19)$$

where $p_y < 0$. Thus, the momentum distribution for the y component of molecules in an

effusive beam is approximated to the product of Gauss distribution and the quadratic function. Here, the derivative becomes

$$f'(p_y) \approx \frac{\theta^2}{\sqrt{\pi}(2mk_B)^{\frac{3}{2}} T_y^{\frac{1}{2}} T_{rxz}} \left(2p_y - \frac{{p_y}^3 - p_{y0}{p_y}^2}{mk_B T_y} \right) \exp\left(- \frac{(p_y - p_{y0})^2}{2mk_B T_y} \right). \quad (5\text{-}20)$$

Therefore, the most probable momentum p_{ym} is given by

$$p_{ym} = \frac{p_{y0}}{2} - \sqrt{\frac{{p_{y0}}^2}{4} + 2mk_B T_y} \ . \quad (5\text{-}21)$$

In the analysis, the momentum distribution of CH_3OH^+ in the laboratory-fixed coordinates is fitted to the model Eq. (5-19) and p_{ym} is obtained. The origin of the momentum vector of the fragment ions can be obtained as $(m_{ion}/m)p_{ym}$, where m_{ion} is the mass of the fragment ion and m is that of the parent ion.

5-3-5. Constraints of the signals and reconstruction of the missing signals

One electron or ion event needs seven signals from the detector, (t, x_1, x_2, y_1, y_2, z_1 and z_2), where t is the timing signal from the MCP. However, another signal originating from some noises or multi-hits may generate improper combination of (t, x_1, x_2, y_1, y_2, z_1, z_2). In order to choose only proper combinations, the time-sum conditions (Eq. (5-22)) and the offset condition (Eq. (5-23)) are known to be applied.

A sum of the arrival times of the two signals, each from the both ends of the delay-line, represents the length of the delay-line. Therefore, the sums ($T_{sum,u}$, $T_{sum,v}$ and $T_{sum,w}$), which are called a time-sums, take constant values as

$$\begin{cases} T_{sum,u} = x_1 + x_2 - 2t \\ T_{sum,v} = y_1 + y_2 - 2t \\ T_{sum,w} = z_1 + z_2 - 2t \end{cases} . \quad (5\text{-}22)$$

In addition, o defined as Eq. (5-8) should be zero

$$o = \frac{d_v}{d_u} v + \frac{d_w}{d_u} w - u = 0 \ , \quad (5\text{-}23)$$

so that the three patterns, Eqs. (5-2), (5-3) and (5-4), of (x, y) obtained from (u, v, w) are the same.

Because of imperfect detection efficiencies of the detectors, some of the signals could be lost. The defects of signals can be reproduced based on the time-sum conditions or the offset condition. In this thesis, the defects are reproduced from the time-sum conditions as follows. The flow chart is drawn in Fig. 5-6.

The timing signals are stored in the input array $a_{in}[i][j]$. The argument i (i = 0, 1, 2, 3, 4, 5, and 6) represents the channel (t, x_1, x_2, y_1, y_2, z_1, and z_2, respectively), and j represents the index of the signal. The number of detected signals for each channel is defined as n[i]. At first, the case when at least one t is recorded, i.e., n[0] > 0, is considered. When at least

one signal is recorded for every (x_1, x_2, y_1, y_2, z_1, z_2), i.e., n[i] > 0 for all i = 1 ~ 6, the one

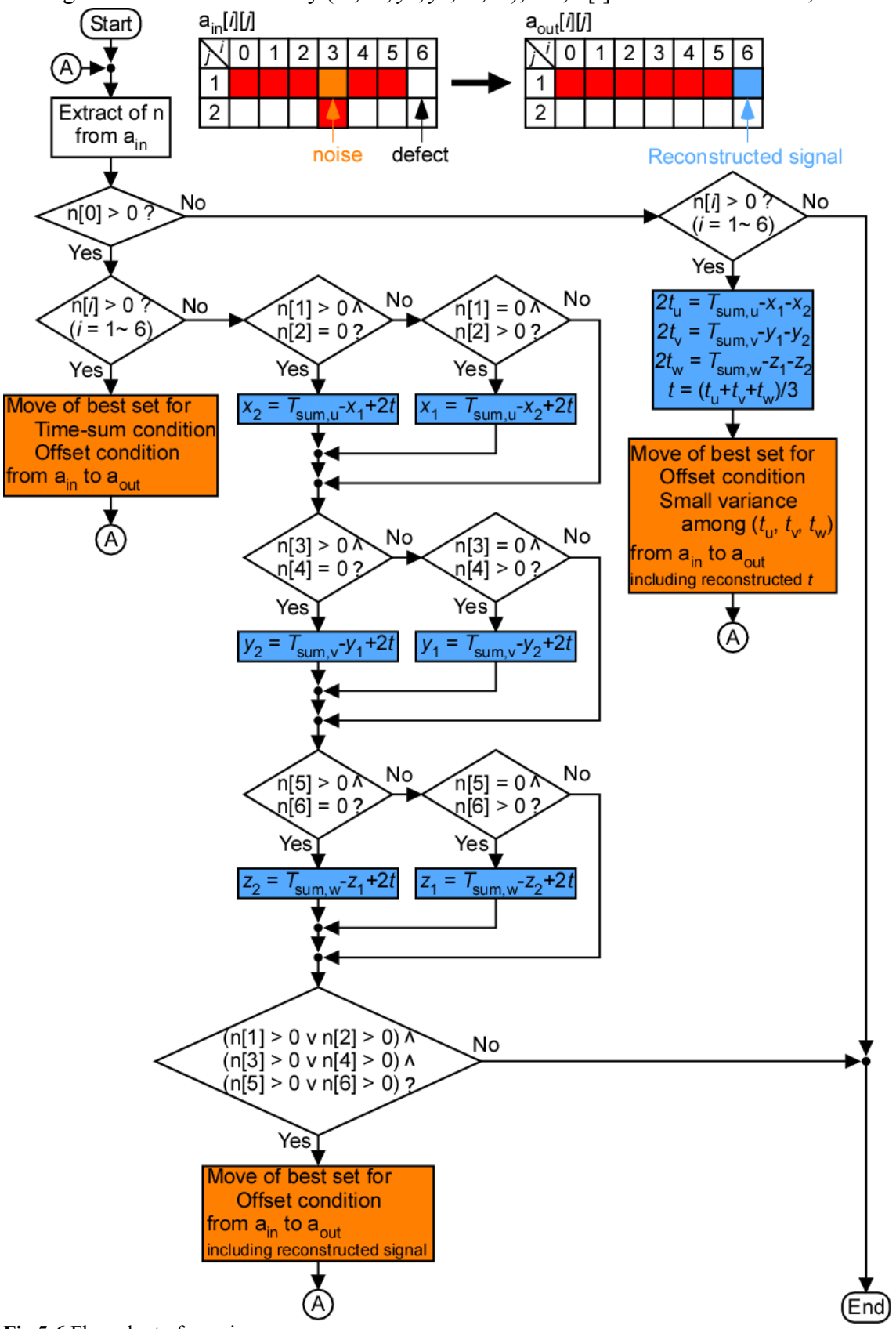

Fig.5-6 Flow chart of reassign.

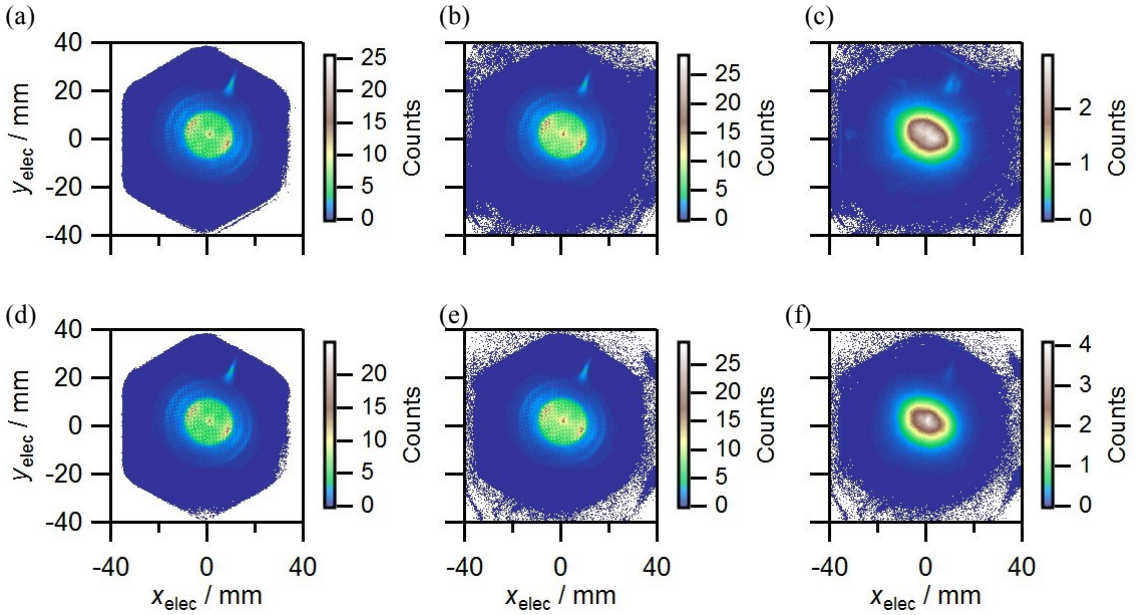

Fig.5-7 XY images for the electrons. (a) With taking into account both reassign strategy and constraints of the time-sum and offset conditions. (b) With taking into account the reassign strategy and without taking into account the constraints of the time-sum and offset conditions. (c) The difference between (a) and (b). (d) Without taking into account the reassign strategy and with taking into account the constraints of the time-sum and offset conditions. (e) Without taking into account both reassign strategy and constraints of the time-sum and offset conditions. (f) The difference between (d) and (e). The data are recorded in Chapter 7.

set of (t, x_1, x_2, y_1, y_2, z_1, z_2) which satisfies both Eqs. (5-22) and (5-23) best is chosen. When n[i] > 0 for not all i = 1 ~ 6, the defected signals are obtained from Eq. (5-22), if possible. For example, when x_1 signals is recorded but x_2 signals are not recorded, x_2 values are reconstructed as $x_2 = T_{sum,u}-x_1+2t$. Then, the set which satisfies Eq. (5-23) best is chosen. When t is not recorded, i.e., n[0] = 0, and at least one signal is recorded for every (x_1, x_2, y_1, y_2, z_1, z_2), i.e., n[i] > 0 for all i = 1 ~ 6, respective t values are obtained as the mean values among t_u, t_v, and t_w derived from Eq. (5-22) for u, v and w. Then, the set which satisfies Eq. (5-23) best and in which variance among t_u, t_v, and t_w is small is chosen. The chosen set above is moved from a_{in} and the chosen set including the reconstructed signals are entered to a new array a_{out}. This strategy, which is named as *reassign*, is repeated until the set cannot be determined.

Figure 5-7 shows the *xy* detector image for electrons, recorded in Chapter 7. In Figs. 5-7(a) and 5-7(b), the *reassign* strategy is utilized, and in Figs. 5-6(d) and 5-6(e), the *reassign* strategy is not utilized. In Figs. 5-7(a) and 5-7(d), the constraint of the time-sum (Eqs. (5-22)) and offset (Eq. (5-23)) conditions are taken into account, and in Figs. 5-7(b) and 5-7(e), the constraint of the time-sum and offset conditions are not taken into account. Based on the comparison between Figs. 5-7(a) and 5-7(d), the electron yield increases by a factor of 1.07 through the *reassign* strategy. Similarly, the ion yield increases by a factor of 1.11, and the yield of the coincident detection increases by a factor of 1.18 in total.

When the constraints are not taken into account (Figs. 5-7(b) and 5-7(e)), the *xy* images exhibit noise signals outer the hexagon, which is ascribed to the Hexanode detector. These noise signals are eliminated by the constraints as shown in Figs. 5-7(a) and 5-7(d). In addition, the larger yields close to the center area can be seen in Figs. 5-6(b) and 5-6(e) than that in Figs. 5-7(a) and 5-7(d). Figure 5-7(c) shows the difference between Figs. 5-7(a) and 5-7(b), and Fig. 5-7(f) shows the difference between Figs. 5-7(d) and 5-7(e). The *xy* images exhibit the broad distribution around the center position in Figs. 5-7(c) and 5-7(f), i.e., only when the constraints are not taken into account. The origin of this signals are described in Sec. 5-3-6. In Fig. 5-7(c), other noises can be recognized,

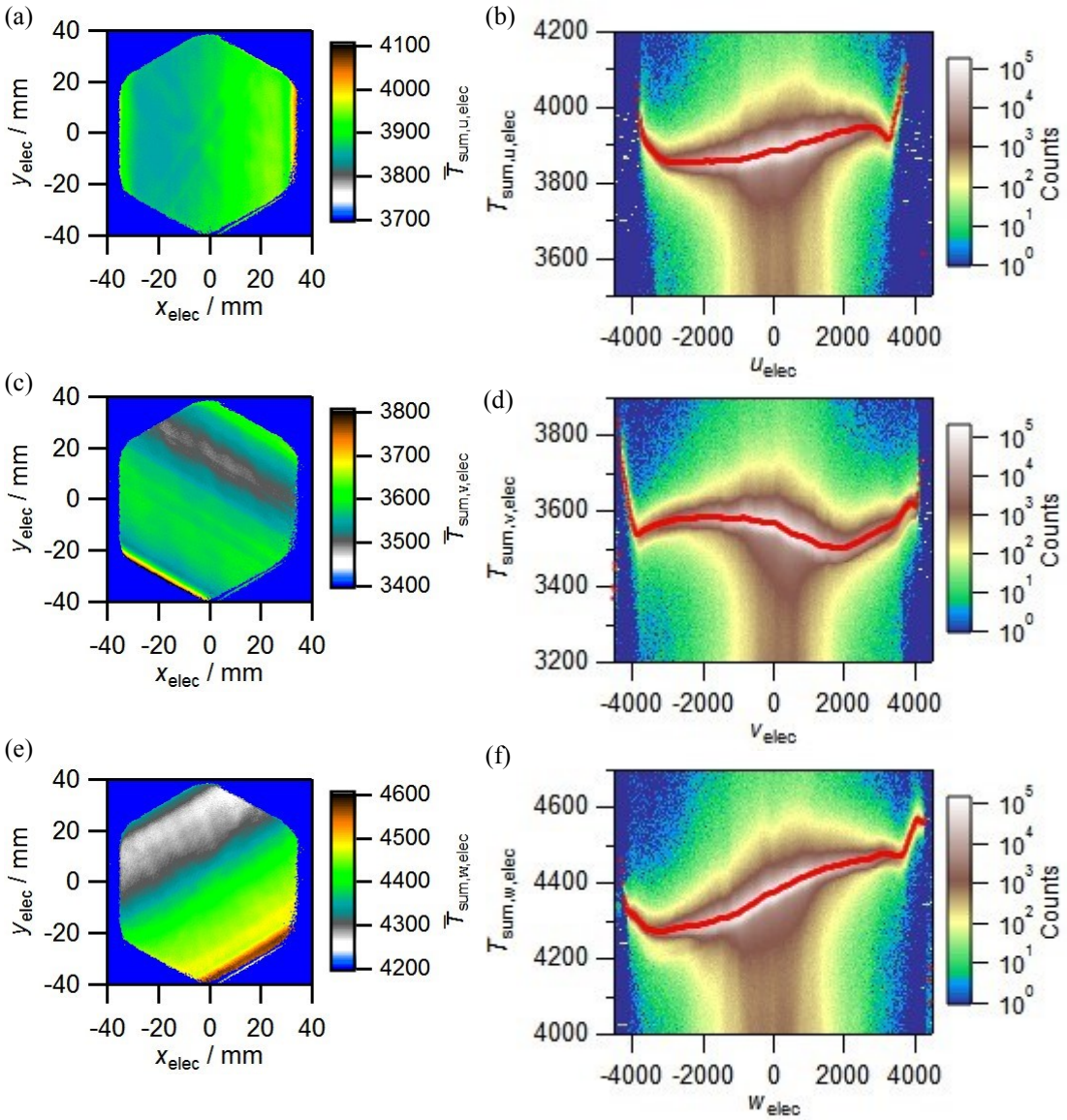

Fig.5-8 (a) The mean value of $T_{sum,u,elec}$ at each (x_{elec}, y_{elec}). (b) The two-dimensional histogram of u_{elec} and $T_{sum,u,elec}$. Red line is the mean value of $T_{sum,u,elec}$ at each u_{elec}. (c) The mean value of $T_{sum,v,elec}$ at each (x_{elec}, y_{elec}). (d) The two-dimensional histogram of v_{elec} and $T_{sum,v,elec}$. Red line is the mean value of $T_{sum,v,elec}$ at each v_{elec}. (e) The mean value of $T_{sum,w,elec}$ at each (x_{elec}, y_{elec}). (f) The two-dimensional histogram of w_{elec} and $T_{sum,w,elec}$. Red line is the mean value of $T_{sum,w,elec}$ at each w_{elec}. The data are recorded in Chapter 7.

compared with Fig. 5-7(f). These noises may be ascribed to the mistake of the *reassign* strategy, but they can be eliminated by the constraints.

5-3-6. Position dependence of time-sums

Time-sum condition (Eq. (5-22)) is ascribed to the length of the delay-line anode, indicating that the time-sum is not dependent on the position. However, the time-sum is dependent on the position. Figures 5-8(a), 5-8(c) and 5-8(e) show the mean values of the time-sums at each position for *u*, *v* and *w*, respectively. The result of only the PSD for electrons is shown, but the same procedure is utilized for the PSD for ions. As shown in these figures, the time-sums are almost a function of *u*, *v*, and *w*, respectively. Figures 5-8(b), 5-8(d) and 5-8(f) show the 2D histograms of the positions and the time-sums. In addition, the mean values of time-sums ($\overline{T}_{\mathrm{sum,u}}(u)$, $\overline{T}_{\mathrm{sum,v}}(v)$ and $\overline{T}_{\mathrm{sum,w}}(w)$) as a function of the position are obtained as shown in the figures.

Time-sum differences ($T_{\mathrm{sumdif,\,u}}$, $T_{\mathrm{sumdif,\,v}}$ and $T_{\mathrm{sumdif,w}}$) are defined as the differences between the time-sums of each laser shot and the mean values as

$$\begin{cases} T_{\mathrm{sumdif,u}} = T_{\mathrm{sum,u}} - \overline{T}_{\mathrm{sum,u}}(u) = x_1 + x_2 - 2t - \overline{T}_{\mathrm{sum,u}}(x_1 - x_2) \\ T_{\mathrm{sumdif,v}} = T_{\mathrm{sum,v}} - \overline{T}_{\mathrm{sum,v}}(v) = y_1 + y_2 - 2t - \overline{T}_{\mathrm{sum,v}}(y_1 - y_2) \\ T_{\mathrm{sumdif,w}} = T_{\mathrm{sum,w}} - \overline{T}_{\mathrm{sum,w}}(w) = z_1 + z_2 - 2t - \overline{T}_{\mathrm{sum,w}}(z_1 - z_2) \end{cases}, \tag{5-24}$$

and their histograms are shown in Fig. 5-9. The histograms of the time-sums are also shown as the dotted lines in the figures, whose horizontal axis is shifted by the center values. By taking the time-sum differences, the widths of the distributions become small. The constraints are set as time-sum differences to be $T_{\mathrm{sumdif},i} = \pm 60$ (= 1.5 ns) (*i* = u, v, w) in the following chapters. In Fig. 5-9, there are some values of the time-sum difference at which the histograms exhibit an extremely large signal intensity (e.g., $T_{\mathrm{sumdif,}} = 0$), originating from the *reassign* strategy describing in Section 5-3-4. The position dependence of the time-sums is also taken into account in the *reassign* strategy.

In addition, the large signals can be seen in the broad range of $T_{\mathrm{sumdif,}} < 0$, only for

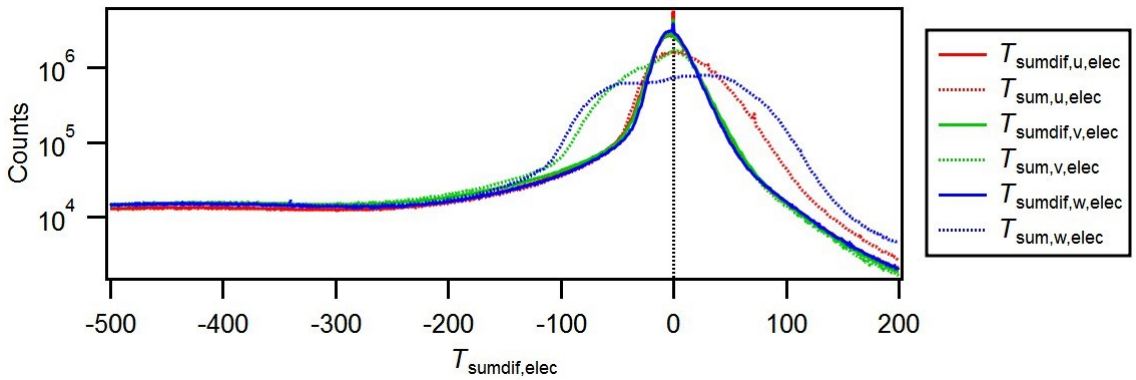

Fig.5-9 Solid lines: The distribution of $T_{\mathrm{sumdif,elec}}$. Dashed lines: The distribution of $T_{\mathrm{sum,elec}}$, whose horizontal axis is shifted by their most probable values. Red, green and blue lines are *u*, *v* and *w*, respectively. The data are recorded in Chapter 7.

electrons but not for ions. These noises in the T_{sumdif} histograms are the origin of the broad noise in the *xy* image shown in Figs. 5-6(e) and 5-6(f). In the case of electrons, the time window is limited within several nanoseconds as shown in Fig. 5-5(b). Because the deadtime of the CFD is larger than 10 ns [175], the multihit signals from the MCP cannot be recorded. Also for the delay-line anodes, some multihit signals cannot be recorded when the positions of the multihit are close to each other, indicating that only the earlier signals are recorded for both ends of the delay-line. Consequently, the multihit of electrons generates the signal whose time-sum seems to be small and position seems to be close to the center.

5-3-7. Adjustment of signal velocities of delay-line anodes

The propagation velocities of the delay-line signal are approximated to be $v_u = 0.737$ mm/ns, $v_v = 0.706$ mm/ns, $v_w = 0.684$ mm/ns, which were written in the manual (version 9.22.1003.1) of the delay-line anode [176], but it is noted that the velocities should be calibrated for each detector in the recent version of the manual (version 11.0.1304.1) [177]. In this study, the calibration the velocities is performed as follows. The result of only the PSD for electrons is shown, but the same procedure is utilized for the PSD for ions.

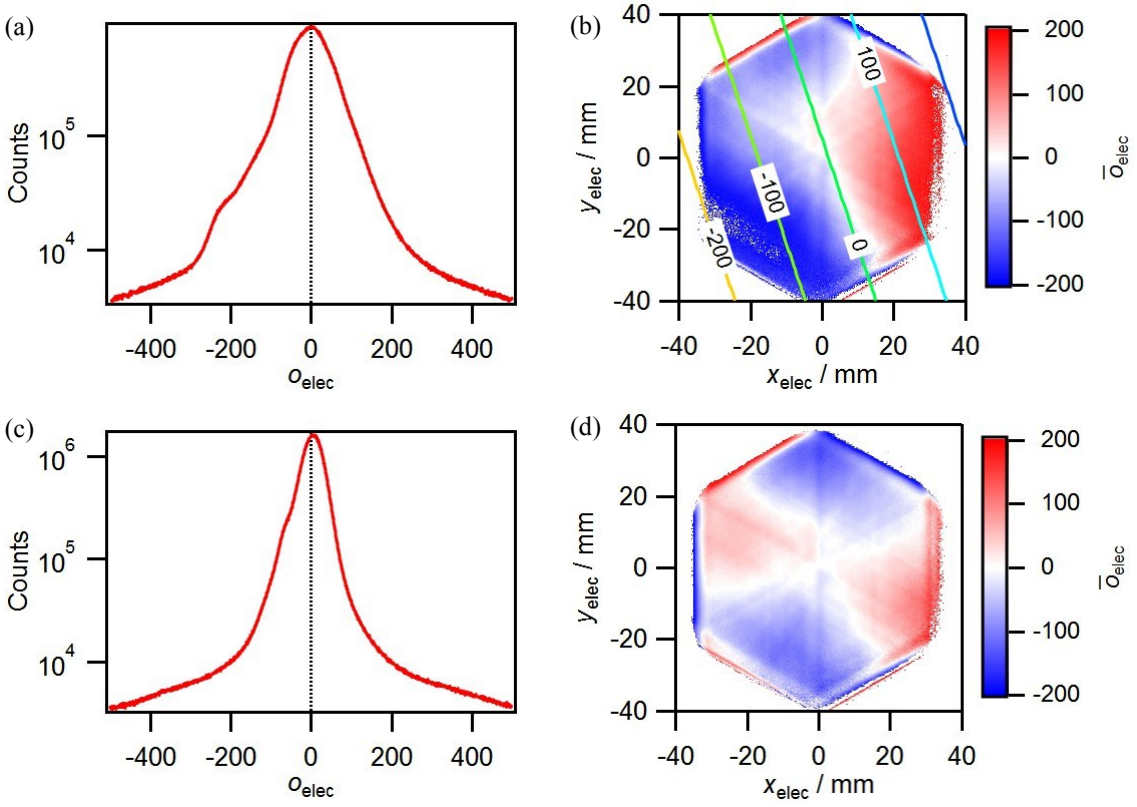

Fig.5-10 (a) The distribution of o_{elec} when the velocities are not adjusted. (b) The mean value of o_{elec} at each (x_{elec}, y_{elec}) when the velocities are not adjusted. Contour plot is the result of linear fit. (c) The distribution of o_{elec} when the velocities are adjusted. (b) The mean value of o_{elec} at each (x_{elec}, y_{elec}) when the velocities are adjusted. The data are recorded in Chapter 7.

If the velocities have deviations, o depends on the positions (x, y) linearly. By using the position dependence of $o(x, y)$, the velocities are calibrated. Figure 5-10(a) shows the histogram of o when the velocities noted in the manual (9.22.1003.1) are used. The mean value of o at each position (x, y) is shown as $\bar{o}(x, y)$ in Fig. 5-10(b). Although the value of o_0 is adjusted so that the center of the distribution of o becomes $o = 0$, as shown in Fig. 5-10(a), the mean value depends on the position. The contour plots shown in Fig. 5-10(b) are the results of the least-squares analysis which assumes o depends on x, y linearly.

When the true value, $d_i = d_{i0}$ and $o_0 = o_{00}$ is used in Eq. (5-8), o becomes $o = 0$ as

$$0 = \frac{d_{v0}}{d_{u0}} v + \frac{d_{w0}}{d_{u0}} (w - o_0 + o_{00}) - u \,. \tag{5-25}$$

Because only the ratios of d_i can be determined, d_{u0} is set to be $d_{u0} = d_u$. By taking the difference between Eqs.(5-8) and (5-25),

$$o = \frac{d_v - d_{v0}}{d_u} v + \frac{d_w - d_{w0}}{d_u} w + \frac{d_{w0}}{d_u} (o_0 - o_{00}) \tag{5-26}$$

is derived. From Eqs. (5-6) and (5-7), the two of the three positions can be derived as

$$d_v v = \frac{x + \sqrt{3} y}{2} + \frac{1}{3} d_u o, d_w w = \frac{x - \sqrt{3} y}{2} + \frac{1}{3} d_u o. \tag{5-27}$$

Therefore, the relation

$$o(x, y) = \frac{3\left[\left(2 - \frac{d_{v0}}{d_v} - \frac{d_{w0}}{d_w}\right) x - \sqrt{3}\left(\frac{d_{v0}}{d_v} - \frac{d_{w0}}{d_w}\right) y + 2 d_{w0} (o_0 - o_{00})\right]}{2 d_u \left(1 + \frac{d_{v0}}{d_v} + \frac{d_{w0}}{d_w}\right)} \tag{5-28}$$

is obtained, suggesting that the true velocities, d_{v0}, d_{w0}, and the true offset, o_{00}, can be determined by the approximation of the position dependence linearly. Thus, the ratio of the velocities d_v / d_u and d_w / d_u are obtained. The results obtained with these parameters are shown in Figs. 5-10(c) and 5-10(d). The FWHMs of Figs. 5-10(a) and 5-10(c) are 109 and 58, respectively, indicating that the width of the o-distribution becomes small by using the new parameters. It should be noted that, as shown in Fig. 5-10(d), although the position dependence of o becomes small, the non-linear dependence still remains. In addition, the value of o becomes irregular at the edge of the PSD because the position cannot be recorded correctly. The similar structure at the edge is also observed in Fig. 5-8.

6. Channel-specific LF- and MF-PAD for dissociative ionization of methanol in intense UV laser fields

本章については、以下の雑誌に刊行予定のため、非公開。
Channel-specific photoelectron angular distribution in laboratory and molecular frames for dissociative ionization of methanol in intense ultraviolet laser fields, Chemical Physics Letters **672**, 7-12 (2017)

7. Orientation-resolved PAD for dissociative ionization of methanol in intense UV laser fields

本章については、5 年以内に雑誌等で刊行予定のため、非公開。

8. Laser-intensity dependence of dissociative ionization of methanol in intense UV laser fields

本章については、5 年以内に雑誌等で刊行予定のため、非公開。

9. Summary and outlook

Carrier-envelope phase (CEP) [70,71] is an important parameter to control molecular dynamics in intense few-cycle laser fields. However, as shown in Chapter 3, CEP is varied through propagation of the laser pulse in dispersed media, such as air. Therefore, determination of absolute CEP at the laser-molecule interaction point has been a crucial problem.

In this thesis, Chapter 4, I demonstrated that the absolute CEP at the laser-molecule interaction point can be determined by recording angle-resolved photoelectron spectra of Ar in circularly polarized few-cycle laser fields with the CEP-tagging method. On the basis of theory of tunnel ionization and subsequent motion of the electron, described in Chapter 2, absolute CEP can be determined without the aid of numerical calculation. The effect of depletion of neutral Ar atoms [69] and that of Columbic potential of Ar^+ on motion of the electron are also examined by classical trajectory Monte Carlo (CTMC) simulation. It is found that the absolute CEP determined by comparing the experimental result in the high photoelectron energy range with the numerical simulation taking into account the two effect above is the same as the absolute CEP expected with taking into account neither of the two effect above, that is, without numerical calculation. This method is applicable when the laser intensity is in the range between 1×10^{14} W/cm^2 and 6×10^{14} W/cm^2 with the pulse duration of 4.1 fs. When the laser intensity increases, the depletion effect becomes significant.

The absolute CEP to be determined by this method can be applied to investigation of CEP dependence of dissociation of molecules in intense few-cycle laser fields. It is known that fragmentation processes of polyatomic molecules vary sensitively depending on the CEP, because the kinetic energy of the recolliding electron, which induces the fragmentation, depends on the absolute CEP [81]. Therefore, the control of the fragmentation pathways of polyatomic molecules such as ethylene may be one of the application of the determined absolute CEP.

Based on this study, not only the absolute CEP is determined but also the depletion effect can be investigated. In this thesis, by comparing the depletion effect in the experimental result with that in the CTMC simulation, a scale factor of 0.27 is introduced to the ionization rate obtained by Ammosov-Delone-Krainov (ADK) theory [31]. Consequently, the absolute ionization rate can be possibly estimated by this method.

The Coulombic potential effect has also been an attractive issue in the intense laser science. The effect of the Coulombic potential on the motion of the electrons can be investigated through the qualitative evaluation of the effect as a function of the

photoelectron energy, because the effect is expected to become smaller as the photoelectron energy increases.

Furthermore, ionization and subsequent excitation pathways to prepare electronically excited states of parent cations in dissociative ionization of molecules in intense laser fields have been an attractive research topic in these years. Particularly, these pathways have securely been revealed by photoelectron-photoion coincidence momentum imaging (PEPICO-MI) [114,115,118].

In this thesis, by using the PEPICO-MI experimental setup described in Chapter 5, dissociative ionization of methanol in intense UV femtosecond laser fields (~ 400 nm) is investigated, on the basis of channel-specific and energy-resolved photoelectron angular distribution (PAD). As shown in Chapter 6, it is revealed by channel-specific PADs in the laboratory-frame and molecular-frame at 8.9×10^{12} W/cm^2 that CH_3OH^+ is decomposed into CH_2OH^+ + H when the four-photon ionization to the vibrationally highly excited states in the electronic ground $\tilde{X}$ state of CH_3OH^+ occurs, while is decomposed into CH_3^+ + OH when the five-photon ionization to the second electronically excited $\tilde{B}$ state occurs. In addition, both fragmentation processes occur through the four-photon ionization to the $\tilde{X}$ state followed by subsequent electronic photoexcitation.

Orientation-resolved PADs are recorded at 3.1×10^{13} W/cm^2, assuming the CH_3^+ ejection direction represents the orientation of the C-O bond axis, in Chapter 7. Because the photoelectron emission is correlated with both the direction of the laser polarization axis and the direction of the C-O bond axis, the orientation-resolved PADs in the stereographic drawing are constructed. It is revealed that when the four-photon ionization to the $\tilde{X}$ state occurs, the photoelectron emission is parallel to the laser polarization direction irrespective to the orientation of the C-O bond axis, while when the five-photon ionization to the $\tilde{B}$ state occurs, the photoelectrons prefers to be ejected from the O atom side rather than the C atom side at the parallel orientation and to be ejected along the direction not only parallel but also perpendicular to the laser polarization direction at the perpendicular orientation.

The laser intensity dependence of the channel-specific photoelectron spectra and the PADs described in Chapter 8 shows that the two-photon resonance with the 3s Rydberg state, which is dissociative along the O-H bond, plays an important role in the four-photon ionization to the $\tilde{X}$ state when the laser intensity is lower than 1×10^{13} W/cm^2. It is also revealed that the dominant pathway in the CH_2OH^+ formation is switched from the four-photon ionization to the vibrationally highly excited states in the $\tilde{X}$ state to the five-photon ionization to the $\tilde{B}$ state.

As shown in Chapters 6 ~ 8, the channel-specific PAD recorded by PEPICO-MI is a

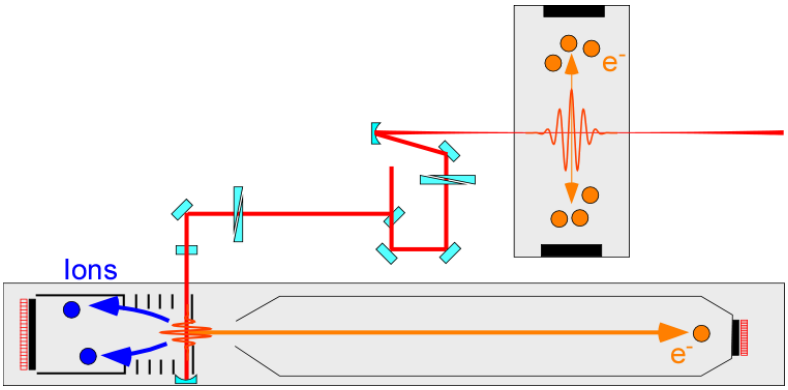

Fig.9-1 Schematic picture of the new PEPICO-MI experimental setup with a phasemeter.

powerful tool to investigate dissociative ionization of molecules in intense laser fields. Because the PADs are strongly dependent on the orientation of molecular axis as shown in this thesis, the interpretation of the PADs on the basis of molecular orbitals (MOs) needs to be taken into account the orientation effect. Now, I am trying to explain the observed orientation-resolved PADs with the aid of the theoretical calculation, such as MO strong-field approximation (MO-SFA) [192] or time-dependent density functional theory (TD-DFT) [196]. In addition, orientation-resolved PADs have a possibility to extract the orientation dependence of the ionization and excitation probability, and thus obtained excitation probability offers us to identify the excitation pathways clearly.

The channel-specific PAD for the parent cation, which is the similar as that of ionization to the electronically excited state rather than to the ground state, suggesting that the deexcitation, that is, stimulated emission in the intense laser fields, from the electronically excited states of the parent cation to the ground state occur. Further investigation is necessary in this context. The kinetic energy of the fragment ion is treated as its mean value in this thesis, but the higher kinetic energy range may correspond to the absorption of more photons in the excitation process. Therefore, the orientation-resolved PAD further-resolved by the released kinetic energy of the fragment ion is also the future work.

As above, the absolute CEP at the laser-molecule interaction point can be determined by the method described in this thesis, and the PEPICO-MI and the channel-specific PAD are useful to examine dissociative ionization of molecules in intense laser fields. Now I am constructing a new PEPICO-MI apparatus whose photoelectron spectrometer was used in Chapter 4. Figure 9-1 shows the schematic picture of the new PEPICO-MI apparatus. It is noteworthy that this photoelectron spectrometer can be performed not only in the field-free mode as in this thesis, but also in the angle-resolved mode [197]. Consequently, the CEP dependence of dissociative ionization of molecules in intense few-cycle laser fields can be investigated by the new PEPICO-MI apparatus with the determined absolute CEP.

Appendices

Appendice A-1, A-2, A-3 and A-4 are related to Chapter 4. Appendices A-5 and A-6 are related to Chapter 6 ~ 8 and Appendix A-7 is related to Chapter 7.

関連する章の内容が 5 年以内に雑誌等で刊行予定のため、非公開。

References

[1] K. Yamanouchi, *Science* **295,** 1659 (2002).
[2] J. H. Posthumus, *Rep. Prog. Phys.* **67,** 623 (2004).
[3] H. Stapelfeldt and T. Seideman, *Rev. Mod. Phys.* **75,** 543 (2003).
[4] A. Hishikawa, A. Iwamae, and K. Yamanouchi, *J. Chem. Phys.* **111,** 8871 (1999).
[5] A. Hishikawa, A. Iwamae, and K. Yamanouchi, *Phys. Rev. Lett.* **83,** 1127 (1999).
[6] H. Hasegawa, A. Hishikawa, and K. Yamanouchi, *Chem. Phys. Lett.* **349,** 57 (2001).
[7] A. Iwasaki, A. Hishikawa, and K. Yamanouchi, *Chem. Phys. Lett.* **346,** 379 (2001).
[8] A. McPherson, G. Gibson, H. Jara, U. Johann, T. S. Luk, I. A. McIntyre, K. Boyer, and C. K. Rhodes, *J. Opt. Soc. Am. B.* **4,** 595 (1987).
[9] M. Ferray, A. L'Huillier, X. F. Li, L. A. Lompre, G. Mainfray, and C. Manus, *J. Phys. B:At. Mol. Opt. Phys.* **21,** L31 (1988).
[10] P. B. Corkum, *Phys. Rev. Lett.* **71,** 1994 (1993).
[11] P. Agostini, F. Fabre, G. Mainfray, G. Petite, and N. Rahman, *Phys. Rev. Lett.* **42,** 1127 (1979).
[12] M. Protopapas, C. H. Keitel, and P. L. Knight, *Rep. Prog. Phys.* **60,** 389 (1997).
[13] L. J. Frasinski, K. Codling, P. A. Hatherly, J. Barr, I. Ross, and W. Toner, *Phys. Rev. Lett.* **58,** 2424 (1987).
[14] D. Normand, C. Cornaggia, J. Lavancier, J. Morellec, and H. Liu, *Phys. Rev. A* **44,** 475 (1991).
[15] C. Cornaggia, J. Lavancier, D. Normand, J. Morellec, P. Agostini, J. P. Chambaret, and A. Antonetti, *Phys. Rev. A* **44,** 4499 (1991).
[16] D. Fittinghoff, P. Bolton, B. Chang, and K. Kulander, *Phys. Rev. Lett.* **69,** 2642 (1992).
[17] K. Codling and L. J. Frasinski, *J. Phys. B:At. Mol. Opt. Phys.* **26,** 783 (1993).
[18] F. Fabre, G. Petite, P. Agostini, and M. Clement, *J. Phys. B:At. Mol. Phys.* **15,** 1353 (1982).
[19] P. Kruit, J. Kimman, H. G. Muller, and M. van der Wiel, *Phys. Rev. A* **28,** 248 (1983).
[20] T. Kibble, *Phys. Rev.* **150,** 1060 (1966).
[21] M. J. Hollis, *Opt. Commun.* **25,** 395 (1978).
[22] P. H. Bucksbaum, R. R. Freeman, M. Bashkansky, and T. J. McIlrath, *J. Opt. Soc. Am. B-Opt. Phys.* **4,** 760 (1987).
[23] R. R. Freeman, P. H. Bucksbaum, H. Milchberg, S. Darack, D. Schumacher, and M. Geusic, *Phys. Rev. Lett.* **59,** 1092 (1987).
[24] R. Wiehle, B. Witzel, H. Helm, and E. Cormier, *Phys. Rev. A* **67,** 063405 (2003).
[25] H. Helm, N. Bjerre, M. Dyer, D. Huestis, and M. Saeed, *Phys. Rev. Lett.* **70,** 3221 (1993).
[26] G. Gibson, R. R. Freeman, and T. McIlrath, *Phys. Rev. Lett.* **67,** 1230 (1991).
[27] L. V. Keldysh, *Sov. Phys. JETP* **20,** 1307 (1965).
[28] F. H. M. Faisal, *J. Phys. B:At. Mol. Phys.* **6,** L89 (1973).
[29] H. Reiss, *Phys. Rev. A* **22,** 1786 (1980).
[30] D. M. Wolkow, *Z. Phys.* **94,** 250 (1935).
[31] M. V. Ammosov, N. B. Delone, and V. P. Krainov, *Sov. Phys. JETP* **64,** 1191 (1986).
[32] X. M. Tong, Z. X. Zhao, and C. D. Lin, *Phys. Rev. A* **66,** 033402 (2002).
[33] T. Kjeldsen, C. Z. Bisgaard, L. B. Madsen, and H. Stapelfeldt, *Phys. Rev. A* **71,** 013418 (2005).
[34] G. G. Paulus, W. Becker, W. Nicklich, and H. Walthe, *J. Phys. B:At. Mol. Opt. Phys.* **27,** L703 (1994).
[35] G. G. Paulus, W. Nicklich, H. Xu, P. Lambropoulos, and H. Walther, *Phys. Rev. Lett.* **72,** 2851 (1994).
[36] T. Nubbemeyer, K. Gorling, A. Saenz, U. Eichmann, and W. Sandner, *Phys. Rev. Lett.* **101,** 233001 (2008).
[37] T. Brabec, M. Y. Ivanov, and P. B. Corkum, *Phys. Rev. A* **54,** R2551 (1996).
[38] D. Comtois, D. Zeidler, H. Pépin, J. C. Kieffer, D. M. Villeneuve, and P. B. Corkum, *J. Phys. B:At. Mol. Opt. Phys.* **38,** 1923 (2005).
[39] C. Huang, Q. Liao, Y. Zhou, and P. Lu, *Opt. Exp.* **18,** 14293 (2010).

[40] L. Zhang, X. Xie, S. Roither, Y. Zhou, P. Lu, D. Kartashov, M. Schöffler, D. Shafir, P. B. Corkum, A. Baltuška, A. Staudte, and M. Kitzler, *Phys. Rev. Lett.* **112,** 193002 (2014).
[41] X. Gong, P. He, Q. Song, Q. Ji, H. Pan, J. Ding, F. He, H. Zeng, and J. Wu, *Phys. Rev. Lett.* **113,** 203001 (2014).
[42] L. Zhang, X. Xie, S. Roither, D. Kartashov, Y. Wang, C. Wang, M. Schöffler, D. Shafir, P. B. Corkum, A. Baltuška, I. Ivanov, A. Kheifets, X. Liu, A. Staudte, and M. Kitzler, *Phys. Rev. A* **90,** 061401 (2014).
[43] J. Henkel and M. Lein, *Phys. Rev. A* **92,** 013422 (2015).
[44] J. Geng, W. H. Xiong, X. R. Xiao, L. Y. Peng, and Q. Gong, *Phys. Rev. Lett.* **115,** 193001 (2015).
[45] G. Lambert, B. Vodungbo, J. Gautier, B. Mahieu, V. Malka, S. Sebban, P. Zeitoun, J. Luning, J. Perron, A. Andreev, S. Stremoukhov, F. Ardana-Lamas, A. Dax, C. P. Hauri, A. Sardinha, and M. Fajardo, *Nat. Commun.* **6,** 6167 (2015).
[46] J. L. Chaloupka and D. D. Hickstein, *Phys. Rev. Lett.* **116,** 143005 (2016).
[47] O. Kfir, P. Grychtol, E. Turgut, R. Knut, D. Zusin, D. Popmintchev, T. Popmintchev, H. Nembach, J. M. Shaw, A. Fleischer, H. Kapteyn, M. Murnane, and O. Cohen, *Nat. Photonics* **9,** 99 (2014).
[48] H. Yazawa, T. Shioyama, Y. Suda, F. Kannari, R. Itakura, and K. Yamanouchi, *J. Chem. Phys.* **125,** 184311 (2006).
[49] R. Itakura, P. Liu, Y. Furukawa, T. Okino, K. Yamanouchi, and H. Nakano, *J. Chem. Phys.* **127,** 104306 (2007).
[50] H. Xu, T. Okino, T. Kudou, K. Yamanouchi, S. Roither, M. Kitzler, A. Baltuška, and S. L. Chin, *J. Phys. Chem. A* **116,** 2686 (2012).
[51] U. Lev, L. Graham, C. B. Madsen, I. Ben-Itzhak, B. D. Bruner, B. D. Esry, H. Frostig, O. Heber, A. Natan, V. S. Prabhudesai, D. Schwalm, Y. Silberberg, D. Strasser, I. D. Williams, and D. Zajfman, *J. Phys. B:At. Mol. Opt. Phys.* **48,** 201001 (2015).
[52] V. V. Yakovlev, C. J. Bardeen, J. Che, J. Cao, and K. R. Wilson, *J. Chem. Phys.* **108,** 2309 (1998).
[53] R. Itakura, K. Yamanouchi, T. Tanabe, T. Okamoto, and F. Kannari, *J. Chem. Phys.* **119,** 4179 (2003).
[54] M. Wollenhaupt, A. Präkelt, C. Sarpe-Tudoran, D. Liese, and T. Baumert, *Appl. Phys. B* **82,** 183 (2006).
[55] T. Nakajima, *Phys. Rev. A* **75,** 053409 (2007).
[56] M. Krug, T. Bayer, M. Wollenhaupt, C. Sarpe-Tudoran, T. Baumert, S. S. Ivanov, and N. V. Vitanov, *New J. Phys.* **11,** 105051 (2009).
[57] J. Plenge, A. Wirsing, C. Raschpichler, M. Meyer, and E. Rühl, *J. Chem. Phys.* **130,** 244313 (2009).
[58] D. Irimia and M. H. M. Janssen, *J. Chem. Phys.* **132,** 234302 (2010).
[59] D. Geißler, T. Rozgonyi, J. González-Vázquez, L. González, P. Marquetand, and T. C. Weinacht, *Phys. Rev. A* **84,** 053422 (2011).
[60] R. J. Levis, G. M. Menkir, and H. Rabitz, *Science* **292,** 709 (2001).
[61] H. Yazawa, T. Tanabe, T. Okamoto, M. Yamanaka, F. Kannari, R. Itakura, and K. Yamanouchi, *J. Chem. Phys.* **124,** 204314 (2006).
[62] H. Ohmura, N. Saito, H. Nonaka, and S. Ichimura, *Phys. Rev. A* **77,** 053405 (2008).
[63] H. Li, D. Ray, S. De, I. Znakovskaya, W. Cao, G. Laurent, Z. Wang, M. F. Kling, A. Le, and C. L. Cocke, *Phys. Rev. A* **84,** 43429 (2011).
[64] H. Ohmura, N. Saito, and T. Morishita, *Phys. Rev. A* **83,** 063407 (2011).
[65] D. G. Arbó, C. Lemell, S. Nagele, N. Camus, L. Fechner, A. Krupp, T. Pfeifer, S. D. López, R. Moshammer, and J. Burgdörfer, *Phys. Rev. A* **92,** 023402 (2015).
[66] S. Skruszewicz, J. Tiggesbaumker, K. H. Meiwes-Broer, M. Arbeiter, T. Fennel, and D. Bauer, *Phys. Rev. Lett.* **115,** 043001 (2015).
[67] V. Wanie, H. Ibrahim, S. Beaulieu, N. Thiré, B. E. Schmidt, Y. Deng, A. S. Alnaser, I. V. Litvinyuk, X. Tong, and F. Légaré, *J. Phys. B:At. Mol. Opt. Phys.* **49,** 025601 (2016).
[68] H. Ohmura and N. Saito, *Phys. Rev. A* **92,** 053408 (2015).

[69] P. Dietrich, F. Krausz, and P. B. Corkum, *Opt. Lett.* **25,** 16 (2000).
[70] A. Baltuška, T. Udem, M. Uiberacker, M. Hentschel, E. Goulielmakis, C. Gohle, R. Holzwarth, V. S. Yakovlev, A. Scrinzi, T. W. Hansch, and F. Krausz, *Nature* **421,** 611 (2003).
[71] G. G. Paulus, F. Grasbon, H. Walther, P. Villoresi, M. Nisoli, S. Stagira, E. Priori, and S. De Silvestri, *Nature* **414,** 182 (2001).
[72] M. Nisoli, S. De Silvestri, and O. Svelto, *Appl. Phys. Lett.* **68,** 2793 (1996).
[73] G. G. Paulus, F. Lindner, H. Walther, A. Baltuška, E. Goulielmakis, M. Lezius, and F. Krausz, *Phys. Rev. Lett.* **91,** 253004 (2003).
[74] M. F. Kling, C. Siedschlag, A. J. Verhoef, J. I. Khan, M. Schultze, T. Uphues, Y. Ni, M. Uiberacker, M. Drescher, F. Krausz, and M. J. J. Vrakking, *Science* **312,** 246 (2006).
[75] M. F. Kling, C. Siedschlag, I. Znakovskaya, A. J. Verhoef, S. Zherebtsov, F. Krausz, M. Lezius, and M. J. J. Vrakking, *Mol. Phys.* **106,** 455 (2008).
[76] S. Chelkowski and A. D. Bandrauk, *Phys. Rev. A* **71,** 053815 (2005).
[77] P. von den Hoff, I. Znakovskaya, M. F. Kling, and R. de Vivie-Riedle, *Chem. Phys.* **366,** 139 (2009).
[78] I. Znakovskaya, P. von den Hoff, S. Zherebtsov, A. Wirth, O. Herrwerth, M. J. J. Vrakking, R. de Vivie-Riedle, and M. F. Kling, *Phys. Rev. Lett.* **103,** 103002 (2009).
[79] B. Fischer, M. Kremer, T. Pfeifer, B. Feuerstein, V. Sharma, U. Thumm, C. D. Schr¥oter, R. Moshammer, and J. Ullrich, *Phys. Rev. Lett.* **105,** 223001 (2010).
[80] Y. Liu, X. Liu, Y. Deng, C. Wu, H. Jiang, and Q. Gong, *Phys. Rev. Lett.* **106,** 073004 (2011).
[81] X. Xie, K. Doblhoff-Dier, S. Roither, M. S. Schöffler, D. Kartashov, H. Xu, T. Rathje, G. G. Paulus, A. Baltuška, S. Gräfe, and M. Kitzler, *Phys. Rev. Lett.* **109,** 243001 (2012).
[82] T. Rathje, A. M. Sayler, S. Zeng, P. Wustelt, H. Figger, B. D. Esry, and G. G. Paulus, *Phys. Rev. Lett.* **111,** 093002 (2013).
[83] A. S. Alnaser, M. Kübel, R. Siemering, B. Bergues, N. G. Kling, K. J. Betsch, Y. Deng, J. Schmidt, Z. A. Alahmed, A. M. Azzeer, J. Ullrich, I. Ben-Itzhak, R. Moshammer, U. Kleineberg, F. Krausz, R. de Vivie-Riedle, and M. F. Kling, *Nat. Commun.* **5,** 3800 (2014).
[84] S. Miura, T. Ando, K. Ootaka, A. Iwasaki, H. Xu, T. Okino, K. Yamanouchi, D. Hoff, T. Rathje, G. G. Paulus, M. Kitzler, A. Baltuška, G. Sansone, and M. Nisoli, *Chem. Phys. Lett.* **595–596,** 61 (2014).
[85] M. Kübel, R. Siemering, C. Burger, N. G. Kling, H. Li, A. S. Alnaser, B. Bergues, S. Zherebtsov, A. M. Azzeer, I. Ben-Itzhak, R. Moshammer, R. de Vivie-Riedle, and M. F. Kling, *Phys. Rev. Lett.* **116,** 193001 (2016).
[86] D. J. Jones, S. A. Diddams, J. K. Ranka, A. Stentz, R. S. Windeler, J. L. Hall, and S. T. Cundiff, *Science* **288,** 635 (2000).
[87] M. Kakehata, H. Takada, Y. Kobayashi, K. Torizuka, Y. Fujihira, T. Homma, and H. Takahashi, *Opt. Lett.* **26,** 1436 (2001).
[88] T. Wittmann, B. Horvath, W. Helml, M. G. Schätzel, X. Gu, A. L. Cavalieri, G. G. Paulus, and R. Kienberger, *Nat. Phys.* **5,** 357 (2009).
[89] S. P. Goreslavski, G. G. Paulus, S. V. Popruzhenko, and N. I. Shvetsov-Shilovski, *Phys. Rev. Lett.* **93,** 233002 (2004).
[90] C. I. Blaga, F. Catoire, P. Colosimo, G. G. Paulus, H. G. Muller, P. Agostini, and L. F. DiMauro, *Nat. Phys.* **5,** 335 (2009).
[91] W. Quan, Z. Lin, M. Wu, H. Kang, H. Liu, X. Liu, J. Chen, J. Liu, X. T. He, S. G. Chen, H. Xiong, L. Guo, H. Xu, Y. Fu, Y. Cheng, and Z. Z. Xu, *Phys. Rev. Lett.* **103,** 093001 (2009).
[92] C. Lemell, K. I. Dimitriou, X. M. Tong, S. Nagele, D. V. Kartashov, J. Burgdörfer, and S. Gräfe, *Phys. Rev. A* **85,** 011403R (2012).
[93] K. Zhang, Y. H. Lai, E. Diesen, B. E. Schmidt, C. I. Blaga, J. Xu, T. T. Gorman, F. Légaré, U. Saalmann, J. Xu, J. M. Rost, and L. F. DiMauro, *Phys. Rev. A* **93,** 021403 (2016).
[94] E. Shigemasa, J. Adachi, M. Oura, and A. Yagishita, *Phys. Rev. Lett.* **74,** 359 (1995).
[95] P. Simon, V. Yulian Vanne, S. Alejandro, C. Alberto, and D. Piero, *Phys. Rev. Lett.* **104,** 223001 (2010).
[96] H. Hasegawa, Y. Ikeda, K. Sonoda, T. Sato, A. Iwasaki, and K. Yamanouchi, *Chem. Phys. Lett.* **662,** 235 (2016).

[97] A. Staudte, S. Patchkovskii, D. Pavicic, H. Akagi, O. Smirnova, D. Zeidler, M. Meckel, D. Villeneuve, R. Dörner, M. Y. Ivanov, and P. B. Corkum, *Phys. Rev. Lett.* **102,** (2009).
[98] H. Akagi, T. Otobe, A. Staudte, A. Shiner, F. Turner, R. Dörner, D. M. Villeneuve, and P. B. Corkum, *Science* **325,** 1364 (2009).
[99] J. Wu, L. P. H. Schmidt, M. Kunitski, M. Meckel, S. Voss, H. Sann, H. Kim, T. Jahnke, A. Czasch, and R. Dörner, *Phys. Rev. Lett.* **108,** 183001 (2012).
[100] A. Hishikawa, E. Takahashi, and A. Matsuda, *Phys. Rev. Lett.* **97,** 243002 (2006).
[101] J. Itatani, J. Levesque, D. Zeidler, H. Niikura, H. Pépin, J. C. Kieffer, P. B. Corkum, and D. M. Villeneuve, *Nature* **432,** 867 (2004).
[102] S. Haessler, J. Caillat, W. Boutu, C. Giovanetti-Teixeira, T. Ruchon, T. Auguste, Z. Diveki, P. Breger, A. Maquet, B. Carré, R. Taïeb, and P. Salières, *Nat. Phys.* **6,** 200 (2010).
[103] S. Haessler, J. Caillat, and P. Salières, *J. Phys. B:At. Mol. Opt. Phys.* **44,** 203001 (2011).
[104] C. Vozzi, M. Negro, F. Calegari, G. Sansone, M. Nisoli, S. De Silvestri, and S. Stagira, *Nat. Phys.* **7,** 822 (2011).
[105] P. Salieres, A. Maquet, S. Haessler, J. Caillat, and R. Taieb, *Rep. Prog. Phys.* **75,** 062401 (2012).
[106] O. Smirnova, Y. Mairesse, S. Patchkovskii, N. Dudovich, D. Villeneuve, P. B. Corkum, and M. Y. Ivanov, *Nature* **460,** 972 (2009).
[107] B. K. McFarland, J. P. Farrell, P. H. Bucksbaum, and M. Guhr, *Science* **322,** 1232 (2008).
[108] W. Li, X. Zhou, R. Lock, S. Patchkovskii, A. Stolow, H. C. Kapteyn, and M. M. Murnane, *Science* **322,** 1207 (2008).
[109] D. Geißler, T. Rozgonyi, J. Gonzàlez-Vàzquez, L. Gonzàlez, S. Nichols, and T. Weinacht, *Phys. Rev. A* **82,** 011402(R) (2010).
[110] L. Fang and G. N. Gibson, *Phys. Rev. A* **75,** 063410 (2007).
[111] C. Wu, H. Zhang, H. Yang, Q. Gong, D. Song, and H. Su, *Phys. Rev. A* **83,** 033410 (2011).
[112] J. Yao, G. Li, X. Jia, X. Hao, B. Zeng, C. Jing, W. Chu, J. Ni, H. Zhang, H. Xie, C. Zhang, Z. Zhao, J. Chen, X. Liu, Y. Cheng, and Z. Xu, *Phys. Rev. Lett.* **111,** 133001 (2013).
[113] P. Wang, S. Xu, D. Li, H. Yang, H. Jiang, Q. Gong, and C. Wu, *Phys. Rev. A* **90,** 033407 (2014).
[114] K. Hosaka, R. Itakura, K. Yokoyama, K. Yamanouchi, and A. Yokoyama, *Chem. Phys. Lett.* **475,** 19 (2009).
[115] T. Ikuta, K. Hosaka, H. Akagi, A. Yokoyama, K. Yamanouchi, F. Kannari, and R. Itakura, *J. Phys. B:At. Mol. Opt. Phys.* **44,** 191002 (2011).
[116] A. E. Boguslavskiy, J. Mikosch, A. Gijsbertsen, M. Spanner, S. Patchkovskii, N. Gador, M. J. J. Vrakking, and A. Stolow, *Science* **335,** 1336 (2012).
[117] J. Mikosch, A. E. Boguslavskiy, I. Wilkinson, M. Spanner, S. Patchkovskii, and A. Stolow, *Phys. Rev. Lett.* **110,** 023004 (2013).
[118] K. Hosaka, A. Yokoyama, K. Yamanouchi, and R. Itakura, *J. Chem. Phys.* **138,** 204301 (2013).
[119] H. Xu, E. Lotstedt, A. Iwasaki, and K. Yamanouchi, *Nat. Commun.* **6,** 8347 (2015).
[120] B. M. Smirnov and M. I. Chibisov, *Sov. Phys. JETP* **22,** 585 (1966).
[121] N. B. Delone and V. P. Krainov, *J. Opt. Soc. Am. B.* **8,** 1207 (1991).
[122] N. B. Delone and V. P. Krainov, *Atoms in Strong Light Fields* (Springer-Verlag, 1985).
[123] A. N. Pfeiffer, C. Cirelli, M. Smolarski, D. Dimitrovski, M. Abu-samha, L. B. Madsen, and U. Keller, *Nat. Phys.* **8,** 76 (2011).
[124] N. I. Shvetsov-Shilovski, D. Dimitrovski, and L. B. Madsen, *Phys. Rev. A* **85,** 023428 (2012).
[125] S. Backus, C. G. Durfee, M. M. Murnane, and H. C. Kapteyn, *Rev. Sci. Instrum.* **69,** 1207 (1998).
[126] D. Strickland and G. Mourou, *Opt. Commun.* **56,** 219 (1985).
[127] D. E. Spence, P. N. Kean, and W. Sibbett, *Opt. Lett.* **16,** 42 (1991).
[128] S. De, M. Magrakvelidze, I. A. Bocharova, D. Ray, W. Cao, I. Znakovskaya, H. Li, Z. Wang, G. Laurent, U. Thumm, M. F. Kling, I. V. Litvinyuk, I. Ben-Itzhak, and C. L. Cocke, *Phys. Rev. A* **84,** 43410 (2011).
[129] T. Ando, A. Shimamoto, S. Miura, K. Nakai, H. Xu, A. Iwasaki, and K. Yamanouchi, *Chem.*

Phys. Lett. **624,** 78 (2015).
[130] E. R. Peck and K. Reeder, *J. Opt. Soc. Am.* **62,** 958 (1972).
[131] G. P. Agrawal, *Nonlinear Fiber Optics 4th edition* (Academic press, 2004).
[132] C. Rullière, *Femtosecond laser pulses : principles and experiments* (Springer, New York, 1998).
[133] M. Nisoli, S. D. Silvestri, O. Svelto, R. Szipöcs, K. Ferencz, C. Spielmann, S. Sartania, and F. Krausz, *Opt. Lett.* **22,** 522 (1997).
[134] V. Pervak, I. Ahmad, M. K. Trubetskov, A. V. Tikhonravov, and F. Krausz, *Opt. Exp.* **17,** 7943 (2009).
[135] N. A. Papadogiannis, B. Witzel, C. Kalpouzos, and D. Charalambidis, *Phys. Rev. Lett.* **83,** 4289 (1999).
[136] P. B. Corkum and F. Krausz, *Nat. Phys.* **3,** 381 (2007).
[137] C. A. Haworth, L. E. Chipperfield, J. S. Robinson, P. L. Knight, J. P. Marangos, and J. W. G. Tisch, *Nat. Phys.* **3,** 52 (2007).
[138] R. Kienberger, E. Goulielmakis, M. Uiberacker, A. Baltuška, V. Yakovlev, F. Bammer, A. Scrinzi, T. Westerwalbesloh, U. Kleineberg, U. Heinzmann, M. Drescher, and F. Krausz, *Nature* **427,** 817 (2004).
[139] X. Liu, H. Rottke, E. Eremina, W. Sandner, E. Goulielmakis, K. O. Keeffe, M. Lezius, F. Krausz, F. Lindner, M. G. Schätzel, G. G. Paulus, and H. Walther, *Phys. Rev. Lett.* **93,** 263001 (2004).
[140] N. G. Johnson, O. Herrwerth, A. Wirth, S. De, I. Ben-Itzhak, M. Lezius, B. Bergues, M. F. Kling, A. Senftleben, C. D. Schröter, R. Moshammer, J. Ullrich, K. J. Betsch, R. R. Jones, A. M. Sayler, T. Rathje, K. Rühle, W. Müller, and G. G. Paulus, *Phys. Rev. A* **83,** 013412 (2011).
[141] A. M. Sayler, M. Arbeiter, S. Fasold, D. Adolph, M. Möller, D. Hoff, T. Rathje, B. Fetić, D. B. Milošević, T. Fennel, and G. G. Paulus, *Opt. Lett.* **40,** 3137 (2015).
[142] B. Bergues, *Opt. Exp.* **20,** 25317 (2012).
[143] A. I. Titov, B. Kämpfer, A. Hosaka, T. Nousch, and D. Seipt, *Phys. Rev. D* **93,** 045010 (2016).
[144] P. L. He, C. Ruiz, and F. He, *Phys. Rev. Lett.* **116,** 203601 (2016).
[145] C. P. J. Martiny and L. B. Madsen, *Phys. Rev. Lett.* **97,** 093001 (2006).
[146] C. P. J. Martiny and L. B. Madsen, *Phys. Rev. A* **76,** 043416 (2007).
[147] K. J. Yuan, S. Chelkowski, and A. D. Bandrauk, *Phys. Rev. A* **93,** 053425 (2016).
[148] M. Bashkansky, P. H. Bucksbaum, and D. W. Schumacher, *Phys. Rev. Lett.* **60,** 2458 (1988).
[149] S. Basile, F. Trombetta, and G. Ferrante, *Phys. Rev. Lett.* **61,** 2435 (1988).
[150] A. Jaroń, J. Z. Kamiński, and F. Ehlotzky, *Opt. Commun.* **163,** 115 (1999).
[151] C. P. J. Martiny, M. Abu-Samha, and L. B. Madsen, *J. Phys. B:At. Mol. Opt. Phys.* **42,** 161001 (2009).
[152] F. Silva, M. Miranda, B. Alonso, J. Rauschenberger, V. Pervak, and H. Crespo, *Opt. Exp.* **22,** 10181 (2014).
[153] J. R. Birge, R. Ell, and F. X. Kartner, *Opt. Lett.* **31,** 2063 (2006).
[154] J. R. Birge, H. M. Crespo, and F. X. Kaertner, *J. Opt. Soc. Am. B.* **27,** 1165 (2010).
[155] A. M. Perelomov and V. S. Popov, *Sov. Phys. JETP* **25,** 336 (1967).
[156] P. Eckle, M. Smolarski, P. Schlup, J. Biegert, A. Staudte, M. Schöffler, H. G. Muller, R. Dörner, and U. Keller, *Nat. Phys.* **4,** 565 (2008).
[157] R. W. Boyd, *J. Opt. Soc. Am.* **70,** 877 (1980).
[158] T. Otobe and K. Yabana, *Phys. Rev. A* **75,** 062507 (2007).
[159] P. Eckle, A. N. Pfeiffer, C. Cirelli, A. Staudte, R. Dörner, H. G. Muller, M. Büttiker, and U. Keller, *Science* **322,** 1525 (2008).
[160] A. S. Landsman, M. Weger, J. Maurer, R. Boge, A. Ludwig, S. Heuser, C. Cirelli, L. Gallmann, and U. Keller, *Optica* **1,** 343 (2014).
[161] L. Torlina, F. Morales, J. Kaushal, I. Ivanov, A. Kheifets, A. Zielinski, A. Scrinzi, H. G. Muller, S. Sukiasyan, M. Ivanov, and O. Smirnova, *Nat. Phys.* **11,** 503 (2015).
[162] N. Teeny, E. Yakaboylu, H. Bauke, and C. H. Keitel, *Phys. Rev. Lett.* **116,** 063003 (2016).
[163] M. Lebech, J. C. Houver, and D. Dowek, *Rev. Sci. Instrum.* **73,** 1866 (2002).
[164] J. Ullrich, R. Moshammer, A. Dorn, R. Dörner, L. P. H. Schmidt, and H. Schmidt, *Rep. Prog.*

Phys. **66,** 1463 (2003).
[165] K. Hosaka, J. Adachi, A. V. Golovin, M. Takahashi, N. Watanabe, and A. Yagishita, *Jpn. J. Appl. Phys.* **45,** 1841 (2006).
[166] A. Matsuda, M. Fushitani, and A. Hishikawa, *J. Elec. Spec. Rel. Phenom.* **169,** 97 (2009).
[167] C. S. Lehmann, N. B. Ram, and M. H. Janssen, *Rev. Sci. Instrum.* **83,** 093103 (2012).
[168] W. C. Wiley and I. H. McLaren, *Rev. Sci. Instrum.* **26,** 1150 (1955).
[169] A. T. J. B. Eppink and D. H. Parker, *Rev. Sci. Instrum.* **68,** 3477 (1997).
[170] C. J. Dasch, *Appl. Opt.* **31,** 1146 (1992).
[171] D. J. Kane and R. Trebino, *IEEE J. Quantum Electron.* **29,** 571 (1993).
[172] R. Trebino, K. W. DeLong, D. N. Fittinghoff, J. N. Sweetser, M. A. Krumbugel, B. A. Richman, and D. J. Kane, *Rev. Sci. Instrum.* **68,** 3277 (1997).
[173] O. Jagutzki, A. Cerezo, A. Czasch, R. Dorner, M. Hattas, Min Huang, V. Mergel, U. Spillmann, K. Ullmann-Pfleger, T. Weber, H. Schmidt-Böcking, and G. D. W. Smith, *IEEE Trans. Nucl. Sci.* **49,** 2477 (2002).
[174] S. E. Sobottka and M. B. Williams, *IEEE Trans. Nucl. Sci.* **35,** 348 (1988).
[175] RoentDek Handels GmbH, *The RoentDek Constant Fraction Discriminators CFD8b, CFD4b and CFD1b (9.1.904.1)* (RoentDek Handels GmbH, Kelkheim, 2009).
[176] RoentDek Handels GmbH, *MCP Delay Line Manual (Version 9.22.1003.1)* (RoentDek Handels GmbH, Kelkheim, 2010).
[177] RoentDek Handels GmbH, *MCP Delay Line Manual (Version 11.0.1304.1)* (RoentDek Handels GmbH, Kelkheim, 2013).
[178] S. L. Chin, *Phys. Rev. A* **4,** 992 (1971).
[179] A. Talebpour, A. D. Bandrauk, J. Yang, and S. L. Chin, *Chem. Phys. Lett.* **313,** 789 (1999).
[180] Q. Song, Z. Li, S. Cui, P. Lu, X. Gong, Q. Ji, K. Lin, W. Zhang, J. Ma, H. Pan, J. Ding, M. F. Kling, H. Zeng, F. He, and J. Wu, *Phys. Rev. A* **94,** 053419 (2016).
[181] T. Suzuki, *Annu. Rev. Phys. Chem.* **57,** 555 (2006).
[182] K. L. Reid, *Mol. Phys.* **110,** 131 (2012).
[183] K. Kimura, S. Katsumata, Y. Achiba, T. Yamazaki, and S. Iwata, *Handbook of HeI photoelectron spectra of fundamental organic molecules* (Japan Scientific Societies Press, Tokyo, 1981).
[184] J. Berkowitz, *J. Chem. Phys.* **69,** 3044 (1978).
[185] L. Holmegaard, J. L. Hansen, L. Kalhøj, S. L. Kragh, H. Stapelfeldt, F. Filsinger, J. Küpper, G. Meijer, D. Dimitrovski, M. Abu-samha, C. P. J. Martiny, and L. B. Madsen, *Nat. Phys.* **6,** 428 (2010).
[186] J. L. Hansen, H. Stapelfeldt, D. Dimitrovski, M. Abu-samha, C. P. J. Martiny, and L. B. Madsen, *Phys. Rev. Lett.* **106,** 073001 (2011).
[187] E. Shigemasa, J. Adachi, K. Soejima, N. Watanabe, A. Yagishita, and N. A. Cherepkov, *Phys. Rev. Lett.* **80,** 1622 (1998).
[188] S. Motoki, J. Adachi, Y. Hikosaka, K. Ito, M. Sano, K. Soejima, A. Yagishita, G. Raseev, and N. A. Cherepkov, *J. Phys. B:At. Mol. Opt. Phys.* **33,** 4193 (2000).
[189] N. A. Cherepkov, G. Raseev, J. Adachi, Y. Hikosaka, K. Ito, S. Motoki, M. Sano, K. Soejima, and A. Yagishita, *J. Phys. B:At. Mol. Opt. Phys.* **33,** 4213 (2000).
[190] V. Kumarappan, L. Holmegaard, C. P. J. Martiny, C. B. Madsen, T. K. Kjeldsen, S. S. Viftrup, L. B. Madsen, and H. Stapelfeldt, *Phys. Rev. Lett.* **100,** 093006 (2008).
[191] G. F. Gribakin and M. Y. Kuchiev, *Phys. Rev. A* **55,** 3760 (1997).
[192] T. K. Kjeldsen and L. B. Madsen, *J. Phys. B:At. Mol. Opt. Phys.* **37,** 2033 (2004).
[193] M. J. Frisch, G. W. Trucks, H. B. Schlegel*, et al*, Gaussian~09 Revision A.02, Gaussian Inc., Wallingford CT, 2009.
[194] D. Dimitrovski, C. P. J. Martiny, and L. B. Madsen, *Phys. Rev. A* **82,** 053404 (2010).
[195] B. Cheng, M. Bahou, W. Chen, C. Yui, Y. Lee, and L. C. Lee, *J. Chem. Phys.* **117,** 1633 (2002).
[196] E. Runge and E. K. U. Gross, *Phys. Rev. Lett.* **52,** 997 (1984).
[197] G. Öhrwall, P. Karlsson, M. Wirde, M. Lundqvist, P. Andersson, D. Ceolin, B. Wannberg, T. Kachel, H. Dürr, W. Eberhardt, and S. Svensson, *J. Elec. Spec. Rel. Phenom.* **183,** 125 (2011).

[198] FEMTOLASERS Produktions GmbH, *FEMTOOPTICS™ 2013 | 2014* (FEMTOLASERS Produktions GmbH, Vienna, 2013).
[199] G. Ghosh, *Opt. Commun.* **163,** 95 (1999).
[200] M. J. Dodge, *Appl. Opt.* **23,** 1980 (1984).
[201] M. B. Robin and N. A. Kuebler, *J. Elec. Spec. Rel. Phenom.* **1,** 13 (1972).
[202] H. Ogata, H. Onizuka, Y. Nihei, and H. Kamada, *Bull. Chem. Soc. Jpn.* **46,** 3036 (1973).
[203] S. Katsumata, T. Iwai, and K. Kimura, *Bull. Chem. Soc. Jpn.* **46,** 3391 (1973).
[204] L. Karlsson, R. Jadrny, L. Mattsson, F. T. Chau, and K. Siegbahn, *Phys. Scr.* **16,** 225 (1977).
[205] K. M. A. Refaey and W. A. Chupka, *J. Chem. Phys.* **48,** 5205 (1968).
[206] P. Warneck, *Z. Naturforsch. A* **26,** 2047 (1971).
[207] T. Nishimura, Y. Niwa, T. Tsuchiya, and H. Nozoye, *J. Chem. Phys.* **72,** 2222 (1980).
[208] S. Nakamura, K. Midorikawa, M. Obara, and K. Toyoda, *Jpn. J. Appl. Phys.* **32,** 3833 (1993).
[209] Wolfram Research Inc., Mathematica Version 10.4, Wolfram Research, Inc., Champaign, Illinois, 2016.

Acknowledgements

First of all, I would like to thank my supervisor, Prof. Kaoru Yamanouchi. He gave me a lot of invaluable advice, and I learned a lot from his attitude to research. He also gave me a chance to study under Dr. Ryuji Itakura in Kansai Photon Science Institute, National Institutes for Quantum and Radiological Science and Technology.

I am deeply indebted Dr. Ryuji Itakura for his valuable guidance, his kind support during my stay, and fruitful discussion with him. I learned a lot not only skills but also attitude to research. I would also like to thank Dr. Hiroshi Akagi and Dr. Tomohito otobe in Kansai Photon Science Institute, and Dr Motoyoshi Nakano now in Tohoku University for their support and fruitful discussion with them.

I am deeply grateful to Prof. Atsushi Iwasaki and Prof. Reika Kanya in Prof. Yamanouchi's group for their valuable guidance and kind help to perform experiments. My gratitude also goes out to Dr. Toshiaki Ando for his valuable advice and fruitful discussion with him. Besides, I would like to thank Dr. Shun Miura for his kind help during my master course study. I am also grateful to the all the other members in Prof. Yamanouchi's group, including previous members while I was a undergraduate student and a master course student, especially, Prof. Tsuyoshi Kato, Dr. Katsunori Nakai, Dr. Erik Lötstedt, Dr. Tamas Szidarovszky, Dr. Takahiro Teramoto, Dr. Tomoya Okino, Mr. Takashi Hiroi, Ms. Mihoshi Abe, Dr. Yoshihiro Ide, Mr. Seiji Ogami, Mr. Yuki Ikeda, Mr. Kakuta Ishida, Ms. Kana Yamada, Ms. Qiqi Zhang and Mr. Makoto Mizui.

I would like to thank Prof. Gerhard G. Paulus and Dr. Tim Rathje in Friedrich-Sciller-Universitat Jena for their kind cooperation in the CEP-tagging experiments.

Last but most importantly, I am grateful to my parents for their warm support over the course of my Ph.D studies.